A Mathematical Model for the Long-Term Dynamics of Tethered Spacecraft

by

Eric LM Lanoix

Department of Mechanical Engineering

McGill University, Montreal

June 1999

This thesis was submitted to the Faculty of Graduate Studies and Research in partial fulfilment of the requirements for the Master of Engineering degree

0-612-55023-0

I ACKNOWLEDGEMENTS

First of all, the author wishes to thank Dr. Arun K. Misra of McGill University for his precious advice and for his scientific rigour in the review of the author's work. The author feels privileged to have had the opportunity to collaborate with Dr. Misra over the last four years.

The author would also like to express his gratitude toward the following people: Dr. Vinod J. Modi (UBC) who cordially welcomed the author to Vancouver over the Summer of 1998 for his experiments on the physical properties of space tethers; Mr. James Barnds (Naval Research Laboratory) for providing information on the TiPS mission; Mr. Joe Carroll (Tether Applications) for graciously providing a space tether sample and for his advice on the heat transfer and librational decay of space tethered systems; Dr. Alex Jablonski (CSA) for providing precious first-hand information on the BOLAS proposal, Barbara G. Wood for her editorial suggestions, and to all the others I forget....

The author's work on tethered spacecraft over the last two years was supported by the Natural Sciences and Engineering Council of Canada (NSERC), by the Canadian Space Agency through an NSERC supplement, and by the Fonds pour la formation de chercheurs et l'aide à la recherche (FCAR).

Finally, the author would like to express my gratitude towards his parents, Julien and Germaine, and to God who gave him the opportunity to live at a time and place when humankind is no longer confined to survival, but can truly wonder about its origins, its place and its destiny among the stars...

ABSTRACT

A tethered satellite system consists of two or more orbiting satellites linked together by a tether (or cable). Although much theoretical and experimental work has contributed to a good understanding of the short-term dynamics of tethered systems, their long-term behaviour remains unexplored. Hence, a detailed mathematical model and a software have been developed to analyse the long-term effect of the low Earth orbit environment on tethered systems. The software predicts the trajectory and the attitude of the system, as well as the temperature and the longitudinal vibrations of the tether. The program accounts for the effects of atmospheric lift and drag, asphericity of the Earth (zonal and sectorial harmonics), solar and Earth radiation, electromagnetic forces, lunisolar attraction, and material damping.

The thesis reviews previous research work in the field and extends it using more detailed models of external perturbations. Particular attention is given to the three major external forces influencing the dynamics of tethered systems: atmospheric forces, Earth oblateness effects, and electromagnetic forces. Furthermore, analytical solutions are provided for the problem of atmospheric drag induced shift of the equilibrium angle.

It was noted that the present formulation can predict the long-term motion of non-conductive librating tethered systems (such as TiPS) with greater accuracy than previous models. The simulation software is also used to study the behaviour of spinning and conductive systems. The results show that bare conductive tethers can decay the orbit of spent rocket stages or dysfunctional satellites over 100 kg at a lower "weight cost" than traditional rocket systems and much faster than atmospheric drag.

RESUME

Un satellite cablé est composé de deux satellites ou plus liés entre eux par un cable. Malgré le fait que la dynamique à court terme des satellites cablés soit maintenant bien connue, il demeure que le comportement à long terme de ce type de système reste mal compris. Donc un modèle très détaillé fut développé afin de mieux cerner le comportement des satellites cablés à long terme. Le modèle et le programme qui s'y rattache prédisent la trajectoire orbitale, les mouvements de lacet et de tangage, ainsi que la température et l'élongation du cable. Le modèle prend les facteurs suivants en ligne de compte: la portance et le freinage aérodynamique, la non-sphéricité et la non-homogénéité de la Terre, la pression de radiation solaire et terrienne, les forces électromagnétiques, l'attraction luni-solaire, et finalement les pertes visco-élastiques du cable.

Ce mémoire passe en revue les divers travaux de recherche qui furent publiés à ce sujet et cherche à obtenir des résultats plus précis en utilisant des modèles de forces perturbatrices plus précis que par le passé. Une attention particulière est portée aux trois forces perturbatrices influençant le plus la dynamique des satellites cablés: la portance et le freinage aérodynamique, la non-sphéricité et la non-homogénéité de la Terre, et les forces électromagnétiques. De plus, le problème du changement de l'angle d'équilibre dû au freinage aérodynamique est résolu analytiquement.

Les résultats obtenus démontrent que le modèle arrive à prédire la dynamique à long terme des satellites cablés non-conducteurs (tels que TiPS) avec plus de précision que les modèles utilisés précédemment. Le programme de simulation est également mis à contribution afin d'étudier le comportement des satellites cablés en rotation continue et celui des satellites cablés dotés d'un cable conducteur. Les résultats démontrent qu'un cable conducteur "nu" arrive à faire réentrer les satellites de plus de 100 kg dans l'atmosphère plus rapidement que la propulsion chimique et beaucoup plus rapidement que le freinage aérodynamique.

IV NOMENCLATURE

Variables:

A	tether cross-sectional area
$A_p, \mathbf{A}_p, \mathbf{A}_{pp}$	spacecraft area shape factors
$\mathbf{B}$	magnetic field
C	Earth asphericity coefficient
D	torsional damping coefficient
E	Young's modulus
$\mathbf{F}$	perturbative force
F^{o}	shape factor for radiative heat transfer
F^{*}	Earth rotation factor
G	tether shear modulus of elasticity
H	atmospheric scale height
I	tether current; polar moment of inertia of the tether
J	Earth asphericity coefficient; load moment of inertia
L	mean longitude at epoch
L^{*}	true longitude at epoch
P_1, P_2, Q_1, Q_2	equinoctial elements
Q	generalized force
$\mathbf{R}$	position vector
R	geocentric altitude; resistance
R'	geodetic altitude
S	solar radiation pressure; Earth asphericity coefficient
T	temperature; kinetic energy
V	velocity; potential energy
a	semi-major axis
a_1, a_2, c_1, c_2	end mass dimensions
b	Earth polar radius
c	speed of light; damping constant
e	orbital eccentricity
$\mathbf{f}'$	perturbative acceleration in orbital coordinates

g,h	Earth magnetic field coefficients
k	spring constant
i	orbital inclination
l_o	unstressed and thermally disturbed tether length
l	tether length
m	mass
m_e	electron mass; equivalent mass
n	mean motion
n_e	ionospheric electron density
r_t	tether radius
u	argument of latitude
x	distance along the tether
Ω	right ascension of the ascending node
Φ	potential field
ψ	shining factor
Υ	electromotive force
Ξ	total power of the Sun
α	pitch angle
β	tether visco-elastic dissipation coefficient
β^*	ballistic coefficient
ϑ	ratio of the amplitude between two consecutive maxima
γ	roll angle
δ	distance between the spacecraft centre of mass and m_1
δ^*	distance between the spacecraft centre of area and m_1
ϵ	strain; emissivity
ζ	damping ratio
κ	tether heat capacity
λ	eastern longitude from the vernal equinox
λ_g	eastern longitude from Greenwich
ϕ	latitude
ρ	density
θ	true anomaly
σ	accommodation coefficient; solar reflectivity/absorptivity; standard deviation

τ	period
ξ	thermal expansion coefficient
ω	argument of perigee; circular frequency

Constants:

R_u	universal gas constant
μ	gravitational parameter

Subscripts and Superscripts:

D	Drag
ND	non-dimensional
a	absorbed
atm	atmosphere
cyl	cylinder
e	equivalent
load	load
long	longitudinal
max	maximum
n	normal
orb	orbital
rd	diffuse reflectivity
rs	specular reflectivity
s	spacecraft
sph	sphere
t	tether, tangential
tot	total
α	pitch angle
γ	roll angle
ϵ	strain
1,2	First and second end mass
⊕,☼,☾	Earth, Sun, Moon

TABLE OF CONTENTS

CHAPTER 1

INTRODUCTION

1.1 PRELIMINARY REMARKS

A tethered satellite system consists of two or more orbiting satellites linked together by a tether (Fig. 1.1). This concept dates back to the work of Tsiolkovsky [1]. In 1895, he envisioned a gigantic tower stretching from the ground to a geostationary orbit from which satellites could be deployed in orbit. Although highly impractical, this idea inspired other scientists who later suggested using tethers or cables to build large space structures. Among them, Colombo has come to be considered the "father of space tethers" for his major contribution to this new field of study [2].

For practical reasons, space tethered systems are always stowed during launch. The tether deployment begins with the separation of the end-bodies and proceeds until the tether is completely wound out from the reel (Fig. 1.2). The system then enters its station-keeping phase during which it gathers most of the scientific data. For many missions, the tether is expected to remain deployed until the end of the satellite lifetime. Air drag then slowly decays the orbit of the spacecraft until the system disintegrates in the upper atmosphere.

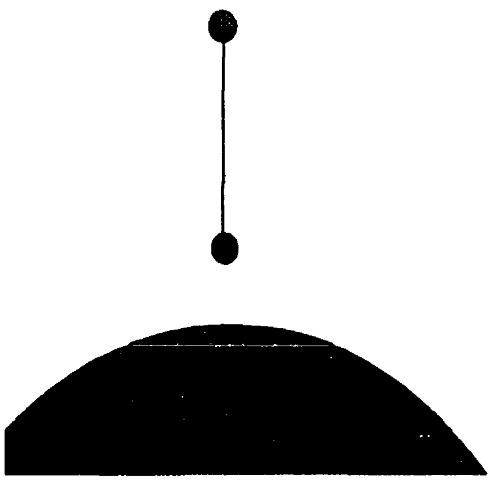

Fig. 1.1: Tethered Satellite Orbiting the Earth

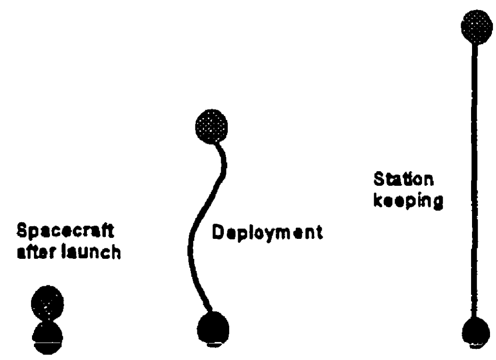

Fig. 1.2: Tethered Satellite Mission History

1.2 PREVIOUS AND CURRENT SPACE TETHERED FLIGHTS

1.2.1 The Gemini Tether Experiments

The first demonstration of space tethered flight took place in September 1966 during the *Gemini* XI mission [3]. After the crew docked their Gemini capsule with an Agena upper stage, astronaut Richard Gordon performed a spacewalk to attach the two spacecraft with a 30 m long tether. Commander Pete Conrad then separated the two spacecraft (Fig. 1.3) and attempted to stabilize the system in the gravity gradient configuration. Unfortunately, the manoeuvre failed. Conrad then spun the system up and tried to stabilize it in the cartwheel configuration, with both spacecraft spinning around the centre of mass of the system. The manoeuvre succeeded: the tether finally became taut. The rotational rate of the Gemini-Agena spacecraft was increased to 55 deg/min: almost one rotation every six minutes. At this point, the astronauts experienced an artificial gravity of 10^{-4} g - enough for one of their cameras to "fall" to the bottom of the capsule.

Two months later, Jim Lovell and Buzz Aldrin attempted a similar experiment on board Gemini XII and achieved stability in the gravity gradient configuration. Despite these successes, the behaviour of tethered systems remained poorly understood.

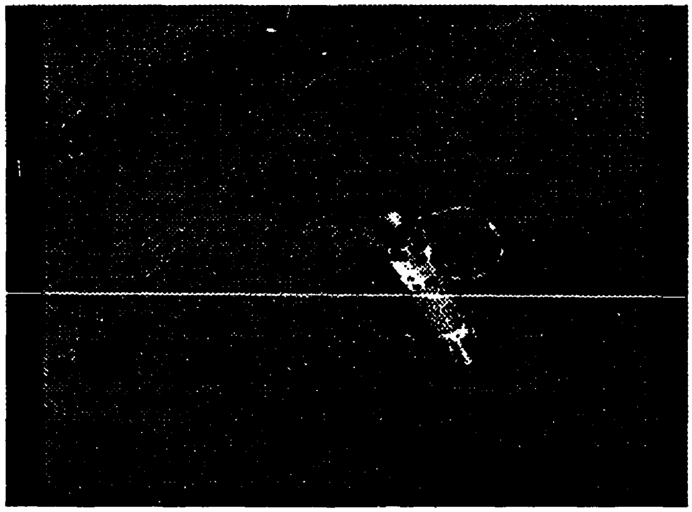

Fig. 1.3: Tether Experiment during the Gemini Program [4]

1.2.2 The OEDIPUS Flights

Over the two decades that followed, an extensive amount of research contributed to a better understanding of tether dynamics. Nevertheless, the US/Japan CHARGE 2A and 2B suborbital flights were the only missions to test these new theories [5].

On January 30, 1989, the *OEDIPUS*-A (Observations of Electric-field Distribution in the Ionospheric Plasma - a Unique Strategy) suborbital mission was launched into a boreal aurora from Andoya in Norway [5,6]. This Canadian-American venture (Fig. 1.4) carried a conductive tether and completed a number of experiments on tether dynamics, on the magnetic field of the Earth, and on ionospheric plasma. The tether consisted of a tin-coated copper wire covered with a white Teflon insulator. It had a diameter of 0.85 mm and measured 958 m. On November 6, 1995, a more advanced probe called OEDIPUS-C flew a similar mission from Fairbanks (Alaska) using a 1174 m tether.

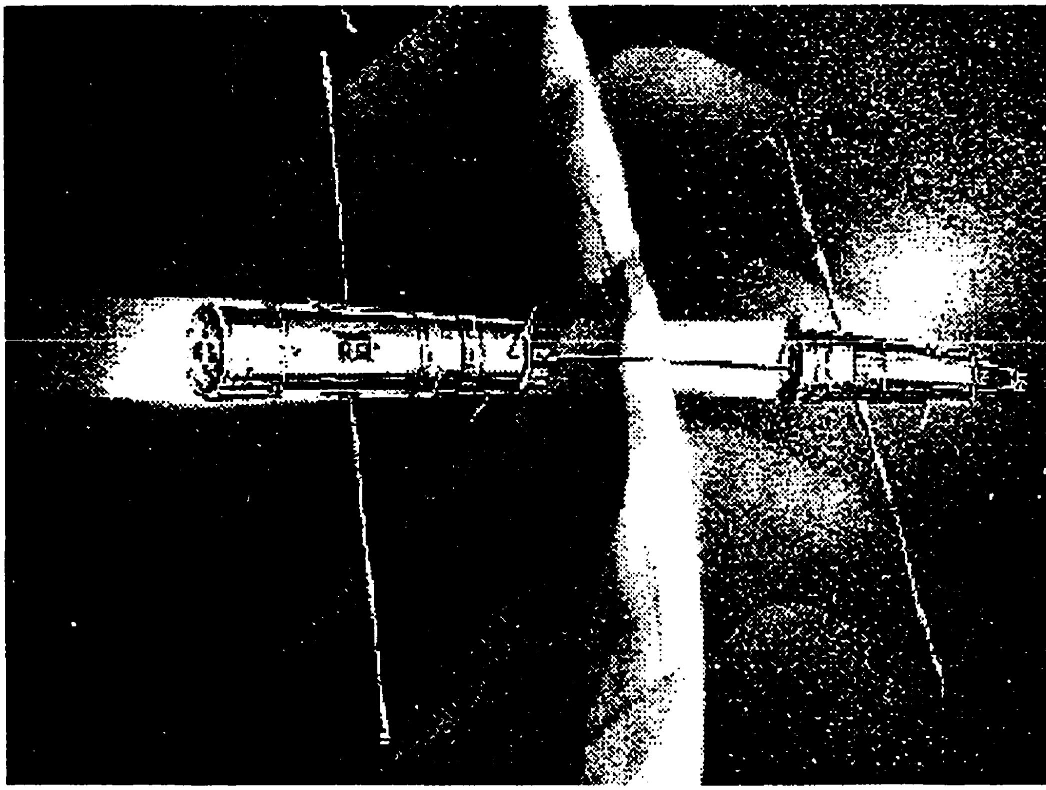

Fig. 1.4: Artist Rendition of the Oedipus-A Separation [7]

1.2.3 The TSS-1 Experiments

Over the 80's and 90's, the U.S. and Italy combined their efforts to better understand tether dynamics, space plasma physics, and electric power generation using the *Faraday effect* [6]. The result of their collaboration took the form of a spherical subsatellite connected to the Orbiter by a 20.7 km long conductive tether.

The *TSS* (Tether Satellite System) flew on the Space Shuttle during missions STS-46 in July-August 1992 and STS-75 in February 1996 (Fig. 1.5). The first mission (TSS-1) failed when the deployment system malfunctioned after deploying only 268 m of tether. During the second mission (TSS-1R), the tether was deployed to 19.7 km, while the TSS system generated an EMF of 3500 Volts [8]. This high electric potential resulted from the motion of the conductive tether through the magnetic field of the Earth. However, a flaw in the tether insulation sparked an electrical arc which eventually ruptured the tether.

Despite these mishaps, the TSS demonstrated the unexpected capability of bare metals to capture ionospheric electrons. Indeed, the power generated during the experiment reached many times the expected value.

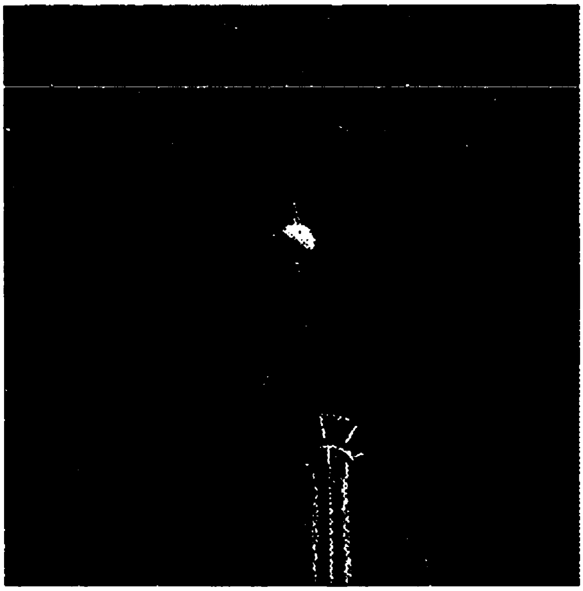

Fig. 1.5: TSS-1R Experiment on the Space Shuttle [9]

1.2.4 The SEDS Flights

Although they did not receive as much publicity as the ill-fated TSS-1 experiments, the *SEDS* (Small Expandable Deployer System) flights successfully demonstrated the feasibility of tether momentum transfer and proved the validity of deployment control laws [6]. Both missions flew as secondary payloads on Delta II launches and involved a 20 km long tether made of SPECTRA-1000.

Launched on March 29, 1993, the SEDS-1 mission demonstrated the deployment of very long tethers (20 km). At the end of the flight, the tether was deliberately severed to experiment tether-based orbital transfer. The manoeuvre successfully raised the orbit of the upper body (Delta II stage) and caused the SEDS-1 payload to deorbit.

SEDS-2 was deployed on March 9, 1994 using a predetermined control scheme. This procedure was designed to reduce tether jerk and libration angles at the end of deployment. The experiment was a complete success with the final deployment rate reaching a mere 2 cm/s (as opposed to 7 m/s for SEDS-1). Furthermore, the final angle of the system with respect to the local vertical was only 4 degrees. The mission lasted about one week until the tether was severed by either a micro-meteorite or a piece of debris.

1.2.5 The PMG Mission

The *PMG* (Plasma Motor Generator) flew on June 26, 1993 as a secondary payload on a Delta II rocket [6]. With the aid of a 500 m conductive tether, the mission demonstrated how the motion of a conductive tether across the magnetic field of the Earth can boost the orbit of a spacecraft (while the system expends electrical energy) or generate electricity (while lowering the spacecraft orbit).

1.2.6 The TiPS Mission

More recently, the flight of *TiPS* (Tether Physics and Survivability) has been paving the way for much longer missions [10]. The spacecraft was sponsored by the *NRO* (Naval Reconnaissance Office) and built by the *NRL* (Naval Research Laboratory) to study the survivability and the long-term dynamics of tethered satellites (Fig. 1.6).

Deployed on June 20, 1996, TiPS has now been operating for three years. TiPS is equipped with a 4 km long tether made of SPECTRA-1000 braided with acrylic. Although much of the data gathered during the flight correlates with current models, no model has yet fully explained the curious fashion in which the librational oscillations of the system have damped. The flight of TiPS is analysed in detail in Chapter 4.

Fig. 1.6: Artist Rendition of the Separation of TiPS [11]

1.2.7 The ATEx Mission

Inspired by the success of TiPS, the NRO and the NRL recently launched the *ATEx* (Advanced Tether Experiment) mission (Fig. 1.7). Equipped with a 6 km long tether, the ATEx system was launched on October 3, 1998 atop the STEx satellite by a Taurus rocket [12]. The mission has three primary objectives. First, the ATEx team intends to conduct experiments on tether libration control using a set of 16 thrusters located on the lower end body (STEx). Second, they plan to demonstrate end body attitude control and determination using *SLR* (Satellite Laser Ranging) techniques [6]. Finally, they plan to show how a multi-lined tether "tape" can drastically increase the survivability of space tethered systems against micro-meteorites and space debris (Fig. 1.8).

Tether deployment took place on January 16, 1999. Unfortunately, the STEx onboard computer ordered the tether to be cut when the libration angle of the system became too large. This occurred after only 22 metres of tether had been deployed. The exact cause of the incident is currently under investigation.

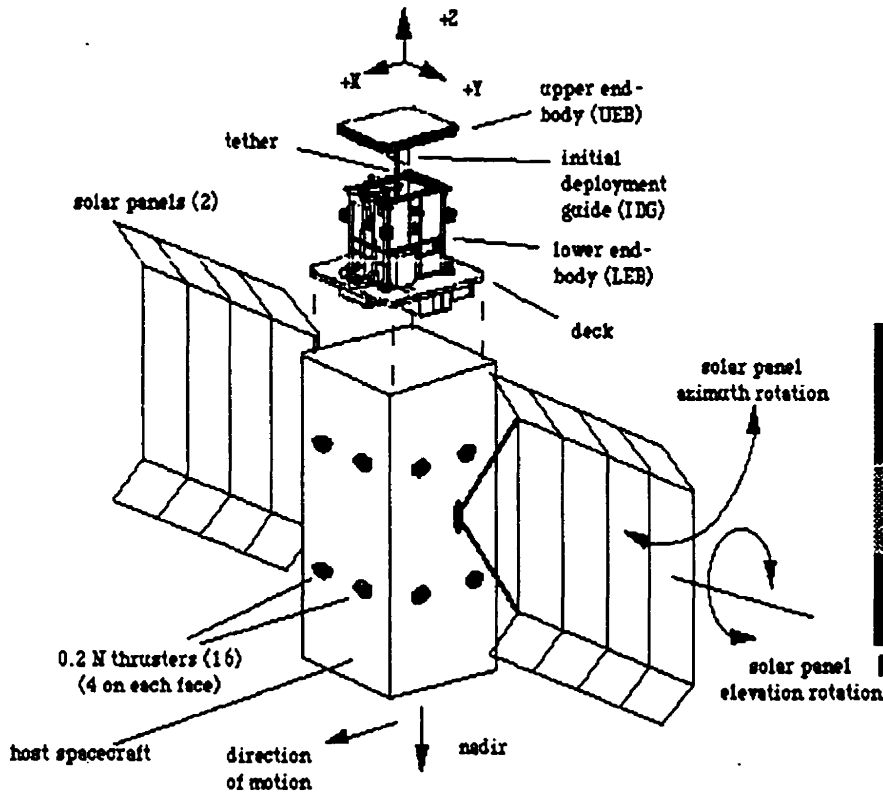

Fig. 1.7: Schematic View of the ATEx/STEx Tethered Spacecraft [13]

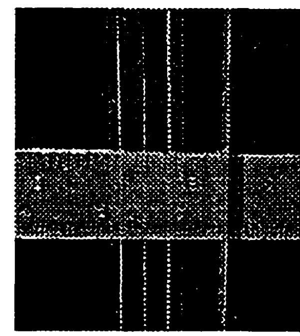

Fig. 1.8: ATEx Three-Lined Tether Tape [14]

1.3 APPROVED TETHERED MISSIONS

1.3.1 The SESDE Mission

The *ESA* (European Space Agency) and Russia plan to fly the first all European tether experiment [15]. The *SESDE* mission (Small Expandable Spool Deployment Experiment) will take place on a *PROGRESS-M* resupply ship.

After the cargo spacecraft has undocked from the MIR space station, the tether deployer will release the ship docking mechanism (50 kg) using a simple spring loaded device. Following this initial release, the gravity gradient force will create enough tension to complete the deployment of the 3 km long tether without further assistance. The main objective of this mission is to demonstrate the safety and reliability of the deployment mechanism. As in the SEDS-1 mission (Section 1.2.4), such a procedure could be used to deorbit re-entry capsules from the *ISS* (International Space Station).

1.3.2 Tethered De-orbit Test Flights

The progressive accumulation of artificial space debris in Earth orbit has become an increasingly alarming issue over the last decade [16]. There is a proposal to run ionospheric electrons down a conductive tether so that the resulting *Lorentz force* would decay the orbit of spent rocket stages and dysfunctional satellites much faster than air drag [8,17]. The initial test flight is expected to take place at the turn of the millennium on board a MOLNIYA or a DNIEPR (SS-18) rocket.

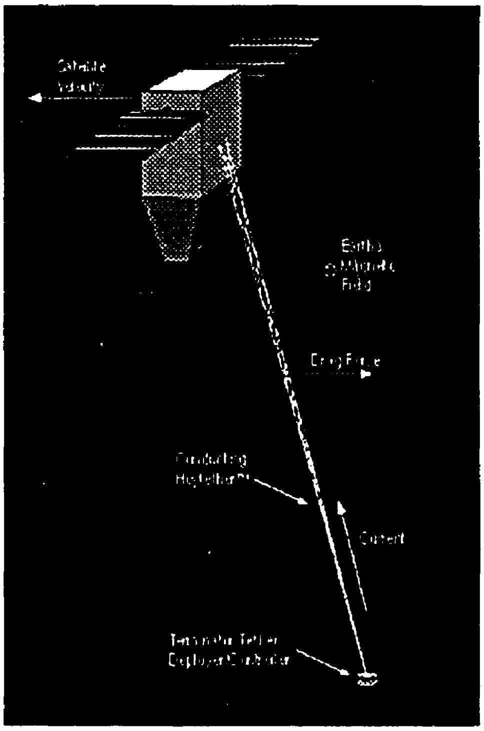

Fig. 1.9: Conceptual View of the Tethered De-orbit Concept [18]

1.4 PROPOSED TETHERED MISSIONS

1.4.1 The AIRSEDS-S Mission

A group of scientists have recently proposed to fly an atmospheric probe on the space shuttle [6,19]. The *AIRSEDS-S* (Atmospheric/Ionospheric Research Small Expandable Deployer Satellite) probe would hover below the Orbiter at the end of a 90 km tether and safely study the upper atmosphere at altitudes down to 140 km (Fig. 1.10). Unlike other spacecraft flying at such altitudes, AIRSEDS-S would not re-enter the atmosphere immediately because the tether tension would provide the necessary upward force.

Moreover, tethered systems can also be used to conduct close range remote sensing studies.

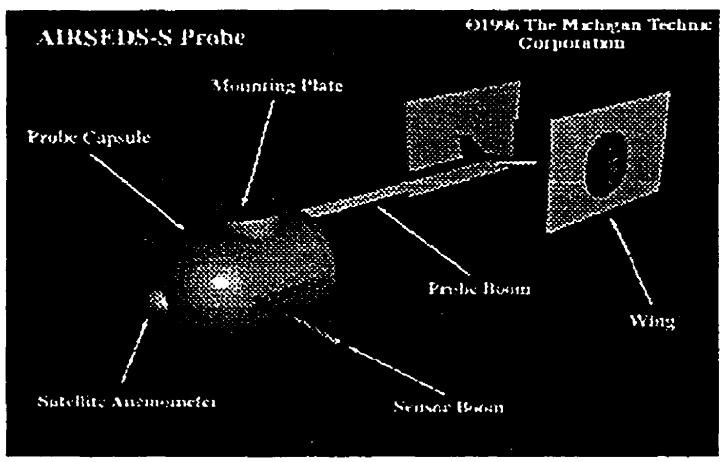

Fig. 1.10: Conceptual Representation of the AIRSEDS-S Probe [20]

1.4.2 The BOLAS Mission

In addition, the *BOLAS* (Bistatic Observations using Low Altitudes Satellites) mission has been proposed to the Canadian Space Agency and *NASA* [21,22]. If approved, this system will consist of two 75 kg microsatellites linked by a 100 m long tether. Depicted in Figure 1.11, this spacecraft will study the ionosphere for six months and will use its own spin for stabilization purposes. The BOLAS proposal is analysed in detail in Chapter 6.

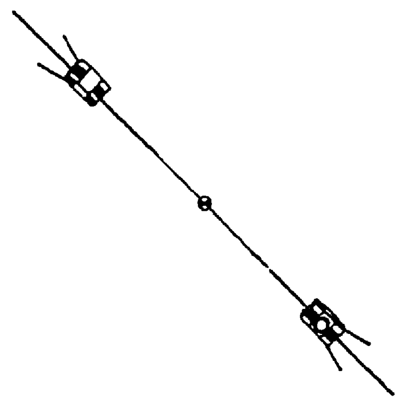

Fig. 1.11: Conceptual Representation of the BOLAS Proposal [23]

1.4.3 Space Station Power Generation and Reboost

Several scientists have recently proposed to fly long semi-insulated wires from the ISS to generate power or to reboost the orbit of the space station [6,24,25,26]. Like the tethered de-orbit proposal (Section 1.3.2), this concept relies on the motion of a conductive material across the magnetic field of the Earth. The effect attained (power generation or reboost) depends on the direction of the tether current. For example, running electrons "down" a 20 km long aluminum wire can provide an average power of 5.3 kW. However, this output comes at the expense of a 1 N electrodynamic drag which slowly decays the station orbit. On the other hand, by running electrons "up" a 7 km long tether using a battery or solar energy, *EP* (Electromagnetic Propulsion) can maintain the orbit of the space station with approximately 7% of the station power (10 kW input). In economic terms, the yearly amount of propellant economized with EP would reach the amount of fuel provided by 4 PROGRESS-M resupply ships. This represents an economy of $US 2 billion over ten years.

But that is not all, EP can potentially be used to control the orbital elements and the librations of tethered systems. This concept is discussed in Chapter 5.

1.5 FUTURE APPLICATIONS OF SPACE TETHERS

1.5.1 Space Station Related Applications

Aside from power generation and electromagnetic propulsion (EP), the ISS represents a unique opportunity to implement several new tether proposals. For example, the *STEPS* (Station Tethered Express Payload System) calls for a novel and yet simple approach to return small payloads from the ISS to the Earth [6]. The payload and the tether (~30 km) are released downward from the ISS. Once properly swung, the tether is severed at the ISS end (Fig. 1.12). Conserving the angular momentum, the orbit of the space station is raised and that of the payload is lowered, causing it to reenter the atmosphere. This innovative approach can be used to release payloads from the space station between shuttle flights, without the need to worry about safety hazards and rocket systems. This procedure can also be used to raise the orbit of the ISS while allowing the Space Shuttle to return to the Earth using less fuel [27].

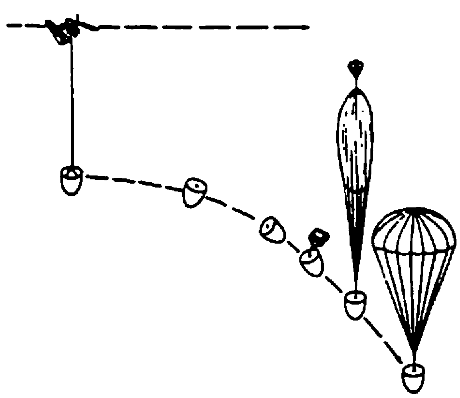

Fig. 1.12: The STEPS Concept [6]

On the other hand, spinning a tethered space station generates artificial gravity [6,28]. This application becomes particularly useful for long term manned flights such as those involved in interplanetary exploration, since the maintenance of artificial gravity prevents muscle atrophy and bone decalcification.

1.5.2 Planetary Exploration

The concept of an atmospheric tethered probe can be carried even further into what is called "tethered aerobraking" [6,29]. An interplanetary spacecraft approaching a target planet can deploy a "tethered aerobraking" craft. The lower probe penetrates the upper atmosphere of the planet deep enough so that air drag slows the spacecraft from hyperbolic escape speed to orbital speed. This greatly reduces the amount of propellant required for planetary capture.

The use of tethers might also reduce the complexity and cost of asteroid and comet sampling missions. Instead of having to land on the target body, a spacecraft rendezvousing an asteroid or a comet can deploy a tethered sampling probe equipped with a penetrator [6,30]. The secondary probe penetrates the surface of the target, extracts a sample from the object, and returns to the "mother" craft as the tether is reeled back (Fig. 1.13). In this way, samples from various locations on the target, or from different bodies can be brought back to the Earth using a single spacecraft.

But that is not all: longer and stronger tethers can be anchored to asteroids to modify the trajectory of spacecraft [31,32]. In this manoeuvre called "tethered sling shot assist," a spacecraft approaching an asteroid at a high speed (1-3 km/s) deploys a tethered penetrator. The secondary probe anchors the system to the asteroid. The trajectory of the spacecraft is modified as it "swings-by" the anchor body. During the "tethered assist," samples can be extracted from the anchor body. At the end of the manoeuvre, the samples are brought back to the primary craft as the tether is reeled back for reuse. In this way, a single probe could sample up to 8 *NEA*'s (Near-Earth Asteroids) in a single mission.

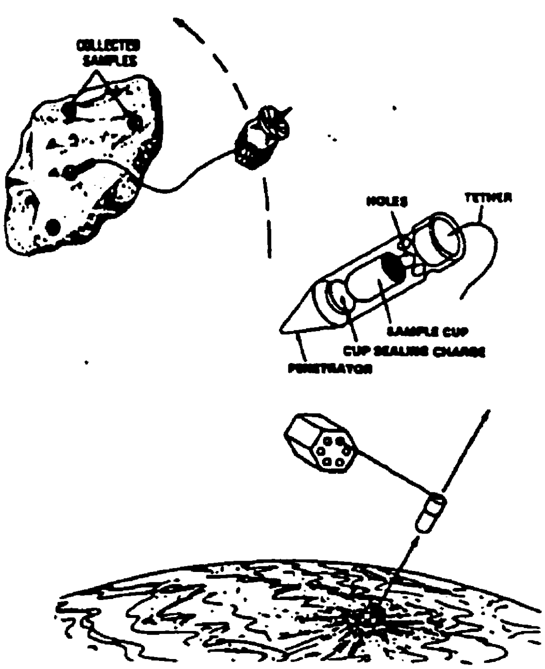

Fig. 1.13: Tethered Sampling Concept [6]

1.6 LITERATURE REVIEW OF ORBITAL MOTION

Keplerian motion assumes that the object of interest moves under the sole influence of the gravity of the attractor (the Earth). Other forces influencing the spacecraft trajectory are called perturbations because their effect on the motion of the system is smaller, but still noticeable. There exist several kinds of perturbations: air lift and drag, Earth asphericity effects, solar radiation pressure, lunisolar attraction, and electromagnetic forces.

The main effect of air lift and drag is the decay of the semi-major axis [6,33]. The decay rate depends on several factors such as altitude, ballistic coefficient, solar activity, etc. Although several interpolation and analytical formulae can estimate the lifetime of satellites [6,34], the exact calculation of this parameter requires very detailed models [35,36]. Using one such model, Warnock and Cochran [37] investigated the effect of several parameters like the semi-major axis, the inclination, the argument of latitude, and the tether length and diameter on the lifetime of tethered satellites. Earth asphericity perturbation forces, as the name suggests, result from the non-homogeneous mass distribution and aspherical shape of the Earth. The net effect of this perturbation is a drift in the ascending node (orientation of the orbital plane) and a drift in the argument of perigee (position of the perigee within the orbital plane) [6,38]. The impact of photons emitted by the Sun on the surface of a spacecraft also affects its trajectory. In fact, solar radiation pressure becomes stronger than air lift and drag for altitudes beyond 800 km [39]. This perturbation causes periodic changes in all of the orbital elements [33]. Lunisolar attraction is the combined interaction of the gravity forces of the Sun and of the Moon on a satellite. This perturbation force becomes non-negligible for altitudes above 26000 km [33]. Electromagnetic or Lorentz forces result from the motion of a conductive tether in the magnetic field of the Earth [6,8,24,25,26]. Depending on the magnitude and frequency of the tether current and on the position and attitude of the spacecraft, electromagnetic forces can influence any of the orbital elements and the orientation of the spacecraft.

1.7 LITERATURE REVIEW OF SPACE TETHER DYNAMICS

Tethered systems are usually stable during deployment. A control system is not required if the tether deployment rate is slow enough and if the initial orientation of the satellite is judiciously chosen. Kulla [40] determined the upper bound on the tether deployment rate that yields a stable deployment. On the other hand, the retrieval phase is intrinsically unstable; regardless of the tether retrieval rate. Bainum and Kumar [41] determined that the behaviour of the system during retrieval is more dependent on the initial roll than on the initial pitch of the system. Matters can become of even greater concern when the retrieval rate is large: the Coriolis acceleration hence imparted on the system causes further instabilities in pitch. Interested readers are referred to the work of Misra and Modi [42], who published a survey of papers on the dynamics and control of space tethered systems.

Although the station keeping phase is marginally stable, the atmospheric drag force shifts the equilibrium orientation of *librating tethered systems* [43]. Furthermore, air drag may even generate instabilities in long and stiff tethered systems due to atmospheric density variations along the cable [44,45,46,47].

Several control strategies were devised to stabilize the system during all the phases of flight. These strategies include tension control, length or reel rate control, offset control and aerodynamic control. As this thesis does not focus on the control of tethered systems, interested readers are again directed to the work of Misra and Modi [42] for more information on the topic.

Several computer models were developed to study the deployment, the station-keeping, and the retrieval of space tethered systems. These include the SKYHOOK model developed at the Smithsonian Astrophysical Observatory [48], the GTOSS model [49], the SPACE TETHER model [50] and the GEODYN model [10]. More recently, Schultz and Vigneron [51,52] have turned their attention on the long term dynamics of *spinning tethered systems* such as BOLAS.

1.8 LITERATURE REVIEW OF TETHER MATERIAL PROPERTIES

Although their impact on the trajectory of the spacecraft remains minor, tether material properties strongly influence the longitudinal oscillations of the tether. They also contribute to the slow decay of the librations of the system [10].

Previous experimental work on various tethers has shown that their properties vary considerably with the number and the intensity of the loading cycles. Angrilli et al. [53] have shown that the properties of composite tethers depend to a great extent on the history of the relative motion between the fibres and the layers of the cable. As the tether is cycled, the friction between the fibres and the layers effectively "packs" the tether. This increases stiffness and reduces damping. This mechanism partly explains why tether stiffness increases with the applied load. A higher load causes more tether "packing." Fanti et al. [54] determined that the stiffness of the TSS-1 tether increases quasi-logarithmically with load. NRL analysts [55] found that the TiPS tether behaves similarly. As far as the creep behaviour is concerned, there is little data available. However, since stress levels are very low, creep is usually not a concern.

Angrilli et al. [56] noticed an increase in stiffness and a large reduction in damping as the temperature decreases. They also found that the longitudinal loss factor of the TSS tether seems to be independent of the frequency of the oscillations. Finally, He and Powell [57] proposed an interpolation formula to determine the longitudinal damping of the TSS-1 tether as a function of tether length.

1.9 OBJECTIVES AND OUTLINE OF THE THESIS

1.9.1 Objectives of the Thesis

The major endeavour of this work is the development, implementation and qualification of a detailed computer model capable of analysing and predicting the long-term dynamics of tethered spacecraft. The second objective of this thesis is to use the above model to better understand the long term dynamics and stability of space tethered systems.

The effects of air lift and drag, Earth oblateness and electromagnetic perturbation forces are given special attention.

1.9.2 Outline of the Thesis

This thesis first presents the mathematical equations behind the present model (Chapter 2). The algorithm based on this model determines the effect of perturbation forces and torques on the orbital, attitude, thermal, and longitudinal dynamics of tethered systems. The perturbation forces taken into account include atmospheric lift and drag, Earth asphericity, solar radiation pressure, lunisolar attraction, and electromagnetic forces.

Chapter 3 discusses a series of experiments on tether material properties carried out at the University of British Columbia and at the Chapman Space Centre of the Canadian Space Agency. The results of these experiments are used to estimate the longitudinal and torsional stiffness, and the longitudinal and torsional damping of the tether used in the TiPS mission and in the BOLAS proposal.

Chapter 4 focuses on the effect of air drag and Earth oblateness forces on the dynamics of *librating* tethered systems. As an example, the behaviour of the TiPS spacecraft is examined in detail. On the other hand, the fifth chapter examines the effect of electromagnetic forces on the orbital motion and on the librations of tethered systems. Chapter 6 discusses the long term behaviour of *spinning* tethered systems such as BOLAS. Finally, Chapter 7 presents some concluding remarks and suggestions for future work.

CHAPTER 2

THEORETICAL CONSIDERATIONS

2.1 DESCRIPTION OF THE SYSTEM

The system under consideration consists of two satellites of mass m_1 and m_2 linked by an elastic tether of mass m_t (Fig. 1.1). The tether is assumed to remain straight. This is done to keep the dynamical model manageable, and because transverse oscillations are not likely to have significant effect on the long-term dynamics of the system. The state of the spacecraft is described by a set of variables that fix the position and velocity of the spacecraft, its attitude (orientation), its temperature, and the longitudinal elongation of the tether. The position and velocity of the system are obtained from its orbital elements (a,P_1,P_2,Q_1,Q_2,L^*). The attitude of the tether is described by the in-plane angle: pitch α and out-of-plane angle: roll γ. The rotation of the system about an axis parallel to the tether line (yaw) is assumed to have no effect on the dynamics of the system. The longitudinal elongation of the tether is described by its strain ϵ. The transverse oscillations of the tether are not considered in this thesis. Finally, the tether temperature T, constitutes the final variable required to fix the state of the system.

Throughout this thesis, the deployed length of the tether is denoted by l, and its radius by r_t. The longitudinal stiffness and damping constant of the tether are EA and β respectively. The relevant thermal properties of the tether include its emissivity ε_t, heat capacity κ, and coefficient of thermal expansion ξ. The atmospheric lift and drag on the system are strongly dependent on the tangential and normal accommodation coefficients of each surface (σ_t and σ_n). These two parameters describe how the incoming flow of air interacts with the surface of the object. On the other hand, the solar absorptivity and diffuse and specular reflectivity (σ_s, σ_{rd}, σ_{rs}) describe the interaction between the system and the photons emitted by the Sun.

A thorough analysis of the motion of tethered systems requires three coordinate frames: a vernal coordinate system, an orbital coordinate system and a spherical coordinate system. The vernal coordinate system OXYZ is well suited to describe the position and velocity of the centre of mass of the system (Fig. 2.1). The origin of this inertial system of coordinates rests at the centre of the Earth. The Z-axis points in the direction of the celestial north pole, the X-axis points toward the vernal equinox, and the Y-axis completes the right-handed set OXYZ.

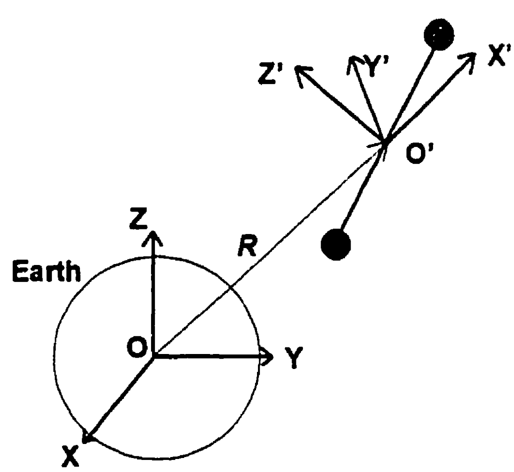

Fig. 2.1: Vernal and Orbital Coordinate Systems

The orbital coordinate system O'X'Y'Z' (Fig. 2.1) proves particularly useful for describing the spacecraft attitude and to calculate most of the perturbation forces. The origin of this non-inertial coordinate system is the centre of mass of the tethered spacecraft. The X'-axis is parallel to the local vertical, that is, the position vector of the system centre of mass measured from the centre of the Earth ***R***. The Z'-axis points in the direction of the angular momentum vector of the spacecraft orbit. Finally, the Y'-axis completes the right-handed frame O'X'Y'Z'. As seen in Fig. 2.2, the angle between the projection of m_2 on the X'Y'-plane and the X'-axis gives the pitch of the system (α). Roll is defined as the angle between the position vector of m_2 relative to O' and its projection on the X'Y'-plane.

The spherical coordinate system (R,λ,ϕ) is a non-inertial and right-handed frame with its origin (O") at the centre of mass of the system (Fig. 2.3). The $\mathbf{e}_R$ axis is parallel to the local vertical, the $\mathbf{e}_\lambda$ axis points eastward in the direction of increasing longitude, and the $\mathbf{e}_\phi$ axis lies in the direction of increasing latitude.

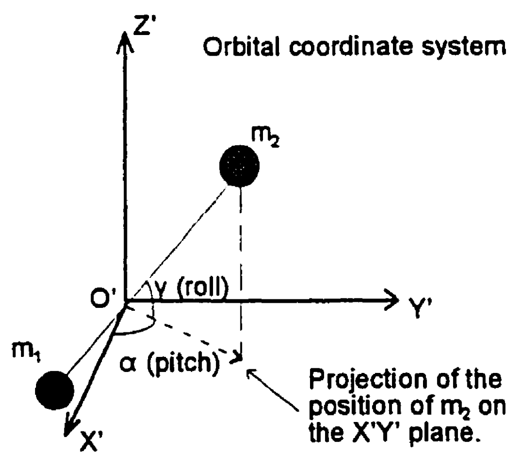

Fig. 2.2: Definition of the Pitch and Roll Angles

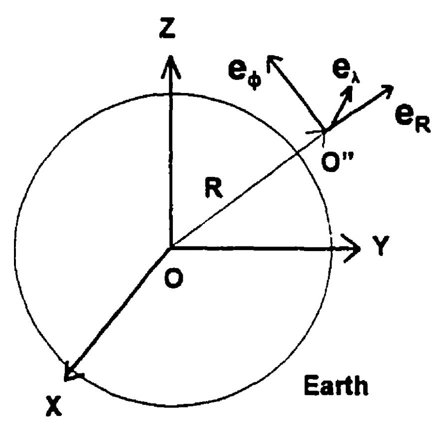

Fig. 2.3: Vernal and Spherical Coordinate Systems

Most of the computations to be performed in this thesis make use of the orbital coordinate system. Vectors in vernal and spherical coordinate frames can be rotated to the orbital coordinate frame using the following transformation equations:

$$\{\boldsymbol{R}\}_{orb} = [A]\{\boldsymbol{R}\}_{ver} \tag{2.1}$$

$$\{\boldsymbol{R}\}_{orb} = [A][B]\{\boldsymbol{R}\}_{sph} \tag{2.2}$$

where matrices *[A]* and *[B]* are given by

$$[A]=\begin{bmatrix} \cos\Omega\cos(u)-\sin\Omega\sin(u)\cos(i) & -\cos\Omega\sin(u)-\sin\Omega\cos(u)\cos(i) & \sin\Omega\sin(i) \\ \sin\Omega\cos(u)+\cos\Omega\sin(u)\cos(i) & -\sin\Omega\sin(u)+\cos\Omega\cos(u)\cos(i) & -\cos\Omega\sin(i) \\ \sin(u)\sin(i) & \cos(u)\sin(i) & \cos(i) \end{bmatrix} \quad (2.3)$$

$$[B]=\begin{bmatrix} \cos\lambda\cos\phi & -\sin\lambda & -\sin\lambda\sin\phi \\ \sin\lambda\cos\phi & \cos\lambda & -\sin\lambda\sin\phi \\ \sin\phi & 0 & \cos\phi \end{bmatrix} \quad (2.4)$$

where u is the argument of latitude ($u=\theta+\omega$), Ω represents the right ascension of the ascending node, i is the orbital inclination, λ denotes the eastern longitude of the object from the vernal equinox, and ϕ gives the latitude.

2.2 PERTURBATIONS OF THE ORBITAL ELEMENTS

In the absence of disturbing forces, any satellite would keep orbiting along a conic section orbit of fixed dimensions and orientation. As explained in the introduction, many factors perturb the motion of satellites. Predicting the state of a satellite over a long period of time requires that one take all these factors into account. The exact trajectory of a spacecraft is determined by integrating the influence of the perturbative forces over time. To that end, perturbation equations must be obtained for each orbital element. Such equations were derived for the classical elements by Lagrange, but they become singular for circular ($e\rightarrow0$) and equatorial ($i\rightarrow0$) orbits [58]. The classical orbital elements are the semi-major axis (a), the eccentricity (e), the inclination (i), the true anomaly (θ), the argument of perigee (ω), and the right ascension of the ascending node (Ω) (Fig. 2.4).

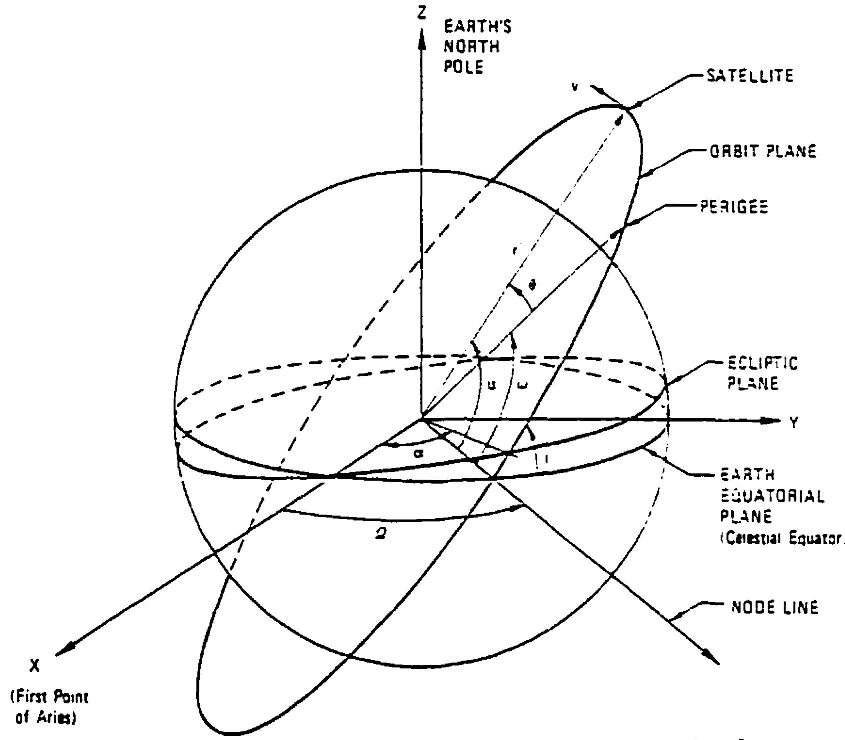

Fig. 2.4: The Clas.. 'cal Orbital Elements [33]

A different set of elements called the equinoctial elements $(a, P_1, P_2, Q_1, Q_2, L)$ is more robust for equatorial and circular orbits [58]. However, the determination of the mean longitude ($L=M+\omega+\Omega$) is computationally time-consuming. To solve this problem, Warnock and Cochran [37] introduced a slightly different formulation which relies on the true longitude ($L^*=\theta+\omega+\Omega$) of the satellite. Based on this, the author devised an even more computationally efficient algorithm to propagate the spacecraft trajectory using the "modified equinoctial elements". One can convert the classical orbital elements to the modified equinoctial elements using the following relations:

$$\begin{aligned}
P_1 &= e * \sin(\omega+\Omega) \\
P_2 &= e * \cos(\omega+\Omega) \\
Q_1 &= \tan(i/2)\sin(\Omega) \\
Q_2 &= \tan(i/2)\cos(\Omega) \\
L^* &= \theta+\omega+\Omega
\end{aligned} \tag{2.5}$$

On the other hand, the modified equinoctial elements can be converted to classical elements by using the following equations:

$$
\begin{aligned}
e &= \sqrt{P_1^2 + P_2^2} \\
i &= 2\arctan\left(\sqrt{Q_1^2 + Q_2^2}\right) \\
\Omega &= \arctan(Q_1/Q_2) \\
\omega &= \arctan(P_1/P_2) - \Omega \\
\theta &= L^{*} - \omega - \Omega
\end{aligned}
\tag{2.6}
$$

The perturbative equations for the modified equinoctial elements can be derived from Lagrange's perturbation equations and are:

$$
\begin{aligned}
\frac{da}{dt} &= \frac{2a^2}{h}\left[[P_2\sin(L^{*}) - P_1\cos(L^{*})]f_{x'} + \frac{p}{R}f_{y'}\right] \\
\frac{dP_1}{dt} &= \frac{R}{h}\left[-\frac{p}{R}\cos(L^{*})f_{x'} + [P_1 + (1+\frac{p}{R})\sin(L^{*})]f_{y'} - P_2[Q_1\cos(L^{*}) - Q_2\sin(L^{*})]f_{z'}\right] \\
\frac{dP_2}{dt} &= \frac{R}{h}\left[\frac{p}{R}\sin(L^{*})f_{x'} + [P_2 + (1+\frac{p}{R})\cos(L^{*})]f_{y'} + P_1[Q_1\cos(L^{*}) - Q_2\sin(L^{*})]f_{z'}\right] \\
\frac{dQ_1}{dt} &= \frac{R}{2h}[1 + Q_1^2 + Q_2^2]\sin(L^{*})f_{z'} \\
\frac{dQ_2}{dt} &= -\frac{R}{2h}[1 + Q_1^2 + Q_2^2]\cos(L^{*})f_{z'} \\
\frac{dL^{*}}{dt} &= \frac{h}{R^2} + \frac{R[\sin(\theta+\omega)\tan(i/2)f_{z'}]}{h}
\end{aligned}
\tag{2.7}
$$

where R denotes the geocentric altitude, and $f=(f_{x'},f_{y'},f_{z'})$ is the perturbative acceleration expressed in the orbital coordinate frame. For maximum accuracy, the model in this thesis discretizes the system into k+2 elements: two for the end-bodies and k elements along the tether. The model then calculates the perturbative force on each element. The sum of these perturbative forces is divided by the total mass of the system to obtain the net perturbative acceleration of the centre of mass of the system ($f_{x'}$, $f_{y'}$, $f_{z'}$). In the above equations, h and $p=a(1-e^2)$ denote the specific angular momentum and semi latus rectum of the spacecraft orbit respectively. The first five equations in (2.7) were derived by Broucke [58]. The perturbation equation for the true longitude was derived by the author. The above differential equations have no singularities, except for linear trajectories (h=0, a trivial case) and for perfectly retrograde orbits (i=π).

From an implementation point of view, the accuracy of numerical analysis software is optimal when all the variables integrated have roughly the same order of magnitude. For this reason, the semi-major axis is non-dimensionalized through division by the radius of the Earth.

$$a_{ND}=\frac{a}{R_{\oplus}} \tag{2.8}$$

2.3 LIBRATIONAL AND LONGITUDINAL DYNAMICS OF TETHERED SATELLITES

2.3.1 Lagrangian of the System

The system under consideration contains two masses and a longitudinally flexible tether whose actual length depends on the deployed tether length and on mechanical and thermal strains. The system is free to librate in the orbital plane (pitch) or out of the orbital plane (roll). Modi et al. [59] provide a very detailed expression for the Lagrangian of tethered systems with a rigid cable. Based on this, one can derive expressions for the kinetic and potential energy of a tethered system with a longitudinally flexible tether:

$$\begin{gathered} T=\frac{m_e l_o^2(1+\epsilon)^2}{2}[(\dot{\theta}+\dot{\alpha})^2\cos^2\gamma+\dot{\gamma}^2]+\frac{m^*}{2}[\dot{l}_o(1+\epsilon)+l_o\dot{\epsilon}]^2 \\ V=\frac{m_e l_o^2(1+\epsilon)^2\mu(1-3\cos^2\alpha\cos^2\gamma)}{2R^3}+\frac{EAl_o\epsilon^2}{2} \end{gathered} \tag{2.9}$$

where μ is the gravitational parameter of the Earth (μ=GM$_{\oplus}$) and l_o is the length of the tether subjected to thermal strain

$$l_o=l(1+\xi\Delta T) \tag{2.10}$$

The mass parameters m_e and m^* are given by

$$m_e=(m_1+\frac{m_t}{2})(\frac{m_2+m/2}{m})-\frac{m_t}{6}$$
$$m^*=\frac{m_1(m_2+m_t)}{m} \tag{2.11}$$

where m is the total mass of the system (m_1 + m_2 + m_t). The various terms in equation (2.9) denote the kinetic energy due to tether libration and extension, the potential energy due to gravity and the elastic energy due to tether extension, respectively. The presence of $d\theta/dt$ and of μ/R^3 indicate that the librational and longitudinal dynamics of the system are coupled with orbital motion.

2.3.2 System Librations

Through application of Lagrange's method, the equations of motion for pitch and roll can be obtained as

$$(\ddot{\theta}+\ddot{\alpha})+2(\dot{\theta}+\dot{\alpha})[\frac{\bar{m}\dot{l}_o}{m_e l_o}-\dot{\gamma}\tan\gamma+\frac{\dot{\epsilon}}{(1+\epsilon)}]+\frac{3\mu\sin2\alpha}{2R^3}=\frac{Q_\alpha}{m_e l_o^2\cos^2\gamma(1+\epsilon)^2} \tag{2.12}$$

$$\ddot{\gamma}+2\dot{\gamma}[\frac{\bar{m}\dot{l}_o}{m_e l_o}+\frac{\dot{\epsilon}}{(1+\epsilon)}]+\frac{\sin2\gamma}{2}[(\dot{\theta}+\dot{\alpha})^2+\frac{3\mu\cos^2\alpha}{R^3}]=\frac{Q_\gamma}{m_e l_o^2(1+\epsilon)^2} \tag{2.13}$$

where Q_α and Q_γ are the generalized forces in the pitch and roll generalized coordinates respectively, and $\bar{m}$ is defined as

$$\bar{m}=\frac{m_1(m_2+m/2)}{m} \tag{2.14}$$

The stable orientation for tethered satellites is the "gravity gradient" configuration. It occurs when $\alpha=\gamma=0,\pi$; that is, when the system is perfectly aligned with the local vertical. For circular orbits, the frequency of small oscillations about the local vertical is $\sqrt{3}\omega_{orb}$ and $2\omega_{orb}$ for pitch and roll, respectively [42]. However, the libration frequency decreases drastically when libration amplitudes become large. This phenomenon is caused by non-linearities in the equations of motion and is similar to the behaviour of simple pendula.

2.3.3 Longitudinal Oscillations

The equation governing the tether strain is

$$\begin{aligned}&\dot{m}[\dot{l}_o(1+\epsilon)+l_o\dot{\epsilon}]+m^*[\ddot{l}_o(1+\epsilon)+2\dot{l}_o\dot{\epsilon}+l_o\ddot{\epsilon}]+EA\epsilon+\beta\dot{\epsilon}\\&-m_el_o(1+\epsilon)[(\dot{\theta}+\dot{\alpha})^2\cos^2\gamma+\dot{\gamma}^2+\frac{\mu}{R^3}(3\cos^2\gamma\cos^2\alpha-1)]=\frac{Q_\epsilon}{l_o}\end{aligned} \tag{2.15}$$

In equation (2.15), Q_ϵ denotes the generalized force corresponding to the generalized coordinate ϵ and the β term accounts for the visco-elastic damping of the tether [50]. The natural frequency of the longitudinal oscillations in the gravity gradient orientation can be approximated using equation (2.15)

$$\omega_{long}=\sqrt{\frac{EA}{lm^*}} \tag{2.16}$$

For most cases of interest, the strain and strain rate of the tether are much smaller in magnitude than the other variables to be integrated. For this reason, the software implementation of the present model utilizes non dimensionalized strain and strain rate variables. These quantities are obtained in the following way:

$$\epsilon_{ND} = \frac{EA\epsilon}{m_e l \omega_{orb}^2}$$
$$\frac{d\epsilon_{ND}}{d(nt)} = \frac{EA\dot{\epsilon}}{m_e l \omega_{orb}^3} \tag{2.17}$$

where t denotes time and n is the mean motion of the spacecraft (number of revolutions per day).

2.3.4 Tether Tension

The tether tension [50] is given by

$$T = EA\epsilon + \beta\dot{\epsilon} \tag{2.18}$$

In most cases, the tension can be approximated by $EA\epsilon$, where the strain depends on several factors like the altitude and the orientation of the system.

2.4 DETERMINATION OF THE GENERALIZED FORCES

The equations of orbital, librational and longitudinal motion of the system (Sections 2.2 and 2.3) require the determination of the overall acceleration vector f, and of the generalized external forces Q_α, Q_γ, and Q_c. For maximum accuracy, the present formulation discretizes the spacecraft into k+2 elements: two for the end bodies and k elements along the tether line. The model then calculates the total perturbative force on each element as:

$$F_j = F_{air_j} + F_{Sun_j} + F_{Mag_j} + m_j[f_{a_j} + f_{\oplus_j} + f_{\mathbb{C}_j}], \tag{2.19}$$

where F_{air} is the aerodynamic force; F_{Sun} denotes the solar radiation pressure force, F_{Mag} designates the electromagnetic force; and f_a, $f_\oplus$, and $f_{\mathbb{C}}$ represent the acceleration due to the

Earth's asphericity and lunisolar attraction, respectively. These forces and accelerations are modelled in section 2.5. The sum of all perturbative forces ΣF_j is divided by the total mass of the system to obtain the net perturbative acceleration of the system f.

To determine the generalized forces on the system, one must first determine the position of the centre of mass of the system at any instant. To do this, let us define l_{tot} as the total length of the tether:

$$l_{tot} = l(1+\epsilon)(1+\xi\Delta T) = l_o(1+\epsilon) \tag{2.20}$$

The two terms in parentheses account for the mechanical and thermal strains. l_o denotes the "thermally" strained tether length.

The distance δ between the centre of the first end body and the centre of mass of the system is given by (Fig. 2.5).

$$\delta = \frac{m_2[l_{tot} + (c_1 + c_2)/2] + m_t[l_{tot} + c_1]/2}{m} \tag{2.21}$$

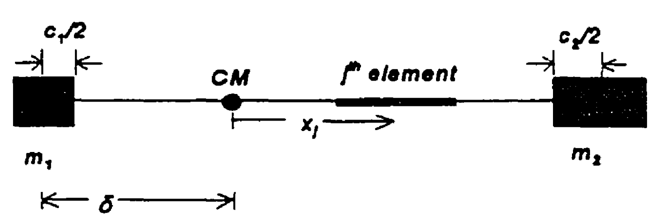

Fig. 2.5: System Discretization

Defining x_j as the position of the centre of the j^{th} element with respect to the centre of mass of the system (Fig. 2.5), we have, for the first end body (j=1):

$$x_1 = -\delta \tag{2.22a}$$

for the tether ($2 \le j \le k+1$):

$$x_j = \frac{(2j-3) l_{tot}}{2k} + \frac{c_1}{2} - \delta \tag{2.22b}$$

and for the second end body ($j=k+2$):

$$x_{k+2} = l_{tot} + \frac{c_1 + c_2}{2} - \delta \tag{2.22c}$$

The generalized forces are obtained from basic principles:

$$Q_i = \sum_{j=1}^{k+2} \boldsymbol{F}_j \cdot \frac{\partial \boldsymbol{R}_j}{\partial q_i} \tag{2.23}$$

where F_j is the total perturbative force on the j^{th} element of the system, R_j is the vector joining the centre of mass of the system to the centre of the j^{th} element. This vector is given in orbital coordinates by

$$\{\vec{\boldsymbol{R}}_j\}_{orb} = \begin{bmatrix} x_j \cos(\gamma)\cos(\alpha) \\ x_j \cos(\gamma)\sin(\alpha) \\ x_j \sin(\gamma) \end{bmatrix} \tag{2.24}$$

The next task is to find the partial derivatives of R_j with respect to α, γ and ϵ. For pitch and roll, this can be done by direct partial differentiation of equation (2.24)

$$\{\frac{\partial \vec{\boldsymbol{R}}_j}{\partial \alpha}\}_{orb} = \begin{bmatrix} -x_j \sin(\alpha)\cos(\gamma) \\ x_j \cos(\alpha)\cos(\gamma) \\ 0 \end{bmatrix} \tag{2.25}$$

$$\{\frac{\partial \vec{R}_j}{\partial \gamma}\}_{orb} = \begin{bmatrix} -x_j\, cos(\alpha)\, sin(\gamma) \\ -x_j\, sin(\alpha)\, sin(\gamma) \\ x_j\, cos(\gamma) \end{bmatrix} \tag{2.26}$$

On the other hand, obtaining the partial derivative of R_j with respect to ϵ is slightly more involved. Using the chain rule, we have

$$\frac{\partial R_j}{\partial \epsilon} = \frac{\partial R_j}{\partial x_j}\frac{\partial x_j}{\partial l_{tot}}\frac{\partial l_{tot}}{\partial \epsilon} = \frac{l_o R_j}{x_j}\frac{\partial x_j}{\partial l_{tot}} \tag{2.27}$$

The partial derivative of x_j with respect to l_{tot} can be determined using equation (2.22). For the first end body, we have:

$$\frac{\partial x_1}{\partial l_{tot}} = \frac{-(m_2 + m_t/2)}{m} \tag{2.28a}$$

for the tether elements:

$$\frac{\partial x_j}{\partial l_{tot}} = \frac{2j-3}{2k} - \frac{(m_2 + m_t/2)}{m} \tag{2.28b}$$

for the second end mass:

$$\frac{\partial x_{k+2}}{\partial l_{tot}} = \frac{(m_1 + m_t/2)}{m} \tag{2.28c}$$

Therefore, the generalized force in the pitch coordinate is

$$Q_\alpha = \sum_{j=1}^{k+2} x_j[-F_{x'j}\sin(\alpha)\cos(\gamma) + F_{y'j}\cos(\alpha)\cos(\gamma)] \tag{2.29a}$$

where x_j is given by equation (2.22). The generalized force for roll is

$$Q_{\gamma}=\sum_{j=1}^{k+2} x_j[-F_{x'j}\cos(\alpha)\sin(\gamma)-F_{y'j}\sin(\alpha)\sin(\gamma)+F_{z'j}\cos(\gamma)] \tag{2.29b}$$

Finally, the generalized force for strain is

$$Q_{\epsilon}=l_o\sum_{j=1}^{k+2} \frac{\partial x_j}{\partial l_{tot}}[F_{x'j}\cos(\gamma)\cos(\alpha)+F_{y'j}\cos(\gamma)\sin(\alpha)+F_{z'j}\sin(\gamma)] \tag{2.29c}$$

where the partial of x_j with respect to l_{tot} is given by equation (2.28). Here $F_{x'j}$, $F_{y'j}$ and $F_{z'j}$ are components of F_j along orbital coordinate axes.

2.5 PERTURBATION FORCES

2.5.1 Aerodynamic Forces

2.5.1.1 Aerodynamic Forces

Atmospheric lift and drag drastically modify the trajectory of satellites in LEO. Their most dramatic effect is the decay of the semi-major axis. The decay rate increases more or less exponentially as the altitude decreases. This phenomenon becomes a true concern for altitudes below 500 km. Although they considered the effects of aerodynamic drag [43,48], most of the previous analyses of tether dynamics have not considered aerodynamic lift. Nonetheless, recent studies [44,61] have shown that lift has a significant effect on the attitude dynamics of tethered systems. The present formulation accounts for the combined effect of both air lift and drag.

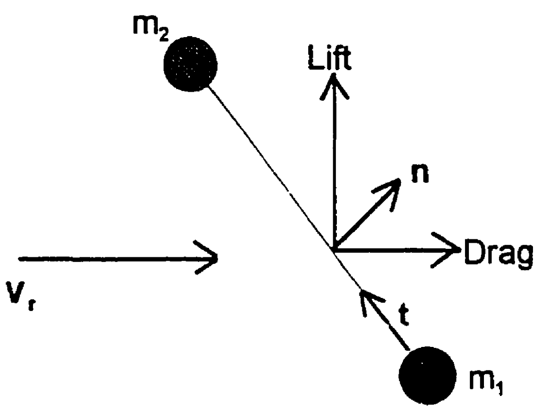

Fig. 2.6: Atmospheric Lift and Drag on a Tethered Spacecraft

Hughes [35] presents a particularly detailed derivation of the air lift and drag force acting on a spacecraft (Fig. 2.6). He bases his analysis on the free-molecular flow model. This model assumes that the mean free path of the air molecules is much larger than the size of the spacecraft. As a result, the effect of collisions between air molecules and the spacecraft is greater than the effect of collisions among air molecules. This situation applies in rarefied density environments like LEO. Hughes states that in such cases, the combined lift and drag force on a surface due to its interaction with the atmosphere is given by

$$F_{air}=\rho_{air}V_r^2[\sigma_t A_p^{\ D}v_r+\sigma_n(\frac{V_b}{V_r})A_p^{\ D}+(2-\sigma_n-\sigma_t)A_{pp}^{\ D}] \tag{2.30}$$

where ρ_{air} is the atmospheric density, v_r is a unit vector in the direction of the velocity of the local atmosphere relative to the surface and V_r is the speed of the atmosphere with respect to the surface. A_p^D, A_p^D and A_{pp}^D are called *shape factors*. These parameters depend on the shape and size of the spacecraft surface. σ_n and σ_t are the accommodation coefficients in the normal and tangential direction respectively. The value of the two accommodation coefficients usually varies between 0.85 and 0.95. The limiting cases of specular and diffuse reflection correspond to $\sigma_n=\sigma_t=0$ and $\sigma_n=\sigma_t=1$, respectively. V_b is the speed of the air molecules at the temperature of the tether T. In other words,

$$V_b = \sqrt{\frac{\pi R_u T}{2m_m}} \tag{2.31}$$

where R_u is the universal gas constant and m_m is the molecular mass of the air.

As the accommodation coefficients usually near unity (diffuse reflection) and since $V_b << V_r$, the first term in equation (2.30) dominates over the other two. As a result, atmospheric forces predominantly act in the direction opposite to that of the spacecraft motion. In other words, the effect of air drag is much more important than that of atmospheric lift. Indeed, the lift to drag ratio of tethered systems (L/D) is of the order of 1/10 [6]. This tends to decay the orbit of satellites.

2.5.1.2 Shape Factors

As mentioned earlier, the shape factors A_p^D, $\boldsymbol{A}_p^D$ and $\boldsymbol{A}_{pp}^D$ depend on the shape and size of the spacecraft surface. They are given by

$$\begin{aligned} A_p^D &\equiv \iint H(\cos\alpha)\cos\alpha\, dA \\ \boldsymbol{A}_p^D &\equiv \iint H(\cos\alpha)\cos\alpha\, d\boldsymbol{A} \\ \boldsymbol{A}_{pp}^D &\equiv \iint H(\cos\alpha)\cos^2\alpha\, d\boldsymbol{A} \end{aligned} \tag{2.32}$$

where $H(x)$ is the Heaviside function [35]. This function is 1 if $x \geq 0$ and 0 if $x<0$. The Heaviside accounts for the absence of air lift and drag on surfaces unexposed to the flow. Note that A_p^D is a scalar, while $\boldsymbol{A}_p^D$ and $\boldsymbol{A}_{pp}^D$ are both vector quantities. All of the above integrals are surface integrals and in general, A_p^D is not simply the magnitude of $\boldsymbol{A}_p^D$. The shape factors of a tether element of radius r_t and length dx are given by

$$\begin{aligned} A_{p_t}^D &= 2r_t(\boldsymbol{v}_r \cdot \boldsymbol{n})dx \\ \boldsymbol{A}_{p_t}^D &= \frac{\pi}{2} r_t(\boldsymbol{v}_r \cdot \boldsymbol{n})\boldsymbol{n}dx \\ \boldsymbol{A}_{pp_t}^D &= \frac{4}{3} r_t(\boldsymbol{v}_r \cdot \boldsymbol{n})^2\boldsymbol{n}dx \end{aligned} \tag{2.33}$$

where $\boldsymbol{n}$ is a unit vector that lies in the $\boldsymbol{t}$-$\boldsymbol{v}_r$ plane and is perpendicular to the tether (Fig. 2.6). $\boldsymbol{t}$ is a unit vector along the tether line. Most of the calculations performed in this thesis assume that the end bodies are shaped like square prisms *sp*. As shown in Figure 2.7, *a* and *c* designate the width and depth of each subsatellite.

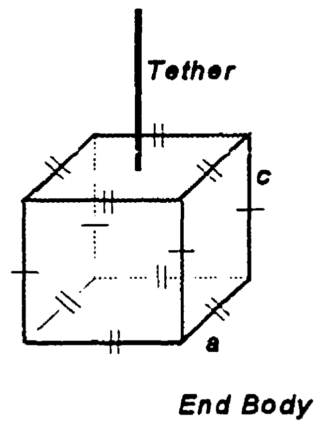

Fig. 2.7: View of a Square Prism Subsatellite

Since the interaction between a square prism and the surrounding flow of air depends on the orientation of the end mass around the tether axis, the shape factors must be averaged over one complete yaw rotation. Hence, the averaged shape factors of a square prism are given by:

$$
\begin{aligned}
A_{p_{sp}}^{D} &= \frac{4}{\pi} ac(\boldsymbol{v}_r \cdot \boldsymbol{n}) + a^2 |(\boldsymbol{v}_r \cdot \boldsymbol{t})| \\
\boldsymbol{A}_{\boldsymbol{p}_{sp}}^{D} &= ac(\boldsymbol{v}_r \cdot \boldsymbol{n})\boldsymbol{n} + a^2 (\boldsymbol{v}_r \cdot \boldsymbol{t})\boldsymbol{t} \\
A_{pp_{sp}}^{D} &= \frac{8ac}{3\pi} (\boldsymbol{v}_r \cdot \boldsymbol{n})^2 \boldsymbol{n} + a^2 (\boldsymbol{v}_r \cdot \boldsymbol{t})^2 \boldsymbol{t}
\end{aligned}
\tag{2.34}
$$

On one particular occasion, the first two shape factors of a sphere and of a cylinder will also be required:

$$
\begin{aligned}
A^D_{p_{sph}} &= \pi r^2_{sph} \\
\boldsymbol{A}^D_{p_{sph}} &= \pi r^2_{sph} \boldsymbol{v}_r \\
A^D_{p_{cyl}} &= 2 r_{cyl} l_{cyl} (\boldsymbol{v}_r \cdot \boldsymbol{n}) + \pi r^2_{cyl} |(\boldsymbol{v}_r \cdot \boldsymbol{t})| \\
\boldsymbol{A}^D_{p_{cyl}} &= \frac{\pi}{2} r_{cyl} l_{cyl} (\boldsymbol{v}_r \cdot \boldsymbol{n}) \boldsymbol{n} + \pi r^2_{cyl} (\boldsymbol{v}_r \cdot \boldsymbol{t}) \boldsymbol{t}
\end{aligned}
\qquad (2.35)
$$

where r_{sph}, r_{cyl}, l_{cyl} denote the sphere radius, the cylinder radius, and the cylinder length, respectively.

2.5.1.3 Atmospheric Density

Spacecraft flying in LEO encounter a relatively "dense" atmosphere. As a result, their orbit decays faster than that of satellites in higher orbits. In fact, the determination of the atmospheric density represents the most important issue in the determination of air lift and drag forces. A large number of previous studies in tether dynamics assume that the atmospheric density follows an exponential variation [43,47,48,51]. Although this approximation may lead to analytical solutions, it fails to account for the very large variations in atmospheric density caused by solar and geomagnetic activity, latitude, etc. These factors can cause the atmospheric density to vary by as much as 2 or 3 orders of magnitude. As an example, Figure 2.8 shows the influence of the solar activity (exospheric temperature) on the atmospheric density. Therefore, great efforts are made to find a very reliable atmospheric density model. The present formulation relies on one of the most accurate atmospheric density models available: the Jacchia 77 model [36]. This model gives the density and molar mass of the ambient air as a function of altitude, solar activity, geomagnetic activity, latitude, Sun-satellite angle, and seasonal variations. The solar activity and geomagnetic activity indices are available via internet on the WDC (World Data Centre) webpage [62].

2.5.1.4 Earth Oblateness

The oblateness of the Earth also influences lift and drag forces on a spacecraft. As the planet is not a perfect sphere, but an ellipsoid, the *geodetic altitude* (altitude above the ground) of an object varies with the geocentric altitude as well as with the latitude (Fig. 2.9).

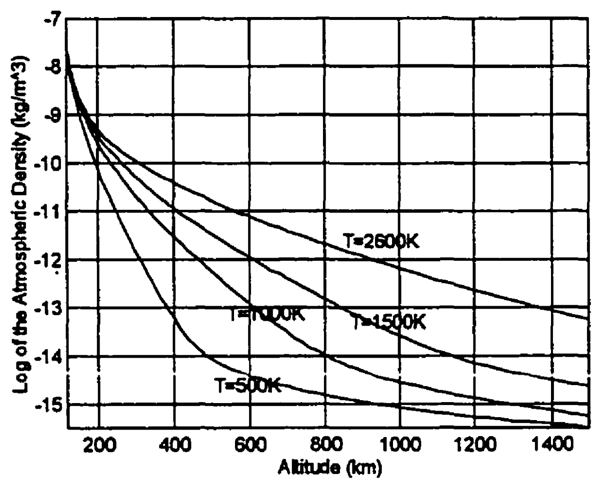

Fig. 2.8: Dependence of the Atmospheric Density on the Solar Activity

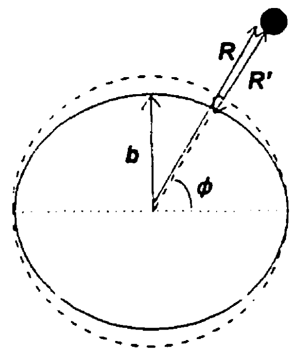

Fig. 2.9: Geodetic Altitude of a Spacecraft

For example, the polar radius of the Earth is approximately 21.4 km smaller than the equatorial radius. This variation in altitude causes a variation in atmospheric density and hence in lift and drag. For any geocentric altitude and latitude, the geodetic altitude is given by

$$R' = R - \frac{b}{\sqrt{1 - \epsilon_{\oplus}^2 \cos^2\phi}} \tag{2.36}$$

where R is the geocentric altitude, R' is the geodetic altitude, b is the polar radius of the Earth, ϕ is the latitude, and $\epsilon_{\oplus}$ is the eccentricity of the surface of the Earth [63].

The effect of Earth oblateness on the lifetime of tethered satellites has been studied in detail by Warnock and Cochran [37]. They noticed that the orbit of polar satellites decays much slower than that of equatorial spacecraft. To explain this phenomenon, they pointed out that the geodetic altitude increases near the poles. This in turn reduces the average atmospheric density and air drag on the spacecraft.

2.5.1.5 Rotation of the Earth

The last factor to influence the lift and drag forces on a spacecraft is the rotation of the Earth. Few earlier studies have considered this factor [2,37]. In equation (2.30), V_r

designates the velocity of the local atmosphere relative to the spacecraft. If the effect of the rotation of the Earth is neglected, $\boldsymbol{V_r}$ is simply $-\boldsymbol{V_s}$ (the negative of the spacecraft velocity). Keshmiri [2], and Warnock and Cochran [37], who accounted for the rotation of the atmosphere, assumed that its rotational rate equals the rotational rate of the Earth. But King-Hele [64], who studied the speed of winds in the upper atmosphere, has pointed out that the rotational rate of the atmosphere varies with the altitude (Fig.2.10). In Figure 2.10, the rotational rate is non-dimensionalized upon division by the rotational rate of the Earth. The velocity of the local atmosphere relative to the spacecraft is then

$$V_r = \omega_{atm} x R - V_s \tag{2.37}$$

From equation (2.37), neglecting the influence of atmospheric rotation leads to an overestimation of air drag for direct orbits (i<90°). The opposite holds for retrograde orbits (i>90°). This deduction was verified numerically by Warnock and Cochran [37].

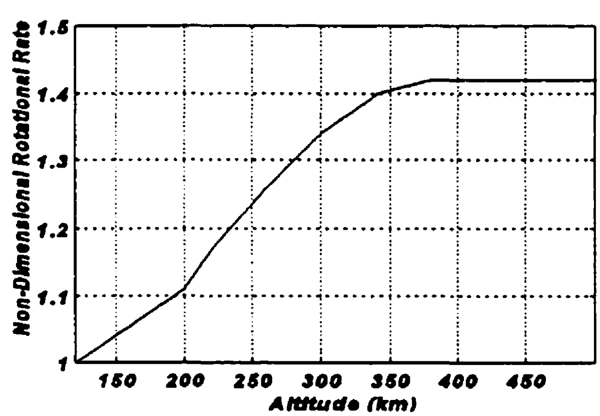

Fig. 2.10: Rotational Rate of the Atmosphere as a Function of the Altitude

2.5.1.6 Analytical and Empirical Lifetime Approximations

Several analytical and empirical formulae have been devised to estimate the orbit decay rate and lifetime of LEO satellites subjected to air drag. For example, Boden [34] presents the following analytical orbit decay model:

$$\frac{da}{dt} \approx \frac{-2\pi\sqrt{a\mu}\rho_{air} e^{-\frac{ae}{H}}[I_0+2eI_1]}{\beta^*}$$
$$\frac{de}{dt} \approx \frac{-2\pi\sqrt{\mu}\rho_{air} e^{-\frac{ae}{H}}[I_1+e(I_0+I_2)/2]}{\sqrt{a}\beta^*} \tag{2.38}$$

where H is the *scale height* of the atmosphere at the perigee, and I_k denotes the modified Bessel function of order k and argument (ae/H) where a is the semi-major axis. The parameter β^* which equals $m/C_D A_P$ is commonly known as the *ballistic coefficient* where C_D is the drag coefficient (≈2.2). When the orbit is circular, equation (2.38) reduces to

$$\frac{da}{dt} \approx \frac{-2\pi\sqrt{\mu a}\rho_{air}}{\beta^*}$$
$$\frac{de}{dt} \approx 0 \tag{2.39}$$

On the other hand, Cosmo and Lorenzini [6] present an empirical model to predict the lifetime of satellites when the atmospheric density is larger than 10^{-14} kg/m^3:

$$R^* = a(1-e) + \frac{2ae}{2+0.308ae/H}$$
$$lifetime = \frac{0.15m^2yr}{kg}\beta^* \frac{[1+2.9(R^*-6578)/T_\infty]^{11}}{3000-T_\infty} \tag{2.40}$$

where T_∞ the exospheric temperature (given in K), is a function of the solar activity [36].

2.5.2 Solar Radiation Pressure

The Sun emits more than 3.8×10^{26} Joules of energy every second [65]. Most of that energy is radiated away from the Sun by photons travelling at the speed of light. The impact of these photons on the surface of a spacecraft disturbs its motion. The solar radiation pressure at any point in the solar system is given by

$$S = \frac{\Xi}{c \cdot 4\pi R_{\alpha-0}^2} \tag{2.41}$$

where Ξ is the total power of the Sun, c is the speed of light, and $R_{\alpha\text{-}0}$ is the distance between the Sun and the object of interest. The solar radiation pressure S in LEO hovers around $4.5\text{x}10^{-6}$ Pa and varies slightly due to several factors like the position of the spacecraft around the Earth and the distance between the Earth and the Sun. The present model takes these minute variations into account. However, one must bear in mind that solar radiation pressure influences the dynamics of a spacecraft only if the object is exposed to sunlight. If the object is in the shadow of the Earth, then the solar radiation pressure force is reduced and may vanish. The present formulation accounts for this variation. Remembering that photons can be treated as particles, the photon-satellite interaction can be seen as a multitude of particles colliding against the surface of an object and bouncing off in various directions [35]. Therefore, the solar radiation pressure force can be accounted for in a way similar to atmospheric lift and drag (Section 2.5.1):

$$F_{Sun} = \psi S[(\sigma_a + \sigma_{rd})\mathring{A}_p s + \frac{2}{3}\sigma_{rd}\mathring{A}_p + 2\sigma_{rs}\mathring{A}_{pp}] \tag{2.42}$$

where ψ is the "shining factor." This parameter is zero if the Sun is hidden from the spacecraft by the Earth, 1 if the Sun is totally visible from the spacecraft, and $0<\psi<1$ if the Sun is partially eclipsed by the Earth. The present formulation utilizes Baker's algorithm to determine the value of ψ [39]. The position of the Sun is determined by an algorithm used in the Astronomical Almanac [66]. The shape factors have a form very similar to those for atmospheric lift and drag, except that the vector $\boldsymbol{v}_r$ is replaced by **s**, a unit vector in the direction of the photon flux. The shape factors for the tether and the square prisms are given by equation (2.43), where $\boldsymbol{n}$ is a unit vector that lies in the ***t-s*** plane and is perpendicular to the tether (Fig. 2.6).

Solar radiation pressure causes yearly sinusoidal variations in eccentricity [33]. The period and magnitude of these variations depend on several factors such as spacecraft area, reflectivity, etc. Figure 2.11 compares the solar pressure force to air drag for a perfectly absorptive 1m^2 flat plate facing an incoming flow of photons and air molecules. Although

Baker states that solar pressure becomes stronger than air drag at 800 km of altitude, the graph below clearly shows that this parameter is strongly dependent on the level of solar activity.

$$
\begin{aligned}
&A_{p_t}^{\circ}=2r(s\cdot n)dx\\
&A_{p_t}^{\circ}=\frac{\pi}{2}r(s\cdot n)ndx\\
&A_{pp_t}^{\circ}=\frac{4}{3}r(s\cdot n)^2ndx\\
&A_{p_{sp}}^{\circ}=\frac{4}{\pi}ac(s\cdot n)+a^2|(s\cdot t)|\\
&A_{p_{sp}}^{\circ}=ac(s\cdot n)n+a^2(s\cdot t)t\\
&A_{pp_{sp}}^{\circ}=\frac{8ac}{3\pi}(s\cdot n)^2n+a^2(s\cdot t)^2t
\end{aligned}
\tag{2.43}
$$

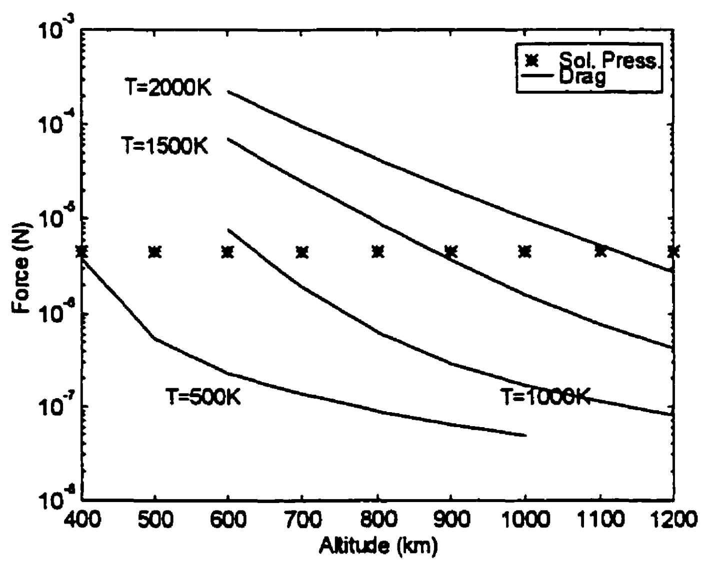

Fig. 2.11: Solar Pressure and Air Drag Forces on a 1m^2 Flat Plate

2.5.3 Earth Asphericity Perturbation Forces

For short term orbital predictions, the gravitational field of the Earth is usually modelled as that of a perfectly spherical and homogeneous body [38], i.e.,

$$\Phi_{sph} = \frac{\mu}{R} \tag{2.44}$$

where Φ_{sph} denotes the gravitational potential of a body with respect to its spherical attractor. As a matter of fact, Φ_{sph} is simply the negative of the gravitational potential energy of the object. This model leads to Keplerian motion in which the object moves along a conic section of fixed dimensions and orientation. As the Earth is not a perfect sphere with uniform mass distribution, this model does not provide accurate results over more than a few hours. For long term predictions, one must account for the exact shape and mass distribution of the Earth. The gravitational potential of an object in orbit around an aspherical and non-homogeneous attractor can be expanded in terms of Legendre functions [67]:

$$\Phi_{true} = \frac{\mu}{R}[1 + \sum_{k=2}^{\infty} \frac{R_{\oplus}^{k}}{R^{k}}[-J_k P_k(\sin\phi) + \sum_{j=1}^{k} P_k^j(\sin\phi)(C_k^j \cos(j\lambda_g) + S_k^j \sin(j\lambda_g))]] \tag{2.45}$$

where $R_{\oplus}$ is the equatorial radius of the Earth, ϕ is the latitude, λ_g is the eastward longitude from Greenwich, $P_k(x)$ is the Legendre polynomial of degree k and order zero, $P_k^j(x)$ is the associated Legendre function of the first kind of degree k and order j, and J_k, C_k and S_k are constants that depend on the shape and mass distribution of the attractor. The value of these coefficients for the Earth are available in the WGS 84 model [68]. The only coefficients retained for calculations in this thesis are J_2 (1082,63X10^{-6}), J_3 (-2.53X10^{-6}), J_4 (-1.61X10^{-6}), C_2^2 (1.57X10^{-6}) and C_3^1 (2.19X10^{-6}); however, the formulation is general.

The perturbative acceleration due to the asphericity and non-homogeneity of the Earth can be obtained by taking the gradient of [Φ_{true} - Φ_{sph}]. Moyer [67] presents this perturbative acceleration in spherical coordinates:

$$
\begin{aligned}
f_{a_R} &= \frac{\mu}{R^2}\sum_{k=2}^{\infty}(k+1)\frac{R_\oplus^k}{R^k}[J_k P_k(\sin\phi) - \sum_{j=1}^{k} P_k^j(\sin\phi)[C_k^j\cos(j\lambda_g) + S_k^j\sin(j\lambda_g)]] \\
f_{a_\lambda} &= \frac{\mu\sec\phi}{R^2}\sum_{k=2}^{\infty}\frac{R_\oplus^k}{R^k}\sum_{j=1}^{k} jP_k^j(\sin\phi)[-C_k^j\sin(j\lambda_g) + S_k^j\cos(j\lambda_g)] \\
f_{a_\phi} &= \frac{\mu\cos\phi}{R^2}\sum_{k=2}^{\infty}\frac{R_\oplus^k}{R^k}[-J_k P_k^{\prime}(\sin\phi) + \sum_{j=1}^{k} P_k^{\prime j}(\sin\phi)[C_k^j\cos(j\lambda_g) + S_k^j\sin(j\lambda_g)]]
\end{aligned}
\tag{2.46}
$$

where the prime above P denotes differentiation with respect to the argument $\sin\phi$. The components of this acceleration vector can be converted to orbital coordinates using equation (2.2).

As J_2 is more than 400 times larger than all the other coefficients of the Legendre harmonics, the J_2 term in f_a is dominant over all of the other terms of equation (2.46). Chobotov [33] states that if only the J_2 term is considered, all orbital parameters show periodic oscillations. However, the mean motion n, the line of apses, and the line of the nodes show the secular variations described by equation (2.47):

$$
\begin{aligned}
\frac{\bar{n}}{n} &= 1 + \frac{3J_2R_\oplus^2}{2a^2(1-e^2)^{3/2}}[1 - \frac{3}{2}\sin^2(i)] \\
\dot{\omega} &= \frac{3J_2R_\oplus^2\bar{n}}{2[a(1-e^2)]^2}[2 - \frac{5}{2}\sin^2(i)] \\
\dot{\Omega} &= \frac{-3J_2R_\oplus^2\bar{n}\cos(i)}{2[a(1-e^2)]^2}
\end{aligned}
\tag{2.47}
$$

2.5.4 Electromagnetic Forces on Conductive Tethered Systems

2.5.4.1 Magnetic Field of the Earth

The motion of a conductive wire across the magnetic field of the Earth induces an EMF and a *Lorentz force* across the system [6]. The resulting voltage and force can provide electrical power and control the motion of the spacecraft. But to accurately predict the effect of *EP* (Electromagnetic Propulsion) on a tethered spacecraft, one must first model the magnetic field of the Earth. As is the case for the gravitational field of the Earth, its magnetic field can be represented by a potential function in terms of Legendre polynomials [69]. This potential function is given by

$$\Phi_{mag} = R_{\oplus} \sum_{k=1}^{\infty} \sum_{j=0}^{k} \frac{R_{\oplus}^{k+1}}{R^{k+1}} P_k^j(\sin\phi)[g_k^j \cos(j\lambda_g) + h_k^j \sin(j\lambda_g)] \tag{2.48}$$

where $P_k^j(x)$ is the normalized Legendre function of the first kind of degree k and order j, while g_k^j and h_k^j are normalized coefficients that determine the exact shape of the magnetic potential. As the magnetic field of the Earth varies continuously, the values of these coefficients change by a few nT (nanoTesla) every year. The yearly values of the *g*'s and *h*'s are found in the IGRF model [70]. The magnetic field $\boldsymbol{B}$ of the Earth at any point is obtained by taking the gradient of the magnetic potential ϕ_{mag}:

$$\begin{aligned} B_R &= \sum_{k=1}^{\infty} \frac{R_{\oplus}^{k+2}}{R^{k+2}} \sum_{j=0}^{k} (k+1) P_k^j(\sin\phi)[g_k^j \cos(j\lambda_g) + h_k^j \sin(j\lambda_g)] \\ B_\lambda &= \sec\phi \sum_{k=1}^{\infty} \frac{R_{\oplus}^{k+2}}{R^{k+2}} \sum_{j=0}^{k} j P_k^j(\sin\phi)[-g_k^j \sin(j\lambda_g) + h_k^j \cos(j\lambda_g)] \\ B_\phi &= \sum_{k=1}^{\infty} \frac{R_{\oplus}^{k+2}}{R^{k+2}} \sum_{j=0}^{k} P_k^{\prime j}(\sin\phi)[g_k^j \cos(j\lambda_g) + h_k^j \sin(j\lambda_g)] \end{aligned} \tag{2.49}$$

where the prime denotes differentiation with respect to the argument $\sin\phi$. The components of the field vector can be written in terms of orbital coordinates using equation (2.2). The computer implementation of the model truncates equation (2.49) at $k=j=5$, which gives 20 coefficients in all.

2.5.4.2 Induced EMF, Current, and Lorentz Forces in Insulated Wires

There exist two basic types of conductive tethers: insulated wires and bare wires. This first subsection analyses the characteristics of insulated wire systems. These devices can only exchange electrons with the ionosphere using the subsatellites, since the entire wire is covered with an insulator (Fig. 2.12). As a result, electron collection in insulated systems is limited to fairly low currents due to *Debye-sheath shielding* [25,71]. On the other hand, electron emission can be achieved using a hollow cathode or an electron gun. The electrical circuit formed by the interaction between an insulated tether and the magnetic field of the Earth is shown in Fig. 2.12.

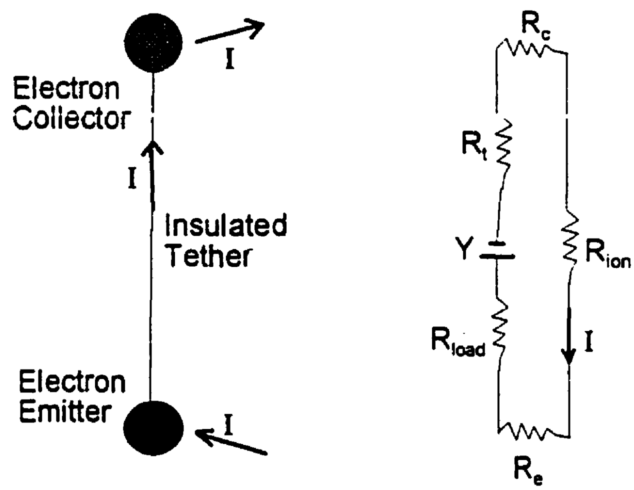

Fig. 2.12: Electrical Circuit for an Insulated Space Tethered System

In the above diagram, R_{load} denotes the impedance of the load, which depends on the application of the system. For example, a negative R_{load} implies that a battery is used to drive the current against the induced EMF Y. R_t, R_e, R_c denote the tether, emitter, and collector resistances, respectively. As in other investigations [24,25,26,71], the present formulation neglects the tether resistance R_t and assumes perfect efficiency. The electrical potential induced in the system by the motion of the conductive tether [6] is given by

$$\Upsilon = \int_0^{l_{tot}} (V_{s/m} \times B) \cdot dl \qquad (2.50)$$

where $V_{s/m}$ designates the velocity of the spacecraft relative to the magnetic field, and dl is an infinitesimal vector element pointing along the tether from m_1 to m_2 (Fig. 2.13). Using this convention, Y is positive whenever m_2 has a higher electrical potential than m_1 and the current I is positive whenever electrons flow from m_2 to m_1.

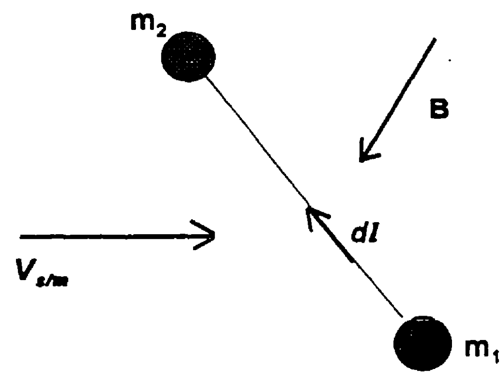

Fig. 2.13: Induced EMF in a Conductive Tether

The velocity of the spacecraft with respect to the magnetic field is given by

$$V_{s/m} = V_s - \omega_\oplus \times R \tag{2.51}$$

where $\omega_\oplus$ is the rotational rate of the Earth and V_s is the spacecraft velocity.

The short-circuit current I_{max}, which corresponds to R_{load}=0, is given by the Parker-Murphy law [72] which was recently updated following the TSS-1R mission [73]:

$$I_{\max} \approx K_1 n_e \sqrt{T_\infty}\left[\frac{1}{2} + \left(\frac{\Upsilon}{\Upsilon_o}\right)^{.528}\right] \tag{2.52}$$

where K_1=5.1255x10^{-15} Amp*m^3/°K$^{.5}$, and n_e denotes the ionospheric electron density. This parameter varies between 10^{12} e$^-$/m^3 (during the day) and 10^{10} e$^-$/m^3 (at night). T_∞ is the undisturbed ionospheric plasma temperature and Y_0 is given by

$$\Upsilon_o = \frac{A^* B^2 e^-}{8\pi m_e} \tag{2.53}$$

where A^* designates the total surface area of the collecting body, B is the magnitude of the surrounding magnetic field, e^- represents the elementary electron charge, and m_e is the electron mass. The current flow through the tether induces a Lorentz force on the system [6] which is given by

$$F_{mag}=\int_0^{l_{tot}} I(dl\times B) \tag{2.54}$$

For insulated wire tethers, the current I can be factored out of the above integral because it remains uniform across the system.

2.5.4.3 Induced EMF, Current, and Lorentz Forces in Insulated Wires

Bare wire systems rely on the tether itself for electron collection (Fig. 2.14). However, a bare wire cannot effectively release electrons into the ionosphere [26,74]. For this reason, such systems are always equipped with one subsatellite acting as an electron emitter and another end mass which merely serves as a ballast to keep the tether taut. Unlike insulated tethers, the characteristic radius of bare wire systems, i.e. the tether radius, is much smaller than the *Debye gyroradius*. This virtually eliminates *Debye shielding* which severely limits the electron collection capability of insulated systems. As a result, bare tethers can collect ions in much larger numbers than insulated wire systems [25].

For example, Figure 2.15 shows the *voltage bias* and the tether current along a bare wire system designed for the generation of 3.1 kW through a load resistance of 200 Ohms using a 20 km long tether with a 1 mm radius flying through a motional electric field E_o=.2 V/m and an electron density n_e of 9×10^{11} e^-/m^3. The *voltage bias* V^* is defined as the difference between the motional EMF generated at a distance l from m_1 and the voltage drop/rise at the load/battery [25]. In other words,

$$V^*(l)=E_o l-I_{\max}*R_{load} \tag{2.55}$$

The collection scenario is the following: the electrons are captured over a segment of the tether (4.52 km in Fig. 2.15). Beyond this point, the current reaches its maximum value I_{max} (15.48 Amp in Fig. 2.15) and does not change thereafter because the voltage bias becomes negative and the wire cannot release electrons.

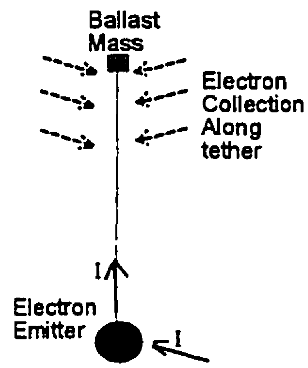

Fig. 2.14: Conceptual Representation of a Bare Wire Tethered System

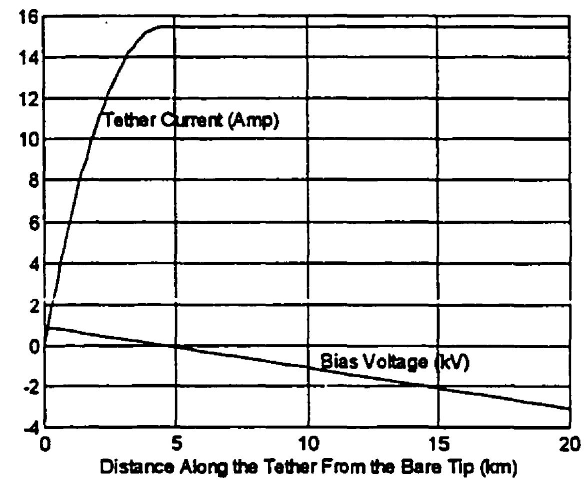

Fig. 2.15: Example of the Current and Voltage Bias Variation Along a Bare Conductive Tether

In mathematical terms, electron collection in bare wires takes place according to the following relations [25,71]. For the interval along the tether where the voltage bias is positive, i.e. form $l=l_{tot}-l_c$ to $l=l_{tot}$, we have

$$\frac{dI(l)}{dl}=K_2 n_e r_t \sqrt{V^*(l)} \tag{2.56}$$

where $V^*(l)$ is given by (2.55) and $K_2=1.9\text{x}10^{-13}\text{C}^{1.5}/\text{kg}^{0.5}$. Upon integration, the above differential equation becomes

$$I(l)=\frac{2}{3}K_2 r_t n_e \sqrt{E_o}[l_c^{3/2}-(l-\frac{I_{max}R_{load}}{E_o})^{3/2}] \tag{2.57}$$

In (2.57) the electron collection length, l_c, is given by

$$l_c=l_{tot}-\frac{I_{max}R_{load}}{E_o} \tag{2.58}$$

For the interval along the tether for which the voltage bias is negative, that is, from $l=0$ to

$l = l_{tot} - l_c$, the tether current is constant:

$$I(l) = I_{max} = \frac{2}{3} K_2 r_t n_e \sqrt{E_o} l_c^{3/2} \qquad (2.59)$$

To verify the validity of (2.57), one can note that it yields zero current when $l = l_{tot}$ and maximum current when $l = l_{tot} - l_c$, which agrees with Figure 2.15. Once the current flowing through each tether element is determined, the induced Lorentz force is calculated using equation (2.54).

2.5.4.4 Effect of Electromagnetic Propulsion on the Orbital Elements

The EP force is responsible for the progressive decay of the spacecraft orbit when the system works as an electrical generator. The TSS-1 missions (Section 1.2.3) and the tethered de-orbit concept (Section 1.3.2) are examples of such generator/deorbit operation. On the other hand, using a battery to run current against the induced EMF produces a thrust which raises the orbit of the satellite. However, this thrust force comes at the expense of the energy expended by the battery. By properly modulating the current in the tether, the electromagnetic force can be used to control the trajectory of tethered systems. Such modulation can be achieved with a variable R_{load} and with a battery that reverses the direction of the current when necessary.

Based on a first order approximation of the magnetic field of the Earth, Moore [75] has determined that EP causes the following effect on the orbital elements of tethered systems:

$$
\begin{aligned}
\Delta a &= \frac{K_3 l_{tot} \cos(i)}{m} \int I(t) dt \\
\Delta e &= \frac{K_3 l_{tot} \cos(i)}{ma} \int I(t) \cos(\theta) dt \\
\Delta i &= \frac{-K_3 l_{tot}}{2ma} \int I(t) \sin(i) \cos^2(u) dt \\
\Delta M &= \frac{3K_3 l_{tot} n \cos(i)}{2ma} \int I(t) t dt \\
\Delta \omega &= \frac{K_3 l_{tot} \cos(i)}{mae} \int I(t) \sin(\theta) dt \\
\Delta \Omega &= \frac{-K_3 l_{tot}}{4ma} \int I(t) \sin(2u) dt
\end{aligned}
\tag{2.60}
$$

where

$$
K_3 \approx \frac{4000kg}{Amp * day} [\frac{R_\oplus}{a}]^{1.5} \tag{2.61}
$$

However, equations (2.60) are not sufficient to determine the variation of the orbital elements; one also needs to know the evolution of the tether current *I(t)*.

Based on a simplified model of the Earth magnetic field [6], the following approximate expressions were obtained for the induced EMF, current, and Lorentz force in orbital coordinates for arbitrary position and pitch, and for zero roll:

$$
\begin{aligned}
\bar{\Upsilon} &\approx K_4 l_{tot} \cos(\alpha) \cos(i) [R_\oplus / R]^{3.5} \\
\bar{I} &\approx \frac{\bar{\Upsilon}}{\bar{R}_{tot}} = \frac{K_4}{\bar{R}_{tot}} l_{tot} \cos(\alpha) \cos(i) [R_\oplus / R]^{3.5} \\
\bar{F}_{x'} &\approx \frac{K_5}{2\bar{R}_{tot}} l_{tot}^2 \sin(2\alpha) \cos^2(i) [R_\oplus / R]^{6.5} \\
\bar{F}_{y'} &\approx \frac{-K_5}{\bar{R}_{tot}} l_{tot}^2 \cos^2(\alpha) \cos^2(i) [R_\oplus / R]^{6.5} \\
\bar{F}_{z'} &\approx \frac{K_5}{2\bar{R}_{tot}} l_{tot}^2 \cos(\alpha) \sin(2i) \cos(u) [R_\oplus / R]^{6.5}
\end{aligned}
\tag{2.62}
$$

where K_3=0.215 V/m, K_4=6.235x10^{-6} N*Ohms/m^2.

Using the above expressions and the perturbation equations for the classical orbital elements [38,76], one can approximate the derivatives of the orbital elements for low eccentricity orbits:

$$\begin{aligned}
\dot{a} &\approx \frac{-2K_5 I_{tot}^2 \cos^2(\alpha)\cos^2(i) R_\oplus^{6.5}}{\sqrt{\mu} m \bar{R}_{tot} a^5} \\
\dot{e} &\approx \frac{3K_5 e I_{tot}^2 \cos^2(\alpha)\cos^2(i) R_\oplus^{6.5}}{2\sqrt{\mu} m |\bar{R}_{tot}| a^6 (1-e^2)^6} \\
\dot{i} &\approx \frac{K_5 I_{tot}^2 \cos(\alpha)\sin(2i) R_\oplus^{6.5}}{4\sqrt{\mu} m \bar{R}_{tot} a^6} \\
\dot{\omega} &\approx \frac{-K_5 I_{tot}^2 \sin(2\alpha)\cos^2(i) R_\oplus^{6.5}}{4\sqrt{\mu} m \bar{R}_{tot} a^6} \\
\dot{\Omega} &\approx 0 \\
\dot{\theta} &\approx n
\end{aligned} \tag{2.63}$$

Despite its being a mere approximation, equation (2.63) reveals a lot about the behaviour of conductive tethered spacecraft. Inverting the above derivatives yields the amount of time required for a prescribed change in each of the orbital elements:

$$\Delta t_a \approx \frac{-\sqrt{\mu} m\bar{R}_{tot}}{12 K_5 l_{tot}^2 \cos^2(\alpha)\cos^2(i) R_\oplus^{6.5}} [a^6]_{a_o}^{a_f}$$

$$\Delta t_e \approx \frac{2\sqrt{\mu} m\bar{R}_{tot} a^6}{3 K_5 l_{tot}^2 \cos^2(\alpha)\cos^2(i) R_\oplus^{6.5}} [\ln e - 3e^2 + \frac{15e^4}{4}]_{e_o}^{e_f}$$

$$\Delta t_i \approx \frac{2\sqrt{\mu} m\bar{R}_{tot} a^6}{K_5 l_{tot}^2 \cos^2(\alpha) R_\oplus^{6.5}} [\ln|\mathrm{cosec}(2i) - cotg(2i)|]_{i_o}^{i_f} \tag{2.64}$$

$$\Delta t_\omega \approx \frac{-4\sqrt{\mu} m\bar{R}_{tot} a^6}{K_5 l_{tot}^2 \sin(2\alpha)\cos^2(i) R_\oplus^{6.5}} [\omega]_{\omega_o}^{\omega_f}$$

$$\Delta t_\theta \approx \frac{1}{n} [\theta]_{\theta_o}^{\theta_f}$$

By comparison, Forward, Hoyt, and Uphoff [8] used a different method which neglected the influence of orbital eccentricity. They obtained the following variations in the semi-major axis and inclination:

$$\frac{\partial a}{\partial t} \approx \frac{-2 l_{tot}^2 B^2 R_\oplus^6 \cos^2(\alpha)\cos^2(i)}{m\bar{R}_{tot} a^5}$$

$$\Delta t_a \approx -[\frac{m\bar{R}_{tot} a^6}{12 l_{tot}^2 B^2 R_\oplus^6 \cos^2(\alpha)\cos^2(i)}]_{a_o}^{a_f} \tag{2.65}$$

$$\frac{\partial i}{\partial t} \approx \frac{l_{tot}^2 B^2 R_\oplus^6 \cos^2(\alpha)\sin(2i)}{4 m\bar{R}_{tot} a^6}$$

Based on the above equations, Forward and Hoyt have calculated the deorbit rate and time for several types of orbits [77,78,79].

2.5.5 Lunisolar Attraction

According to Newton's Universal Law of Gravitation, all objects in the universe attract one another. Nevertheless, light and distant bodies do not significantly attract spacecraft in

LEO. Only the Moon and the Sun can somewhat alter the geocentric trajectory of a spacecraft. Moulton [80] presents the acceleration of any object in LEO due to the attraction of the Sun:

$$f_{☼}=\mu_{☼}[-\frac{R}{R_{s-☼}^{3}}+R_{\oplus-☼}(\frac{1}{R_{s-☼}^{3}}-\frac{1}{R_{\oplus-☼}^{3}})] \tag{2.66}$$

In equation (2.66), ☼ denotes the Sun, ⊕ designates the Earth, and s denotes the spacecraft. A similar relation can also be used to calculate the net attraction of the Moon on the spacecraft. The algorithm required to determine the exact position of the Moon and of the Sun with respect to the Earth at any instant is found in the Astronomical Almanac [66]. Lunar attraction causes the tides on Earth, and a drift in the line of apses and in the line of nodes:

$$\begin{aligned}\frac{d\omega_{☾}}{dt}&=\frac{3n_{☾}^{2}[1-1.5\sin^{2}(i_{☾})][2-2.5\sin^{2}(i)+.5e^{2}]}{4n\sqrt{1-e^{2}}}\\ \frac{d\Omega_{☾}}{dt}&=\frac{-3n_{☾}^{2}(1+1.5e^{2})\cos(i)[3\cos^{2}(i_{☾})-1]}{8n\sqrt{1-e^{2}}}\end{aligned} \tag{2.67}$$

where $n_{☾}$ and $i_{☾}$ denote the mean motion and the inclination of the Moon with respect to the Earth equator, respectively [33]. Equation (2.67) also applies to solar perturbations. For equatorial and circular orbits, the average rotation of the perigee and line of nodes can be approximated by

$$\begin{aligned}\frac{d\bar{\omega}}{dt}&\approx\frac{3n_{☾}^{2}}{2n}\\ \frac{d\bar{\Omega}}{dt}&\approx\frac{-3n_{☾}^{2}}{4n}\end{aligned} \tag{2.68}$$

By comparing equations (2.68) and (2.47), one can deduce that the effect of lunisolar attraction becomes larger than that of Earth oblateness at altitudes beyond 22000 km.

2.6 THERMAL INTERACTIONS BETWEEN THE SYSTEM AND ITS ENVIRONMENT

The temperature of the tether influences the dynamics of the entire system to a certain extent. For example, the SPECTRA-Acrylic tether used in the TiPS mission and in the BOLAS proposal has a high and negative coefficient of thermal expansion. This causes the tether to contract as it heats up. By conservation of angular momentum, the pitch and roll rates are increased. The reverse effect occurs when the spacecraft flies through the shadow of the Earth.

The following analysis assumes that the tether is thermally insulated from the end bodies and that it has uniform temperature. Figure 2.16 shows the heat exchanges between the tether and its surroundings. The cable receives thermal energy from Earth infrared radiation $dQ_{\oplus}/dt$, from direct solar radiation $dQ_{\odot}/dt$, from Earth albedo radiation dQ_A/dt, from air drag dQ_D/dt, and from ohmic dissipation dQ_O/dt. On the other hand, the tether radiates energy away in the infrared spectrum dQ_E/dt.

A simple heat balance on the tether gives the state equation for tether temperature T:

$$\frac{dT}{dt}=\frac{[\dot{Q}_{\oplus}+\dot{Q}_{\odot}+\dot{Q}_A+\dot{Q}_D+\dot{Q}_O-\dot{Q}_E]}{m_t\kappa} \tag{2.69}$$

The Earth infrared radiation absorbed by the tether [6] is given by

$$\dot{Q}_{\oplus}=(2\pi r l_{tot})F^{o}\sigma T_{\oplus}^{4}\epsilon_t \tag{2.70}$$

where F^o is the view factor of the tether for the Earth. This parameter varies with the altitude and with the orientation of the system. σ denotes Stephan-Boltzmann's constant, and $T_{\oplus}$ is the black body temperature of the Earth (248 ^{0}K). The dependence of $dQ_{\oplus}/dt$ on the tether emissivity ϵ_t is justified by Kirchoff's law [81].

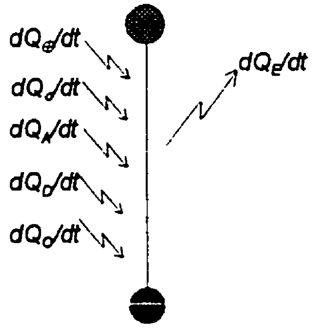

Fig. 2.16: Heat Exchanges between the System and Its Environment

The heating rate due to direct solar radiation is [6]

$$\dot{Q}_{\odot}=\sigma_{a}A_{p_{t}}^{\circ}\psi\Phi_{\odot} \tag{2.71}$$

where Ψ is the shining factor and A_{pt}° is first shape factor of the tether. $\Phi_{\odot}$ is the solar flux:

$$\Phi_{\odot}=Sc=\frac{\Xi}{4\pi R_{s-\odot}^{2}} \tag{2.72}$$

The solar flux in LEO averages 1353 W/m^2. Its minute variations ($\approx$40 W/m^2) result from the change in the distance between the spacecraft and the Sun. The present formulation accounts for these variations. While much of the solar radiation incident on the system comes directly from the Sun, a significant amount bounces off the clouds and the surface of the Earth before hitting the spacecraft [6]. This phenomenon is called Earth albedo radiation and its intensity is given by

$$\dot{Q}_{A}=(2\pi r l_{tot})F^{o}\tau\Phi_{\odot}\sigma_{a}\cos(\varsigma) \tag{2.73}$$

where ς represents the *Sun-zenith angle*; that is, the reflection angle of Sun rays on the Earth or atmosphere. τ denotes the *Earth albedo*: the reflectivity of the Earth. τ ranges between 0.1 and 0.7, but its average value is 0.37.

The atmospheric heating input is simply the power exerted by aerodynamic forces on the tether [6]

$$\dot{Q}_D = F_{air} \cdot V_R \tag{2.74}$$

If an electrical current is run through the tether, the resulting ohmic dissipation will transfer heat to the system at the rate

$$\dot{Q}_U = R_t I^2 \tag{2.75}$$

where R_t is the tether resistance and I is the tether current. Finally, the tether radiates energy away according to Stephan-Boltzmann law [6]

$$\dot{Q}_E = (2\pi r l_{tot}) \epsilon_t \sigma T^4 \tag{2.76}$$

Although the determination of the exact thermal profile requires the integration of equation (2.69), the minimum tether temperature can be approximated by equating the heat intake due to Earth radiation with the energy radiated by the tether:

$$T_{\min} \approx T_{\oplus} F^{o\,1/4}_{\min} \tag{2.77}$$

On the other hand the tether temperature is maximized when the solar, the albedo, and the Earth IR heating are all maximized. Therefore, the maximum tether temperature is approximately

$$T_{\max} \approx \sqrt[4]{F^{o}_{\max} T^4_{\oplus} + \frac{\Phi_a \sigma_a [\tau F^{o}_{\max} \cos(\varsigma) + 1/\pi]}{\epsilon_t \sigma}} \tag{2.78}$$

2.7 EFFECT OF EXTERNAL PERTURBATIONS ON SYSTEM LIBRATIONS

2.7.1 Effect of Atmospheric Forces on System Librations

Atmospheric forces influence the librations of tethered systems in two major ways. Firstly, they can shift the equilibrium angle of the system when the aerodynamic centre of the system does not coincide with the centre of mass, or when the atmospheric density gradient along the tether becomes large. Secondly, atmospheric forces can dampen or excite the librations of a tethered system.

2.7.1.1 Equilibrium Angle Shift due to Aerodynamic Forces

The equilibrium angle shift caused by aerodynamic forces has been investigated on several occasions [43,82], but all solutions found so far are implicit and iterative. The main objective of this subsection is to derive an explicit approximate solution to the problem of equilibrium shift in tethered systems due to atmospheric forces. Three end mass shapes are considered: the sphere, the cylinder, and square prism (Section 2.5.1.2).

As mentioned earlier, the position of the aerodynamic centre along the tether is one of the major factors influencing the equilibrium shift. Using a notation similar to that of Section 2.5.1.2, the aerodynamic centre of a tethered system is given by

$$\delta^{*}=\frac{A_{p_t}^{D}[l_{tot}+c_1]/2+A_{p_2}^{D}[l_{tot}+(c_1+c_2)/2]}{A_{p_1}^{D}+A_{p_2}^{D}+A_{p_t}^{D}} \tag{2.79}$$

where δ^* denotes the distance between the centre of m_1 and the aerodynamic centre of the system. When the aerodynamic centre falls below the mass centre ($\delta^*<\delta$), the equilibrium shift is positive, and vice-versa.

The atmospheric torque on the system can be calculated by substituting equation (2.30) which gives the atmospheric force into equation (2.29a). To simplify the treatment of this problem, the flow reflection is assumed to be perfectly diffuse (σ_n=σ_t=1), roll oscillations are disregarded, the tether is presumed to be cylindrical (2.33), and V_b<<V_r:

$$Q_{air}=\rho_{air}F^{*}V_r^2\cos\alpha[A_{p_1}^{D}\delta-A_{p_2}^{D}(l_{tot}-\delta)-r_t l_{tot}\cos\alpha(l_{tot}-2\delta)] \tag{2.80}$$

The above equation assumes that l_{tot} and δ are much larger than the end masses dimensions, and that the air density and speed remain uniform along the system. On the other hand, the F^* term accounts for the influence of Earth rotation [51]:

$$F^{*}=[1-\frac{\omega_{atm}\cos(i)}{\omega_{orb}}]^2 \tag{2.81}$$

The equilibrium angle shift due to atmospheric forces can be determined by substituting (2.80) into the pitch equation of motion (2.12), and setting all time derivatives to zero:

$$\frac{3\mu\sin2\alpha}{2a^3}=\frac{\rho_{air}F^{*}\mu\cos\alpha[A_{p_1}^{D}\delta-A_{p_2}^{D}(l_{tot}-\delta)-r_t l_{tot}\cos\alpha(l_{tot}-2\delta)]}{m_e a l_{tot}^2} \tag{2.82}$$

The term on the left-hand side of equation (2.82) represents the GG (Gravity Gradient) torque. Furthermore, (2.82) neglects the influence of orbital eccentricity and Earth oblateness.

The "perturbed" equilibrium angle for square prismatic end masses α_{sp}, for spherical subsatellites α_{sph}, and for cylindrical end masses α_{cyl} can be determined by combining equations (2.34), (2.35), and (2.82) and solving for α. After a few algebraic manipulations, the "perturbed" equilibrium angles reduce to

$$\alpha_{sp}=atan[\frac{K_6}{K_7+sign(\delta^*-\delta)K_8}]$$
$$\alpha_{cyl}=atan[\frac{K_9}{K_7+sign(\delta^*-\delta)K_{10}}] \tag{2.83}$$
$$\alpha_{sph}=asin[\frac{-K_{12}-sign(\delta^*-\delta)\cdot\sqrt{K_{12}^2-4K_{11}K_{13}}}{2K_{11}}]$$

where the K's are given by

$$K_6=\frac{4[\delta a_1c_1-(l_{tot}-\delta)a_2c_2]}{\pi}-r_t l_{tot}(l_{tot}-2\delta)$$
$$K_7=\frac{3m_e l_{tot}^2}{\rho_{air}F^*a^2}$$
$$K_8=\delta a_1^2-(l_{tot}-\delta)a_2^2$$
$$K_9=2\delta r_{cyl_1}l_{cyl_1}-2(l_{tot}-\delta)r_{cyl_2}l_{cyl_2}-r_t l_{tot}(l_{tot}-2\delta)$$
$$K_{10}=\pi[\delta r_{cyl_1}^2-(l_{tot}-\delta)r_{cyl_2}^2] \tag{2.84}$$
$$K_{11}=\frac{9m_e^2l_{tot}^4}{\rho_{air}^2F^{*2}a^4}+r_t^2l_{tot}^2(l-2\delta)^2$$
$$K_{12}=\frac{-6m_e l_{tot}^2\pi[\delta r_{sph_1}^2-(l-\delta)r_{sph_2}^2]}{\rho_{air}F^*a^2}$$
$$K_{13}=\pi^2[\delta r_{sph_1}^2-(l-\delta)r_{sph_2}^2]-r_t^2l_{tot}^2(l-2\delta)^2$$

2.7.1.2 Librational Excitations due to Aerodynamic Forces

Atmospheric forces not only shift the equilibrium angle, they can also cause unstable motion in very long tethered systems. As pointed out by Onada and Watanabe [45], and No and Cochran [47], there exists a critical length l^* given by

$$l^*=\frac{EAH}{mn^2R} \tag{2.85}$$

beyond which aerodynamic forces cause unstable pitch motion.

Furthermore, the oblateness of the Earth can also cause unstable roll motion. A spacecraft flying along an inclined orbit encounters a $2\omega_{orb}$ variation in atmospheric density due to the ellipsoidal shape of the Earth. As a result, the aerodynamic forces on the system also follow a $2\omega_{orb}$ variation which is resonant with roll librations [42].

2.7.2 Effect of Earth Oblateness Forces on System Librations

Analysing the influence of Earth oblateness forces on the librational motion of tethered systems can be greatly simplified by considering the J_2 term only. With this in mind, the oblateness perturbation force [38] reduces to

$$
\begin{aligned}
F_x' &= \frac{-3m\mu J_2 R_\oplus^2[1-3\sin^2(i)\sin^2(u)]}{2R^4} \\
F_y' &= \frac{-3m\mu J_2 R_\oplus^2 \sin^2(i)\sin(2u)}{2R^4} \\
F_z' &= \frac{-3m\mu J_2 R_\oplus^2[\sin(2i)\sin(u)]}{2R^4}
\end{aligned}
\tag{2.86}
$$

Substituting (2.86) into (2.29) gives the J_2 induced torques:

$$
\begin{aligned}
Q_{\alpha_{J_2}} &= 3\mu J_2 R_\oplus^2 \sum_{j=1}^{k+2} m_j x_j \frac{[(1-3s^2 i_j s^2 u_j)s\alpha c\gamma - s^2 i_j s(2u_j)c\alpha c\gamma)]}{2R_j^4} \\
Q_{\gamma_{J_2}} &= 3\mu J_2 R_\oplus^2 \sum_{j=1}^{k+2} m_j x_j \frac{[(1-3s^2 i_j s^2 u_j)c\alpha s\gamma + s^2 i_j s(2u_j)s\alpha s\gamma - s(2i_j)su_j c\gamma)]}{2R_j^4}
\end{aligned}
\tag{2.87}
$$

where *sx* and *cx* denote the sine and cosine of *x*, respectively. By inspection, the J_2 induced torques arise from variations in the gravitational field along the system. In fact, if gradient effects were neglected, the entire fraction in (2.87) could be factored out of the summation. Furthermore, the sum of $m_j x_j$ would vanish, since it is none other than the first moment of area about the centre of mass, which is zero by definition. In that case, both torques would clearly vanish.

The gradient nature of the J_2 torque does not come as a surprise, since the GG (Gravity Gradient) torque is also gradient based. But as the influence of J_2 on the gravitational field of the Earth is much smaller than that of μ, one should expect any librational instability that could be generated by J_2 torques to be quickly overtaken by the much stronger GG torques.

Closer examination of equation (2.87) reveals the general behaviour of J_2 induced oscillations in tethered systems librating near the local vertical ($\alpha, \gamma \to 0$)

$$\begin{aligned} Q_{\alpha_{J_2}} &\approx 3\mu J_2 R_\oplus^2 \sum_{j=1}^{k+2} m_j x_j \frac{(1-3s^2 i_j s^2 u_j)\alpha - s^2 i_j s(2u_j)}{2R_j^4} \\ Q_{\gamma_{J_2}} &\approx 3\mu J_2 R_\oplus^2 \sum_{j=1}^{k+2} m_j x_j \frac{\gamma(1-3s^2 i_j s^2 u_j) - s(2i_j) s u_j}{2R_j^4} \end{aligned} \tag{2.88}$$

For non-equatorial and non-polar orbits, the pitch oscillations described by (2.88) would be a superposition or *beat* [83] of two waves of frequency $2\omega_{orb}$ (coming from the $\alpha sin^2(u)$ and $sin(2u)$ terms) and $\sqrt{3}\omega_{orb}$ (coming from the α term) respectively. These two waves add up to a single wave with a time varying amplitude, with an oscillation frequency of $(2+\sqrt{3})\omega_{orb}/2$, and a *beat frequency* of $(2-\sqrt{3})\omega_{orb}$. For roll oscillations, the beat frequency would be $(2-1)\omega_{orb}=\omega_{orb}$, since the $\gamma sin^2(u)$ and γ terms both have a $2\omega_{orb}$ frequency, and the $sin(u)$ term has a frequency of ω_{orb}.

For polar orbits, (2.88) becomes

$$\begin{aligned} Q_{\alpha_{J_2}} &\approx 3\mu J_2 R_\oplus^2 \sum_{j=1}^{k+2} m_j x_j \frac{(1-3s^2 u_j)\alpha - s(2u_j)}{2R_j^4} \\ Q_{\gamma_{J_2}} &\approx 3\mu J_2 R_\oplus^2 \gamma \sum_{j=1}^{k+2} m_j x_j \frac{(1-3s^2 u_j)}{2R_j^4} \end{aligned} \tag{2.89}$$

in which case pitch conserves its $(2-\sqrt{3})\omega_{orb}$ beat, but roll "loses its beat" and becomes a "pure" sine wave with a frequency of $2\omega_{orb}$.

For equatorial orbits, (2.88) reduces to

$$Q_{\alpha_{J_2}} \approx 3\mu J_2 R_\oplus^2 \alpha \sum_{j=1}^{k+2} \frac{m_j x_j}{2R_j^4}$$
$$Q_{\gamma_{J_2}} \approx 3\mu J_2 R_\oplus^2 \gamma \sum_{j=1}^{k+2} \frac{m_j x_j}{2R_j^4} \tag{2.90}$$

The J_2 torques on librating systems flying along equatorial orbits have a destabilizing influence, since they grow linearly with the libration angle. But as mentioned earlier, these moments are counterbalanced by the GG torque which tends to align the system along the local vertical. Since the J_2 moment can be regarded as a small perturbation which constantly opposes the GG torque, the resulting motion is a distorted sine wave with a frequency slightly lower than $\sqrt{3}\omega_{orb}$ for pitch and slightly lower than $2\omega_{orb}$ for roll.

2.7.3 Effect of Electromagnetic Forces on System Librations

Electromagnetic forces can not only modify the orbital elements of a spacecraft, they can also alter its librational motion. Colombo et al. [84] have pointed out that a current modulation of $\sqrt{3}\omega_{orb}$ can be used to control pitch librations. However, modulations of one or two times the orbital frequency can dangerously excite roll librations. This topic is discussed in more detail in Chapter 5.

CHAPTER 3

DETERMINATION OF TETHER MATERIAL PROPERTIES

3.1 SPECIMEN DESCRIPTION

This chapter aims at verifying experimentally the commonly accepted value for the longitudinal stiffness and damping ratio of a SPECTRA-1000 tether braided with acrylic. An approximate value for the torsional stiffness and damping ratio is also desired. The tether specimen considered is identical to that used in the TiPS mission and was graciously provided by Joe Carroll of Tether Applications.

To determine some of the physical properties of this tether, two sets of experiments were carried out at the IRIS laboratory of the University of British Columbia and at the Chapman Space Centre of the Canadian Space Agency.

3.2 TETHER LONGITUDINAL STIFFNESS AND DAMPING PROPERTIES

3.2.1 Preliminary Considerations

The longitudinal stiffness *EA* and damping ratio ζ of the tether not only influence the vibrations of the tether, they also determine to a great extent the decay rate of the librations. This phenomenon is caused by the coupling between pitch, roll and longitudinal strain noticeable from equations (2.12), (2.13), and (2.15). To determine the value of *EA* and ζ, a simple tether and mass system was constructed (Fig. 3.1).

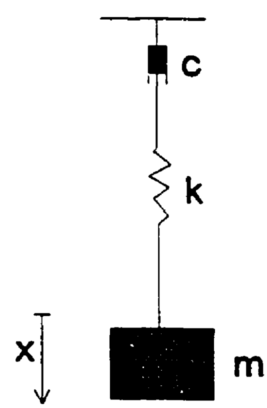

Fig. 3.1: Schematic Representation of the Experimental Setup

SPECTRA is known for its highly non-linear stress-strain relationship [85]. Furthermore, its stiffness and damping properties depend on the tether "loading history"; that is, on the number of loading cycles and the magnitude of each cycle. Neglecting the influence of the tether mass, the equation of motion for the system shown in Figure 3.1 is given by:

$$\ddot{x}+\frac{c}{m}\dot{x}+\frac{k}{m}x=g \tag{3.1}$$

where $k = EA/l$ and $c = 2\zeta m\omega_n$. As a result, the above expression can be written as

$$\ddot{x}+2\zeta\omega_n\dot{x}+\omega_n^2x=g \tag{3.2}$$

3.2.1.1 Static Tests

At static equilibrium, the two time derivatives in equation (3.2) vanish. Therefore, a simple measurement of the deformation caused by a given mass fixes the tether stiffness for a given load:

$$EA=\frac{mgl}{x_{eq}} \tag{3.3}$$

3.2.1.2 Dynamic Tests

The system vibrations hold the key to the determination of the tether stiffness and damping ratio [86]. The frequency of the dampened oscillations ω_d, the period between two consecutive maxima τ_d, and the ratio of the amplitude of two consecutive maxima β are given by:

$$\begin{gathered}\omega_d=\omega_n\sqrt{1-\zeta^2}\\ \tau_d=2\pi/\omega_d\\ \beta=e^{[2\pi\zeta]/\sqrt{1-\zeta^2}}\end{gathered} \tag{3.4}$$

From the above equations, τ_d and β suffice to solve for the damping ratio and the stiffness:

$$\begin{gathered}\zeta=\frac{\ln\beta}{\sqrt{[\ln\beta]^2+4\pi^2}}\\ EA=\frac{4\pi^2ml}{\tau_d^2(1-\zeta^2)}\end{gathered} \tag{3.5}$$

To summarize, the tether stiffness can be obtained using both static and dynamic tests (equations (3.3) and (3.5)), while the damping ratio can only be deduced from dynamic tests (equations (3.5)).

3.2.2 Laboratory Setup

The laboratory setup for static and dynamic tests is described in length by Modi and Pradhan [87] who used the same facilities to perform similar tests on the OEDIPUS-C tether.

3.2.2.1 Static Tests

The laboratory setup for static tests consists of the elements shown on Figure 3.1 (tether and end mass) and of a Vernier caliper used to measure the static deformation of the cable.

3.2.2.1 Dynamic Tests

The oscillations of the mass (m = 0.2 kg) are monitored using an accelerometer (m = 0.031 kg) attached to the end body. A thin wire links the accelerometer to a charge amplifier. The amplifier boosts the weak electrical signal emitted by the transducer and relays it to an oscilloscope. The operator reads the necessary information (τ_d and δ) graphically from the oscilloscope.

3.2.3 Results and Analysis

3.2.3.1 Static Tests

Tables 3.1 and 3.2, and Figure 3.2 present the data related to three distinct static deformation tests. The first test was carried out on a "fresh" tether (with no previous loading). The second test was carried out on the same specimen, but after it had been subjected to test #1 and to a 2 N load for 100 minutes. Finally, the third test was performed following the first two tests and a 2 N pre-stress of 2 months.

Table 3.1: Results of Two Static Deformation Tests				
End mass (g)	Elongation for test #1 (cm)	EA for test #1 (N)	Elongation for test #2 (cm)	EA for test #2 (N)
0	0	-	0	-
5	0.45	44.3	0.3	66.5
10	0.7	57	0.5	79.8
20	1.4	57	1.1	72.5
30	1.55	77.2	1.25	95.7
40	1.75	91.1	1.45	110
50	1.95	102.3	1.6	124.6
60	2.1	113.9	1.8	132.9
70	2.4	116.3	1.9	146.9
100	2.7	147.7	2.3	173.4
150	3.15	189.9	2.6	230.1
200	3.6	221.5	2.7	295.4
300	3.8	314.8	3	398.8
400	4.2	379.8	3.15	506.4
500	4.3	463.7	3.3	604.2

Table 3.2: Results of the Third Static Deformation Test		
End mass (g)	Elongation for test #3 (cm)	EA for test #3 (N)
0	0	-
5	0.12	166
10	0.27	148
20	0.51	156

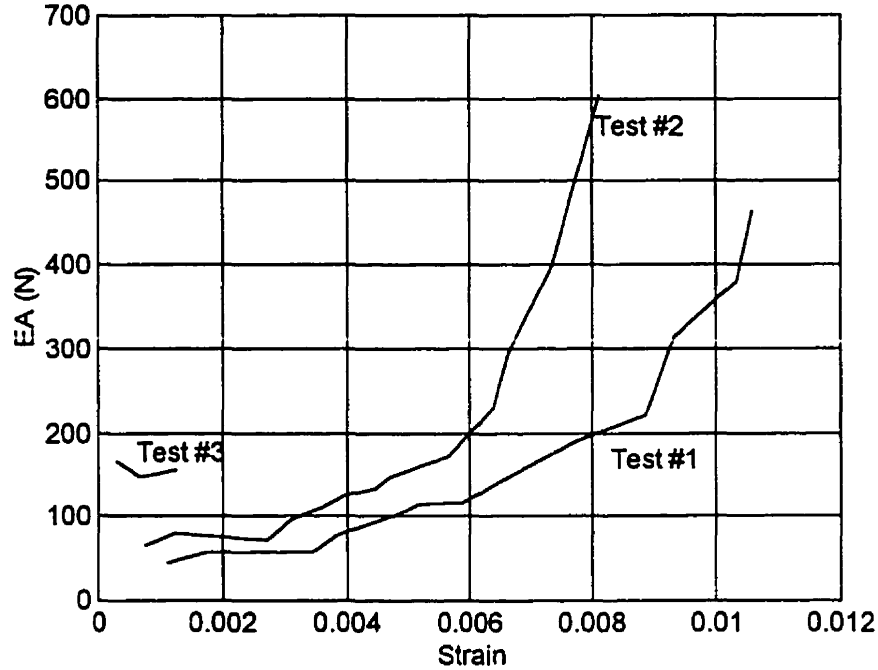

Fig. 3.2: Strain-Stiffness Curve for the Static Deformation Tests

As can be seen from Tables 3.1 and 3.2, and Figure 3.2, the tether stiffness varies with the load and the loading history. By comparison, Figure 3.3 displays the results obtained by the NRL TiPS team [55]. As mentioned in Section 1.8, the dependence of the tether stiffness on the loading history is mainly attributable to tether packing [53]. Indeed, the strength properties of tethers depend to a great extent on the history of the relative motion between the fibres and the layers of the cable. As the tether is stressed and cycled, the friction between the fibres and the layers effectively "packs" the tether. This increases stiffness. The above values of *EA* generally agree with the quoted value of 150 N to 10000 N. The lower stiffness values recorded for low loads are due to the absence of tether packing in "fresh" tethers subjected to low stresses.

Over the long run, SPECTRA, which is used for TiPS and BOLAS, becomes well packed. Furthermore, the tether in these two missions is subjected to very low strains (below 0.003) [88]. The corresponding stiffness in Table 3.3 reaches 150 N. However, the low temperatures prevailing in LEO probably contribute to an increase in *EA*. For this reason, the value of EA adopted for all TiPS and BOLAS simulations in Chapters 4 and 6 is 200 N. This value is consistent with that used in other investigations [52].

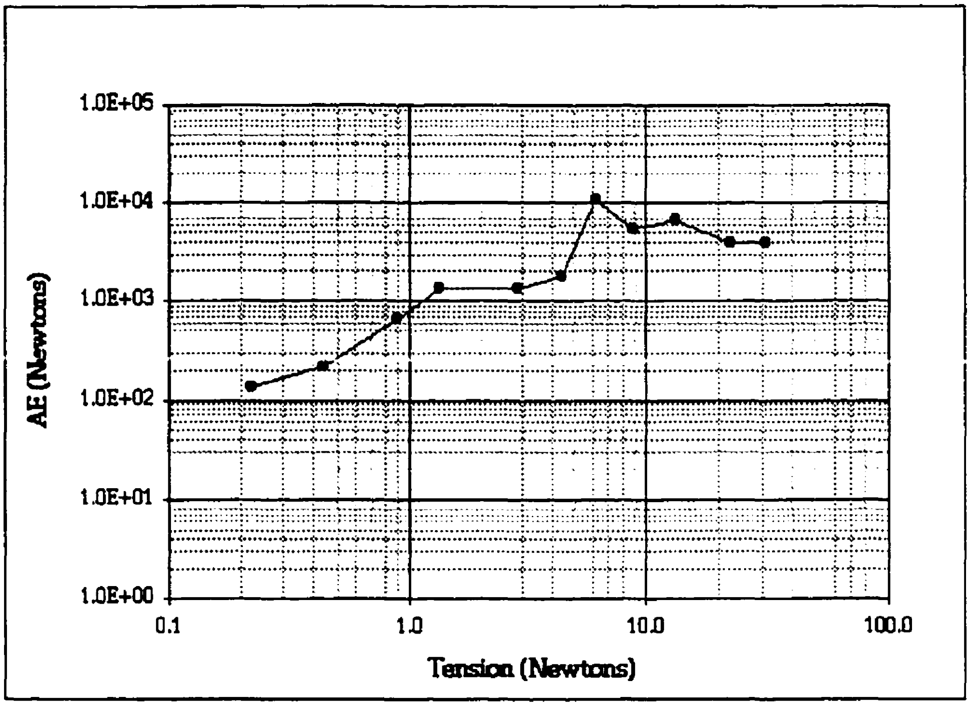

Fig. 3.3: Tension-Stiffness Graph of the TiPS Tether [55]

3.2.3.2 Dynamic Tests

The specimen underwent dynamics tests following a two-month prestressing of 2 N. Several tests were carried out to determine the period of the oscillations T_d and the ratio of two consecutive maxima θ. The data pertaining to these tests are displayed in Table 3.3.

The results yield an average stiffness of 2700 N (σ = 620 N) which is consistent with that of a "well packed" tether subjected to heavy loading. The mean damping ratio is 0.13 (σ = 0.02) which agrees with the value of 0.1 quoted by Schultz and Vigneron [52].

The effect of the uncertainty of the stiffness and damping ratio on the long-term dynamics of space tethered systems is difficult to predict. Glaese found that larger damping ratios decay tether vibrations more quickly, but to a lesser extent than smaller damping ratios [88].

Table 3.3: Dynamics Tests Data				
Trial #	β	τ_d (s)	ζ	EA (N)
1	2.6	0.1625	0.1503	1436
2	1.85	0.1125	0.0971	2957
3	1.8	0.125	0.0931	2393
4	2.5	0.125	0.1443	2423
5	2.4	0.119	0.138	2669
6	2	0.125	0.1097	2401
7	2.63	0.125	0.1518	2429
8	2	0.125	0.1097	2401
9	2.5	0.1125	0.1443	2991
10	2.27	0.13	0.1296	2231
11	2.56	0.125	0.1477	2425
12	3	0.15	0.1722	1698
13	2.4	0.125	0.138	2419
14	2.25	0.1	0.128	3769
15	2.22	0.1125	0.1261	2976
16	2.67	0.1125	0.1542	3000
17	2.43	0.1	0.1398	3781
18	2.1	0.1125	0.1173	2970
19	2	0.1	0.1097	3752
20	2.5	0.1125	0.1443	2991

3.3 TETHER TORSIONAL STIFFNESS AND DAMPING PROPERTIES

3.3.1 Preliminary Considerations

The equation of torque-free torsional motion is derived from the concepts elaborated by Wilson [89]

$$\ddot{\theta}+\frac{D\dot{\theta}}{J}+\frac{IG\theta}{Jl}=0 \tag{3.6}$$

where $J = mr^2/2$ denotes the mass moment of inertia of the load; D represents the torsional damping coefficient [kg*m²/s], $I = \pi r^4/2$ is the polar moment of inertia of the tether [90]; G denotes the shear modulus of the tether [Pa], θ is the twist (angular deflection), and l is the tether length [m]. To determine the value of G and D, one must measure the ratio of the amplitude between an extremum and the following extremum[1] β, and the amount of time elapsed between them $\tau_t/2$.

Comparing equation (3.6) and (3.2) yields the following dynamical equivalence:

$$\omega_n=\sqrt{\frac{IG}{Jl}} \qquad \zeta=\frac{D\sqrt{l}}{2\sqrt{JIG}} \tag{3.7}$$

Therefore, the period of the dampened torsional oscillations is given by

$$\tau_t=2\pi\sqrt{\frac{Jl}{IG(1-\zeta^2)}} \tag{3.8}$$

Once the amplitude ratio β is determined from experiments, the damping coefficient [86] can be calculated using

$$\zeta=\frac{\ln\beta}{\sqrt{[\ln\beta]^2+\pi^2}} \tag{3.9}$$

---

[1] For example, a maximum and the following minimum.

The parameters G and D can then be determined from

$$G=\frac{4\pi^2 J l}{I\tau_t^2(1-\zeta^2)}$$
$$D=\frac{4\pi\zeta J}{\tau_t\sqrt{1-\zeta^2}} \tag{3.10}$$

3.3.2 Laboratory Setup

To calculate the torsional stiffness and damping ratio, a high resolution video camera was used to record the torsional motion of the system. The "movie" of the motion was then analysed to determine D and G. The parameters of the system are shown in Table 3.4.

Table 3.4: System Parameters for Torsional Tests	
End body shape	Cylindrical
End body mass (kg)	0.2
End body radius (cm)	3.5
End body length (cm)	4.4
Tether radius (mm)	1.125
Tether length (m)	4.065
I_{tether} (m^4)	$2.516\text{x}10^{-12}$
J ($kg*m^2$)	$1.225\text{x}10^{-4}$

3.3.3 Results

A series of six tests were carried out to determine the values of D and G. The data related to these experiments are summarized in Table 3.5.

Table 3.5: Torsional Stiffness and Damping Test					
Test #	Ratio between max. and min.	ζ	Time Between Extrema (sec)	D [µkg*m^2/s]	G [MPa]
1	3.33	0.358	26.6	11.1	3.17
2	3.75	0.388	21.9	14.8	4.79
3	3.33	0.358	24	12.3	3.89
4	2.31	0.258	19	10.8	5.8
5	3.2	0.347	31	9.2	2.31
6	2.74	0.306	24.5	10.1	3.59

Table 3.6 presents the average value and standard deviation of the three important torsional properties of the specimen.

Table 3.6: Average Torsional Properties of the Specimen		
Torsional property	Average value	Standard deviation
Shear Modulus G (MPa)	3.92	1.2
Torsional damping coefficient D (µkg*m^2/s)	11.4	2
Torsional damping factor ζ	0.336	0.047

3.3.4 Torsional Period of Orbital Tethered Systems

This sections applies the results obtained in the preceding section to orbital systems. Figure 3.4 illustrates the motion of the end masses about the tether (yaw) axis.

Accounting for the presence of tether damping, the period of the twist motion is

$$\tau_t = 2\pi \sqrt{\frac{J_1 J_2 l}{IG(J_1+J_2)(1-\zeta^2)}} \tag{3.11}$$

Assuming that the torsional stiffness G and dampening ratio ζ do not vary with the tether length, Table 3.7 shows the period of torsional oscillation of two tethered systems equipped with the same type of tether as the one tested in this chapter.

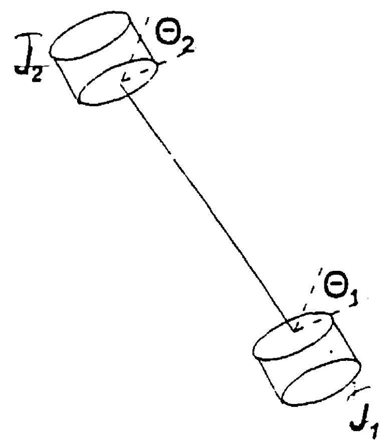

Fig. 3.4: Motion of Spacecraft about the Yaw Axis

Table 3.7: Period of Torsional Oscillation for Two Tethered Spacecraft				
Name	l (m)	J_1 (kg*m^2)	J_2 (kg*m^2)	T_t (hrs)
TiPS	4023	1.387	0.349	19.8
BOLAS	100	1.694	1.661	5.41

To determine the amount of vibrational energy lost over time, one must consider the period and amplitude of oscillation, as well as the damping ratio. As shown in Table 3.7, the period of torsional oscillations for tethered systems is extremely long (hours to days). Furthermore, torsional strains in tethered systems are usually low [91]. As a result, tethered systems lose little energy through torsional damping, even though the damping ratio is relatively large (0.336 for SPECTRA). Hence, the assumption that yaw oscillations have negligible influence on the system is justified.

CHAPTER 4

THE DYNAMICS OF LIBRATING SPACE TETHERED SYSTEMS

4.1 EFFECT OF AERODYNAMIC FORCES ON LIBRATING SYSTEMS

4.1.1 Equilibrium Angle Shift due to Atmospheric Forces

As mentioned in Section (2.7.1.1), aerodynamic forces cause a shift in the equilibrium angle of librating tethered systems. This perturbation results from the torque imparted on the spacecraft by air drag and becomes non-negligible at low altitudes.

The example of a tethered spacecraft flying along a circular and equatorial orbit is used to test the validity of the approximate solution given by equation (2.83) which approximates this angular shift. Three end mass shapes are considered: the square parallelepiped, the cylinder, and the sphere. The parameters of the end bodies and tether are displayed in Tables 4.1 and 4.2, respectively.

Table 4.1: Parameters of the End Bodies	
Parameter	**Value**
Mass (m_1, m_2)	100 kg, 5 kg
Square prism width (a_1, a_2)	1 m, 0.3 m
Square parallelepiped and cylinder length (c_1, c_2, l_1, l_2)	1 m, 0.3 m
Sphere and cylinder radius (r_{s1}, r_{s2}, r_{c1}, r_{c2})	1 m, 0.3 m

Table 4.2: Parameters of the Tether (SPECTRA-1000 + Acrylic)	
Parameter	**Value**
Mass (m_t)	1.36 kg
Radius (r)	1.125 mm
Length (l)	1000 m

The state equations for the ten variables of interest ($a, e, i, \theta, \Omega, \omega, \alpha, \gamma, \epsilon, T$) and for three of their derivatives ($d\alpha/dt$, $d\gamma/dt$, $d\epsilon/dt$) form a system of thirteen first order differential equations to be integrated using MATLAB's implementation [92] of Gear's method [93]. Unlike fixed step size methods like Euler's method and Runge-Kutta's method, Gear's method is a variable order and variable step size predictor-corrector algorithm particularly well suited for "stiff" systems, which contain time constants of different orders of magnitude. Hence, this algorithm provides much more accurate results than fixed step size methods and faster computational speeds than other predictor-corrector schemes such as the Adams-Moulton method [48].

For the example spacecraft presented above, Tables 4.3 through 4.8 show the equilibrium shift due to atmospheric forces as calculated using equation (2.83) and using the simulation software. Note that although (2.83) assumes that $V_b << V_n$ the simulation does not use this simplification. Therefore, (2.83) gives a simple estimate of the equilibrium shift caused by atmospheric forces, but the simulation software provides more accurate results.

Table 4.3: Estimated Equilibrium Angle Shift Due to Atmospheric Forces for Square Parallelepiped End Masses

Altitude \ T_∞	500 K	1000 K	1500 K
250 km	-1.4°	-10.1°	-19.0°
300 km	-0.23°	-3.3°	-8.1°
400 km	-0.0094°	-0.49°	-1.9°
500 km	-0.0014°	-0.091°	-0.56°

Table 4.4: Simulated Equilibrium Angle Shift Due to Atmospheric Forces for Square Parallelepiped End Masses

Altitude \ T_∞	500 K	1000 K	1500 K
250 km	-1.5°	-10.5°	-19.5°
300 km	-0.24°	-3.4°	-8.4°
400 km	-0.0098°	-0.51°	-2.0°
500 km	-0.0014°	-0.095°	-0.58°

Table 4.5: Estimated Equilibrium Angle Shift Due to Atmospheric Forces for Spherical End Masses

Altitude \ T_∞	500 K	1000 K	1500 K
250 km	-1.5°	-10.5°	-19.8°
300 km	-0.24°	-3.5°	-8.6°
400 km	-0.010°	-0.51°	-2.0°
500 km	-0.0015°	-0.096°	-0.59°

Table 4.6: Simulated Equilibrium Angle Shift Due to Atmospheric Forces for Spherical End Masses

Altitude \ T_∞	500 K	1000 K	1500 K
250 km	-1.5°	-11.0°	-20.2°
300 km	-0.25°	-3.6°	-8.9°
400 km	-0.010°	-0.53°	-2.1°
500 km	-0.0015°	-0.10°	-0.62°

Table 4.7: Estimated Equilibrium Angle Shift Due to Atmospheric Forces for Cylindrical End Masses			
Altitude \ T_∞	500 K	1000 K	1500 K
250 km	-1.4°	-10.5°	-19.8°
300 km	-0.23°	-3.4°	-8.4°
400 km	-0.0096°	-0.50°	-2.0°
500 km	-0.0014°	-0.093°	-0.57°

Table 4.8: Simulated Equilibrium Angle Shift Due to Atmospheric Forces for Cylindrical End Masses			
Altitude \ T_∞	500 K	1000 K	1500 K
250 km	-1.5°	-10.9°	-20.4°
300 km	-0.24°	-3.5°	-8.7°
400 km	-0.010°	-0.52°	-2.0°
500 km	-0.0016°	-0.097°	-0.60°

As shown in the above tables, the equilibrium shift due to atmospheric forces varies strongly with altitude and solar activity. Indeed, lower altitudes and higher solar activities cause higher atmospheric densities which induce larger shifts. The "perturbed" equilibrium angle corresponds to the attitude for which the gravity gradient torque counter-balances the drag induced torque.

Upon examination of the above data, (2.83) is shown to provide a very reasonable approximation of the equilibrium orientation, but slightly underestimates it in all cases. This discrepancy arises because equation (2.83) neglects the second term of (2.30). Indeed, the $\boldsymbol{A}_p^D$ of the tether and end bodies all have a component either in the $\boldsymbol{n}$ or in the $\boldsymbol{v}_r$ direction (equations (2.34), (2.35); Fig. 2.6). Furthermore, the aerodynamic centre does not coincide with the mass centre. As a result, the second term in (2.30) tends to further increase the angular perturbation induced by atmospheric forces. Therefore, the angular shift predicted by (2.83) is always smaller than the "actual" value obtained using the simulation software.

Moreover, one should keep in mind that the accuracy of (2.83) is considerably lower for long tethers. For example, a spacecraft with spherical end masses identical to those described in Tables 4.1 and 4.2, but with a 20 km long tether flying 250 km above the ground in a 1500 K atmosphere would librate about an equilibrium angle of -5.45°, whereas equation (2.83) predicts an equilibrium angle of -6.66°. This 22% error is due to the large atmospheric density gradients along the system which are not accounted for in (2.83). As the density is lower along the upper part of the spacecraft, the analytical solution always overestimates the torque on the upper portion of long tethered systems. Hence, (2.83) underestimates the angular shift caused by atmospheric forces when α_{eq} is positive and overevaluates α_{eq} when the shift is negative.

But that is not all, for as shown in Table 4.9, the mass distribution of the system also influences the angular shift. The results listed below apply to a series of spacecraft with spherical end masses identical to those presented in Tables 4.1 and 4.2, except for the mass of the second end body which varies. The spacecraft is assumed to fly some 250 km above the ground and the prevailing solar activity yields an exopheric temperature of 1500 K.

As the mass of the second end body approaches that of the primary (100 kg), the centre of mass of the system moves higher up along the tether. If the centre of mass is below the aerodynamic centre, then the equilibrium angle will be negative. The converse also holds.. The further the mass centre is from the aerodynamic centre, the larger the equilibrium shift is. The reason why the equilibrium angle does not converge to zero as $m_2 \rightarrow m_1$ is that atmospheric density gradients along the tether induce a larger torque on the lower portion of the cable.

Table 4.9: Simulated Equilibrium Angle Shift due to Atmospheric Forces for Spherical End Masses for Various Values of m_2

m_2 (kg)	Equilibrium Angle
5	-20.5°
25	-1.17°
32	0.01°
50	1.54°
100	2.93°

On the other hand, the projected area of the subsatellites does not play a major role in the equilibrium shift because most of the spacecraft surface area is provided by the tether. Although the example presented in Tables 4.1 and 4.2 has a relatively short tether (1 km), the area of the cable "exposed" to the air flow accounts for more than two thirds of the total spacecraft area. For this reason, changing the projected area of the end masses would not significantly alter the equilibrium orientation.

4.1.2 Instabilities Induced by Aerodynamic Forces

As mentioned in Section 2.7.1.2, atmospheric forces may in some cases cause unstable librational and/or longitudinal motion. This subsection gives an example of such unstable behaviour. Table 4.10 shows the initial parameters of the simulation which assumes an exospheric temperature of 1500 K, and accounts for orbital, librational and longitudinal motion.

Table 4.10: Initial Parameters of the Simulation	
Semi-major axis	6963 km
Orbital eccentricity	0.05
Orbital inclination	90°
True anomaly	0°
Argument of perigee	0°
Right ascension of the ascending node	0°
Pitch	40°
Pitch rate	0°/s
Roll	0°
Roll rate	0/s

Table 4.10: Initial Parameters of the Simulation	
Strain	0.0091[1]
Strain Rate	0/s

The resulting librations and longitudinal oscillations are displayed in Figures 4.1 and 4.2, respectively.

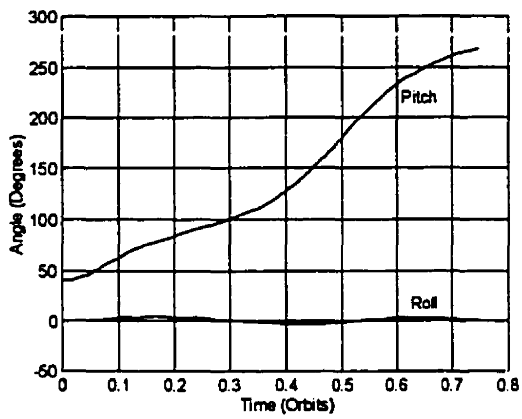

Fig. 4.1: Simulated Attitude for Aerodynamically Unstable Spacecraft

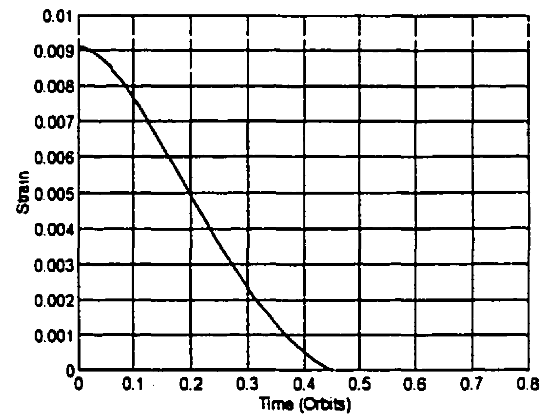

Fig. 4.2: Simulated Strain for Aerodynamically Unstable Spacecraft

As demonstrated by Figures 4.1 and 4.2, the spacecraft motion is clearly unstable: pitch grows in an unbounded fashion; roll oscillations are excited to a 4° amplitude; and the tether loses tension before the spacecraft completes its first half orbit. This unstable motion is caused by a combination of two factors. First and foremost, the aerodynamic centre and the centre of mass of the system are located very far apart. This induces a large net aerodynamic torque on the system. Secondly, the spacecraft encounters large and periodic atmospheric density variations along its eccentric orbit which excite both librational and longitudinal oscillations.

[1] For the prescribed initial orbital and librational parameters, this represents the equilibrium strain (equation (2.15)).

4.2 EFFECT OF EARTH OBLATENESS ON LIBRATING SPACE TETHERED SYSTEMS

This section focuses on the influence of Earth oblateness on the attitude of tethered satellites. The parameters of the spacecraft used to demonstrate the concepts laid out in Section (2.7.2) are presented in Tables 4.1 and 4.2. Unlike what was the case for aerodynamic forces, the shape of the end masses bears no importance on the behaviour of the system. For non-equatorial and non-polar orbits, Earth oblateness torques are given by (2.88) and induce the following librational motion (Figures 4.3 and 4.4):

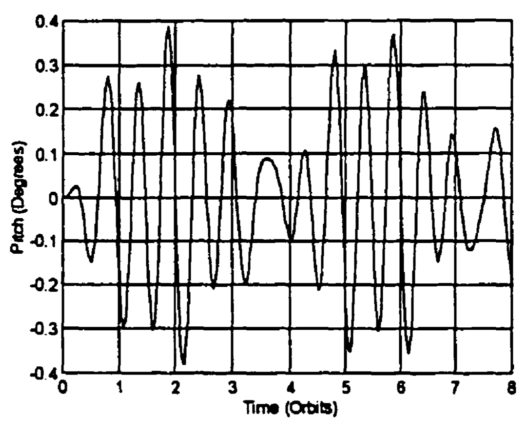

Fig. 4.3: Pitch Librations of a Spacecraft Subjected to Earth Oblateness Torques (a=6578km, e=0, i=45°)

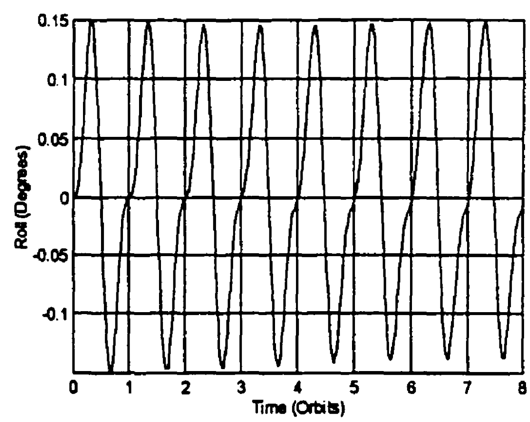

Fig. 4.4: Roll Librations of a Spacecraft Subjected to Earth Oblateness Torques (a=6578km, e=0, i=45°)

The above plots clearly show that pitch follows a beat of frequency $(2-\sqrt{3})\omega_{orb} \approx 0.25\omega_{orb}$ with an oscillation frequency of $(2+\sqrt{3})\omega_{orb}/2 \approx 1.87\omega_{orb}$. On the other hand, roll follows an oscillation of frequency ω_{orb}.

As explained in Section (2.7.2), the same spacecraft flying along a polar orbit should conserve its beat in pitch (Fig. 4.5) and should lose its beat in roll (Fig. 4.6). While Figure 4.5 does follow the expected behaviour, the simulated roll oscillations seem to contradict the theoretical predictions made in Chapter 2. This can be explained by the influence of higher order harmonics of the Earth gravitational field which are not accounted for in equation (2.89), but are included in the simulation software and may have a significant effect in polar orbits. Nevertheless, the roll oscillations due to these harmonics are less than a tenth of the size of that encountered along mid-latitude trajectories (for i=45°).

As shown in Figures 4.7 and 4.8, the pitch and roll motion of equatorial tethered systems subjected to Earth oblateness show no beat, but slightly distorted sinusoidal waves of frequency $\sqrt{3}\omega_{orb}$ and $2\omega_{orb}$ for pitch and roll, respectively. This behaviour agrees with equation (2.90).

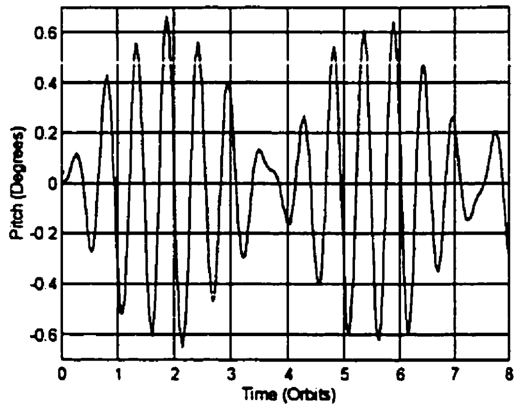

Fig. 4.5: Pitch Librations of a Spacecraft Subjected to Earth Oblateness Torques (a=6578km, e=0, i=90°)

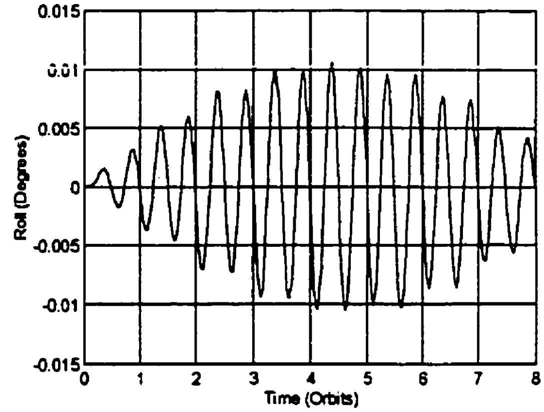

Fig. 4.6: Roll Librations of a Spacecraft Subjected to Earth Oblateness Torques (a=6578km, e=0, i=90°)

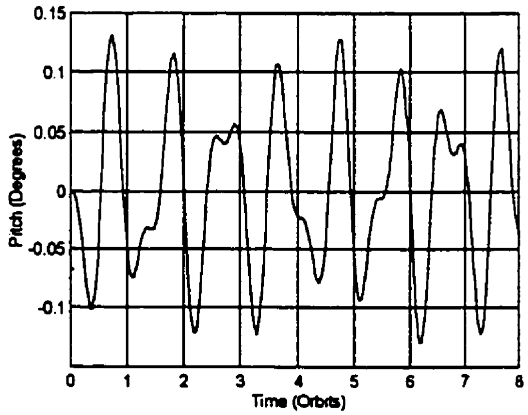

Fig. 4.7: Pitch Librations of a Spacecraft Subjected to Earth Oblateness Torques (a=6578km, e=0, i=0°)

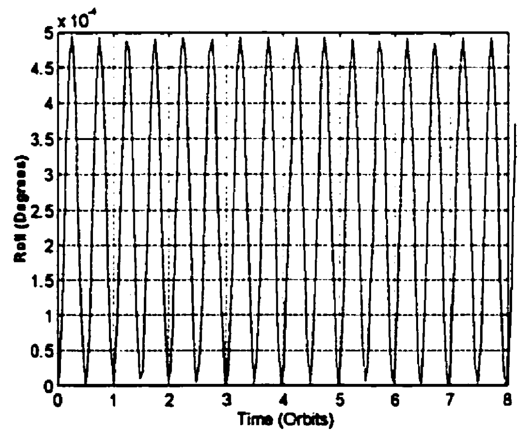

Fig. 4.8: Roll Librations of a Spacecraft Subjected to Earth Oblateness Torques (a=6578km, e=0, i=0°)

A series of parameter analyses was performed to determine the effect of several factors on the oblateness induced oscillations of tethered systems. For example, comparison of Figures 4.5, 4.9 and 4.10 demonstrate the effect of altitude on pitch.

It is clear that the orbital altitude (semi-major axis) only affects the amplitude, but not the shape of pitch librations. A more in depth analysis reveals that the amplitudes of pitch and roll librations vary with the inverse of the square of the altitude.

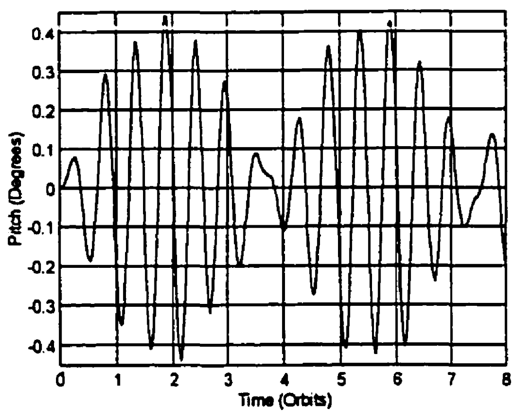

Fig. 4.9: Pitch Librations of a Spacecraft Subjected to Earth Oblateness Torques (a=8000km, e=0, i=0°)

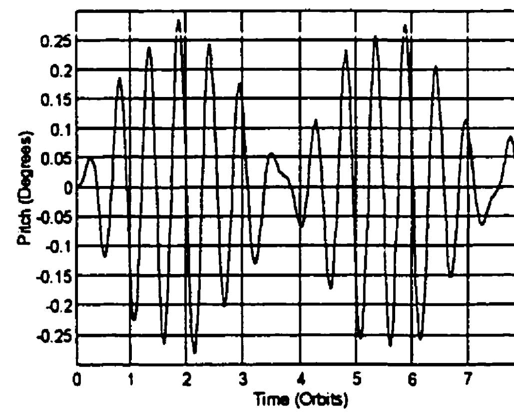

Fig. 4.10: Pitch Librations of a Spacecraft Subjected to Earth Oblateness Torques (a=10000km, e=0, i=90°)

Similar investigations were carried out to determine the influence of system mass and geometry and of orbital inclination on oblateness induced oscillations. Although the results of these analyses are not shown here for brevity, the librations were found to be independent of system geometry and mass over a wide range of values of m_1, m_2, and l. Furthermore, the oblateness induced librations peak at inclinations of 90° for pitch and 45° for roll.

Based on the above results, the following interpolation formulae provide an upper bound on the maximum amplitude of oblateness induced oscillations for tethered systems flying along circular orbits:

$$\alpha_{\max_{J_2}} \leq 0.62^{o}\left(\frac{6578km}{a}\right)^2$$
$$\gamma_{\max_{J_2}} \leq 0.15^{o}\left(\frac{6578km}{a}\right)^2 \qquad (4.1)$$

with equality occurring when i=90° for pitch and when i=45° for roll.

4.3 ANALYSIS OF THE TiPS MISSION

4.3.1 TiPS Spacecraft Parameters

As mentioned in Section 1.2.6, TiPS was launched 3 years ago. The primary objectives of this tethered spacecraft consist of investigating the survivability of tethers and the long-term decay of librations. Tables 4.11 and 4.12 display the parameters of the TiPS subsatellites and tether, respectively.

Table 4.11: Parameters of the TiPS Subsatellites (Ralph/Norton)

Parameter	Value	Source
Mass (m_1, m_2)	37.7 kg, 10.5 kg	[94]
Width (a_1, a_2)	0.67 m, 0.55 m	[10]
Height (c_1,c_2)	0.32 m, 0.23 m	[10]
Solar absorptivity (α_{s1})	0.2	Estimated
Normal accommodation coeff. (σ_{n1}, σ_{n2})	0.85	[35]
Tangential accommodation coeff. (σ_{t1}, σ_{t2})	0.85	[35]

Table 4.12: Parameters of the TiPS Tether (SPECTRA-1000 + Acrylic)

Parameter	Value	Source
Mass (m_t)	5.6 kg	Deduced from other data
Radius (r)	1.125 mm	[10]
Length (l)	4023 m	[10]
Emissivity (ϵ_t)	0.625	[91]
Infrared absorptivity (α_{IR})	0.1	[91]
Solar absorptivity (α_{st})	0.1	[91]
Normal accommodation coeff. (σ_{nt})	0.94	[91]
Tangential accommodation coeff. (σ_{tt})	0.94	[91]
Heat capacity (κ)	1400J/(kg*K)	[91]

Table 4.12: Parameters of the TiPS Tether (SPECTRA-1000 + Acrylic)		
Coeff. of thermal expansion (ξ)	-0.000028/K	[91]
Undisturbed temperature (T_{und})	180 K	Average tether temperature
Damping ratio (ζ)	0.1	[52]

4.3.2 TiPS Predeployment Phase

4.3.2.1 External Forces

For the range of altitudes covered by TiPS, the Earth oblateness force (0.1N) dominates over the solar pressure force (10^{-5}N), lunisolar attraction (10^{-5}N), as well as atmospheric lift and drag (10^{-7}N). As the TiPS tether is not conductive, there are no electromagnetic forces acting on the system. The simulations to follow account for the effect of Earth oblateness, aerodynamic forces, solar pressure and lunisolar attraction. For all simulations to be performed in this section, the tolerance of the Gear integrator is set to $2X10^{-6}$.

4.3.2.2 Orbital Motion Prior to Deployment

Following its May '96 launch, the TiPS spacecraft detached itself from the upper stage and initiated tether deployment on June 20, 1996 at 10:34 GMT. The orbital elements of the satellite are available on the TiPS webpage and are given at intervals of approximately 12 hours [95]. However, the exact position of TiPS at the instant t_0 when the deployment was initiated was unknown. The simplest way to overcome this difficulty is to propagate the trajectory of the system from a time (prior to deployment) when the orbital elements are known, to t_0. Following this procedure, the orbital elements of the spacecraft at t_0 - 3.0667 hours (Table 4.13) were propagated until t_0 (Table 4.14) using the simulation software.

Table 4.13: Initial Conditions of TiPS for Pre-Deployment Simulations		
Parameter	**Value**	**Source**
Beginning of the simulation	June 20, 1996 GMT 7:30	[95]
Semi-major axis (*a*)	7400.653 km	[95]
Eccentricity (*e*)	0.0003317	[95]
True anomaly (θ)	38.673°	[95]
Inclination (*i*)	63.410°	[95]
Argument of perigee (ω)	162.241°	[95]
Long. of the ascending node (Ω)	171.610°	[95]

Table 4.14: Orbital Elements of TiPS at t_0 (Deployment)	
Parameter	**Value**
Semi-major axis (*a*)	7389.626 km
Eccentricity (*e*)	0.00055511
True anomaly (θ)	147.449°
Inclination (*i*)	63.387°
Argument of perigee (ω)	321.232°
Long. of the ascending node (Ω)	171.251°

4.3.3 TiPS Deployment Phase

4.3.3.1 Tether Length History During Deployment

During the 42.5 minutes that deployment lasted, the deployer recorded the amount of tether released using a turn counter. Figure 4.11 shows the variation of the tether length and deployment rate during the manoeuvre[1]. The deployment acceleration was obtained by differentiating the deployment rate point by point and filtering the resulting acceleration profile through a low pass filter. The overall length history (length, length rate, length acceleration) is then used to integrate the equations of motion of the system during deployment (Chapter 2).

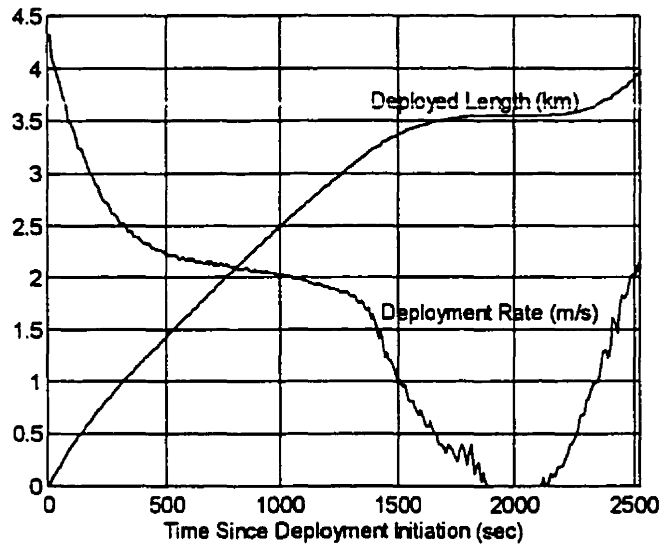

Fig. 4.11: Tether Deployment Length and Length Rate History

4.3.3.2 Parametric Study of Deployment

The exact orientation of TiPS when deployment was initiated remains unknown. However, it is believed that the initial pitch ranged between 10^0 and 50^0, while the initial roll could have been anywhere between -30^0 and 30^0 [96]. Furthermore, the post-deployment pitch and roll amplitudes were thought to be approximately 40° and 25° respectively [10]. However, these values are subject to uncertainties of 7° in pitch and 15° in roll [97]!

In an effort to determine attitude of the system prior to and following deployment, several simulations with different initial orientations were run. In all cases, the initial strain and strain rate were set to 0 and the initial temperature and the damping constant were set

[1] This information was graciously provided by Jim Barnds of the NRL.

to 180 K and 322 kNs, respectively. Table 4.15 shows the post-deployment pitch and roll amplitudes for several possible pre-deployment orientations (α_o, γ_o).

Table 4.15: TiPS Deployment Simulations

α_o	γ_o	α_{amp}	γ_{amp}
10°	-50°	50.0°	18.5°
10°	-30°	39.9°	10.6°
10°	-10°	36.9°	3.4°
10°	10°	36.9°	3.4°
10°	30°	39.9°	10.6°
10°	50°	50.0°	18.4°
20°	-20°	35.6°	7.0°
30°	-50°	41.7°	19.9°
30°	-30°	36.0°	11.0°
30°	-10°	34.5°	3.5°
30°	10°	34.5°	3.5°
30°	30°	36.0°	11.0°
30°	50°	41.7°	19.9°
50°	-50°	40.5°	21.7°
50°	-30°	37.3°	12.2°
50°	-10°	36.9°	3.9°
50°	10°	36.9°	3.9°
50°	18°	36.9°	7.0°
50°	30°	37.3°	12.1°
50°	50°	40.6°	21.7°
50°	60°	46.3°	26.7°
50°	70°	60.0°	30.7°
70°	70°	60.8°	33.6°

These results are consistent with the findings of Glaese who also modelled the effects of transverse tether dynamics, but did not account for the effects of external forces as accurately as the present formulation does [88]. To further demonstrate the agreement among the results, Figures 4.12 and 4.13 show the evolution of the pitch and roll angles during deployment as simulated by the author and by Glaese ($[\alpha_o, \gamma_o] = [20°, -20°]$).

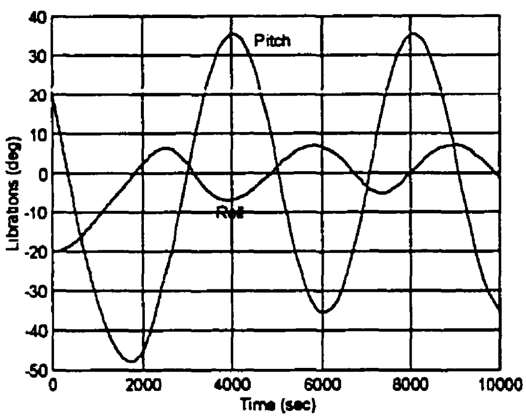

Fig. 4.12: TiPS Deployment Librations Simulated by the Author ($[\alpha_o, \gamma_o] = [20°, -20°]$)

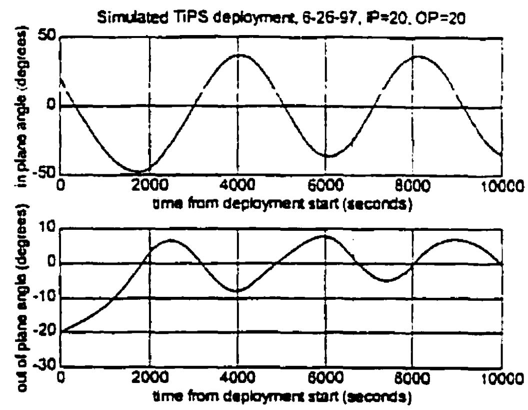

Fig. 4.13: TiPS Deployment Librations Simulated by Glaese ($[\alpha_o, \gamma_o] = [20°, -20°]$) [90]

Examination of Table 4.15 reveals that the post-deployment pitch and roll amplitudes are more strongly dependent on the initial roll than they are on the initial pitch angle. Furthermore, pitch amplitudes of 40° (+/-7°) and roll amplitudes of 25° (+/-15°) are reachable given the range of "probable" initial orientations ($10° < \alpha_o < 50°$; $-30° < \gamma_o < 30°$). For example, an initial pitch and roll of 50° and -30°, respectively generate post-deployment librations of 37.3° in pitch and 12.2° in roll. However, larger roll amplitudes cannot be reached if $10° < \alpha_o < 50°$ and if $-30° < \gamma_o < 30°$. In fact, the highest roll amplitude that can be obtained within that range is 12.2°.

These findings are consistent with those of the NRL [98] and the roll amplitudes recorded using SLR techniques are likely to be erroneous. In fact, the TiPS team no longer believes that the roll amplitude ever went beyond 7°! To tackle the total absence of certainty on the initial roll amplitude of TiPS, it was decided to assume initial pitch and roll amplitudes of 41° and 22°, respectively. This represents a compromise between the roll amplitude of 30°

suggested earlier by TiPS analysts, and the maximum roll amplitude of 12.2° obtained from the deployment simulations for "probable" initial spacecraft attitudes ($10°<\alpha_0<50°$; $-30°<\gamma_0<30°$). With this presumption in mind, Figure 4.14 shows the librations of the system in the early hours of the flight.

4.3.3.3 Tether Tension During Deployment

Figure 4.15 shows the evolution of the tether tension during deployment. The end of the deployment phase is indicated by an "●".

After deployment begins, the tension rises progressively from 0 N to approximately 0.05 N at the end of deployment. This quasi-linear increase of the tension is due to an increase in GG forces as the tether length increases. At the moment when deployment ends, the tether "jerks" and the tension reaches a maximum of about 0.14 N. After the initial "jerk", the tension cycles between 0.075 N to 0.15 N.

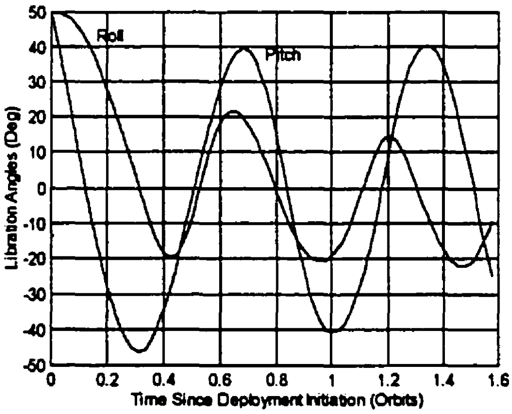

Fig. 4.14: Simulated TiPS Deployment Librations

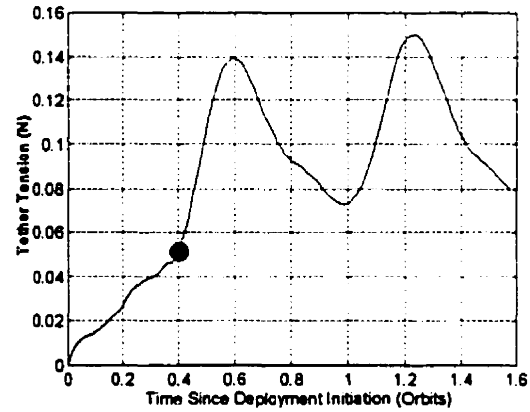

Fig. 4.15: Simulated TiPS Tether Tension during Deployment

4.3.4 TIPS Station-Keeping Phase

4.3.4.1 Orbital Motion

The orbital elements of TiPS show both periodic and secular variations. As an example of periodic motion, Figure 4.16 shows the evolution of the simulated semi-major axis over the second half of the 250th day of flight.

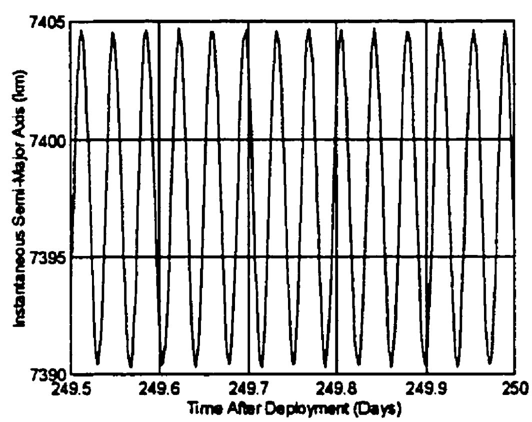

Fig. 4.16: Evolution of the Simulated Semi-major Axis of TiPS

As shown in Figure 4.16, the semi-major axis undergoes periodic variations whose peak to peak amplitude reaches 14.28 km. The period of these oscillations is 52.8 minutes and corresponds to approximately half of the orbital period (105.6 minutes). In other words, the semi-major axis oscillates twice per orbit. This periodic variation is caused by the J_2 term of the Earth oblateness force. Furthermore, this oscillation causes a change in the mean motion n of the satellite. A sinusoidal fit on the above data reveals that the exact mean motion of the satellite is 13.641 rev/day, as opposed to 13.645 rev/day for Keplerian motion. This discrepancy is consistent with equation (2.47). Neglecting this seemingly insignificant discrepancy would cause an error of 360° after 250 days.

Given the large periodic variations undergone by the semi-major axis (a), determining its secular variations requires one to "filter out" the periodic component. One of the possible ways to achieve this consists of calculating the mean value of a over a certain period of time (0.5 days). Figure 4.17 shows the "filtered" secular variation of the semi-major axis of TiPS as predicted by the present formulation. On the other hand, Figure 4.18 shows the same parameter as observed by SLR radars, but using a different filter (devised by NRL analysts). This explains why the initial "filtered" semi-majors axes in Figures 4.17 and 4.18 differ by 2.2 km. Please note that the y-axis units are different in the two figures. However, what really matters is the variation of the filtered or "nominal" semi-major axis during the prescribed period of time. Over the first 250 days of flight, the observed nominal semi-major axis of the orbit decayed by 537 m for an average decay rate of 2.15 m per day (Fig. 4.18). The present model predicts a decay of 533.3 m for an error of only 0.7% (Fig. 4.17). This decay is mainly caused by air drag. As the first term of equation (2.30) dominates over the other two, aerodynamic forces act mainly in the direction opposite to the velocity of the spacecraft. In fact, the lift to drag ratio (L/D) for most satellites is of the order of 1/10 [6]. As a result, atmospheric forces progressively drain mechanical energy from the spacecraft and reduce the semi-major axis of its orbit. The decay rate depends on several factors including the altitude, the solar activity, the spacecraft mass, shape, and surface area.

As expected, the present model outperforms analytical models and empirical interpolation formulae. For example the model presented by Cosmo and Lorenzini [6] and discussed in Section 2.5.1.6 (equation (2.40)) does not apply to TiPS because the atmospheric density is too low. On the other hand, Boden's analytical model (equation (2.38)) predicts a decay of 503.6m which yields an error of 6.2%.

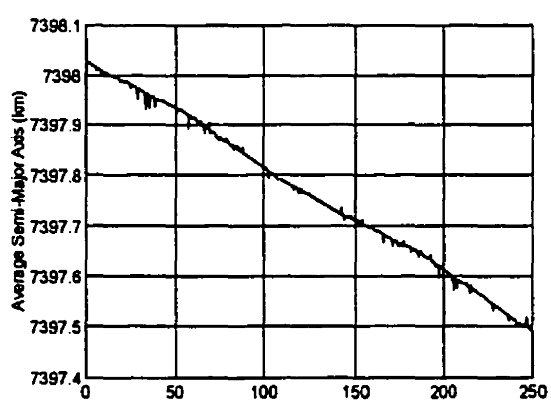

Fig. 4.17: Simulated Secular Variation of TiPS Semi-Major Axis

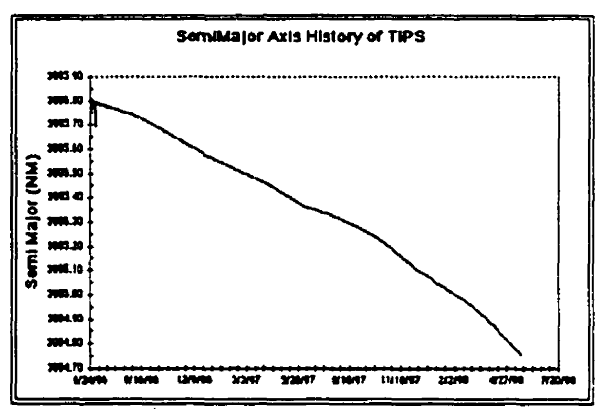

Fig. 4.18: Secular Variation of the TiPS Semi-Major Axis Observed Using SLR Techniques [99]

The orbital eccentricity of TiPS undergoes periodic and secular variations. Figure 4.19 shows the periodic variations of the eccentricity as predicted by the present model. Unlike the semi-major axis, the eccentricity oscillates only once per orbit with a peak-to-peak amplitude of 8×10^{-9}. The graph below clearly shows that the eccentricity also undergoes secular variations. The present formulation predicts an increase of the orbital eccentricity from 0.0002 to 0.0024 over 250 days. This perfectly matches the observed variation of the nominal eccentricity which reaches 0.0024 after 250 days of flight (Fig. 4.20). This increase is caused by solar pressure [33].

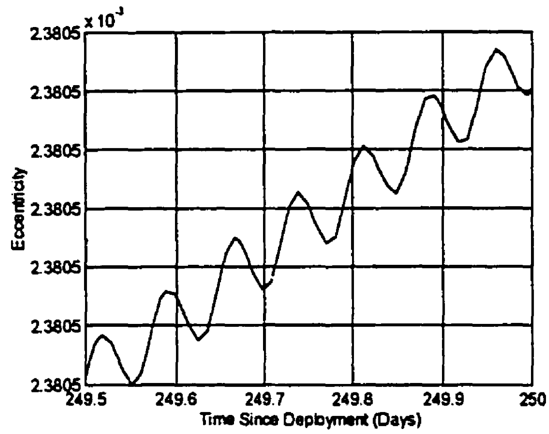

Fig. 4.19: Simulated Variation of the TiPS Eccentricity

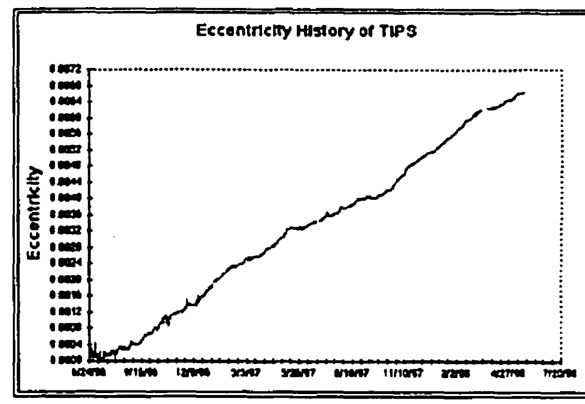

Fig. 4.20: Secular Variation of the TiPS Eccentricity Observed Using SLR Techniques [99]

In contrast, the model predicts very slow periodic oscillations in the inclination (less than 0.03°), but no net secular variations. These results are confirmed by the observed SLR observations, which are very noisy (Fig. 4.21).

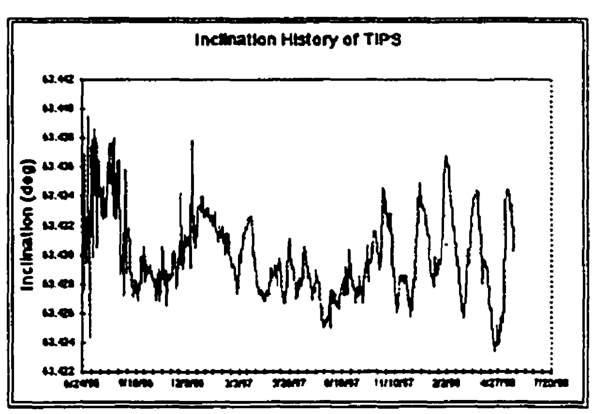

Fig. 4.21: Observed TiPS Inclination [99]

As shown in Figures 4.22 and 4.23, the longitude of the ascending node shows a secular variation of -2.651°/day, yielding a nodal regression of 663° over 250 days. This rotation of the orbital plane is consistent with theory and is caused by the Earth oblateness (equation 2.47). Figure 4.23 was constructed by the author from the record of the orbital elements of TiPS over time [95].

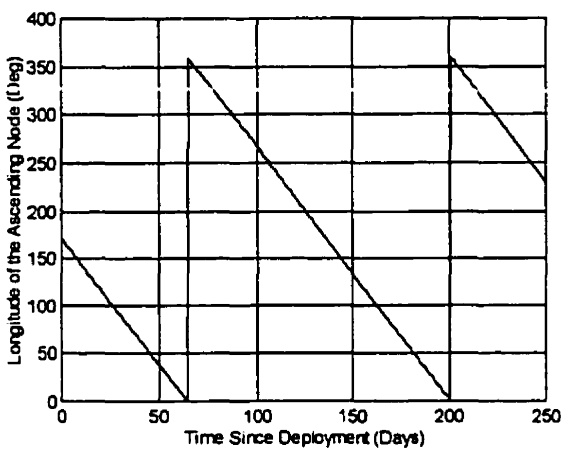

Fig. 4.22: Simulated Evolution of the Longitude of the Ascending Node of TiPS

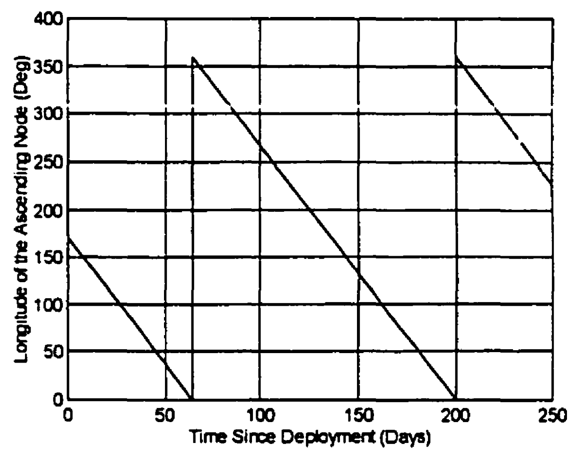

Fig. 4.23: Evolution of the Longitude of the Ascending Node of TiPS Observed Using SLR Techniques [95]

Finally, the argument of perigee is expected to show very little secular changes because the satellite is in a "critical" orbit inclined at 63.4° (equation (2.47)). But as the eccentricity of TiPS is negligible, the argument of perigee loses its meaning, since every point along a circular orbit can be regarded as the apogee or as the perigee. As shown in equation (4.2), this phenomenon corresponds to a singularity of $d\omega/dt$ in the eccentricity [38]

$$\frac{d\omega}{dt}=\frac{R}{he}[-\cos\theta(1+e\cdot\cos\theta)f_{x'}+\sin\theta(2+e\cdot\cos\theta)f_{y'}] \tag{4.2}$$

Equation (4.2) is one the six Lagrange's perturbation equations for the orbital elements. As mentioned in Section 2.2, these equations become singular for circular and equatorial orbits. In the case of TiPS, using Lagrange's formulation indeed causes the failure of integration schemes. This constitutes a strong incentive for propagating the satellite trajectory using the modified version of Broucke's equinoctial elements instead of the Lagrange perturbation equations.

4.3.4.2 Long-Term Librational Motion

As shown in Figure 4.24, roll librations decay quite rapidly over the first 10 days of flight, but they diminish considerably slowly afterward. On the other hand, the pitch amplitude continually decays in an exponential manner. These phenomena result from the coupling between the longitudinal and the attitude dynamics of the system (equations (2.12), (2.13), and (2.15)). Indeed, the librations of the system induce longitudinal oscillations which are damped by tether damping. Hence, the system slowly loses librational energy over time. As the coupling between pitch and strain is stronger than that between roll and strain, pitch decays more appreciably than roll.

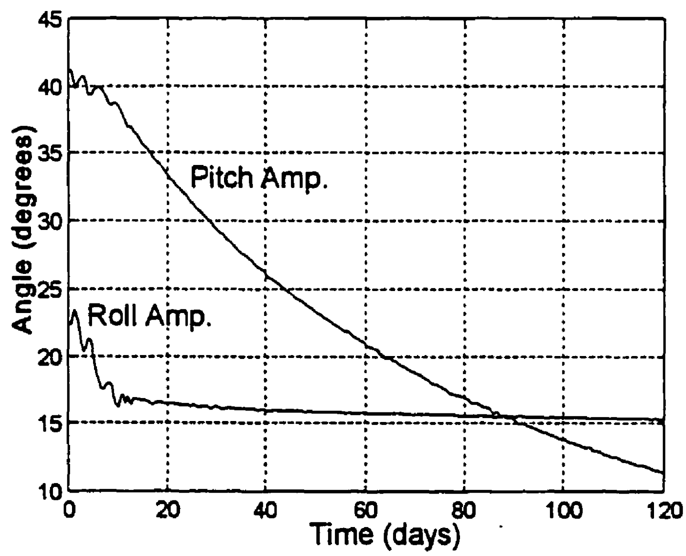

Fig. 4.24: Simulated Decay of TiPS Libration Amplitudes

The rapid decay of roll during the first ten days is related to resonance. When the libration amplitudes are small, the ratio of the frequencies of the two libration motions $\omega_\gamma/\omega_\alpha$ is $2/\sqrt{3}=1.1547$: an irrational number. However, when the libration amplitudes are large, the ratio $\omega_\gamma/\omega_\alpha$ reaches a rational number (5/4). Under such conditions, the system tends to transfer roll librational energy to pitch oscillations. By the principle of least effort, this is the "preferred" path of the system because it loses energy faster in this way. This resonance condition is obvious in Figure 4.25, which plots pitch vs roll oscillations over the first day of flight. Resonance disappears around the tenth day, as demonstrated by Figure 4.26, and hence the rapid decay of roll stops (Fig. 4.24). Glaese obtained similar results [88].

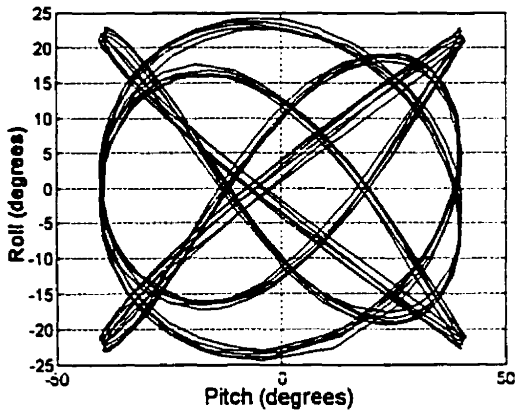

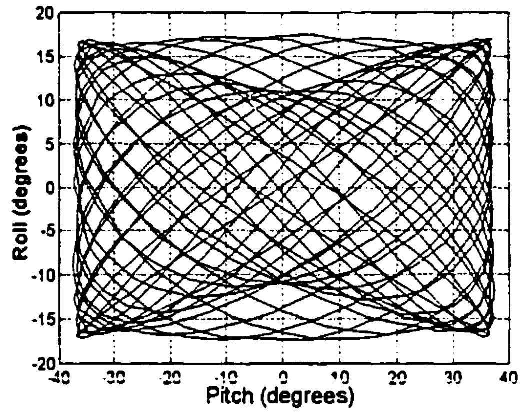

Fig. 4.25: Simulated Pitch and Roll Librations of TiPS During the Tenth Day of Flight

Fig. 4.26: Simulated Pitch and Roll librations of TiPS During the Tenth Day of Flight

Although the trend of the simulated librations is correct (Fig. 4.24), the results do not totally agree with the libration amplitudes observed using the SLR system [88] (Fig. 4.27). In fact, the pitch and roll librations obtained from the SLR data appear to both decay similarly with time. As explained earlier, this discrepancy is more than likely caused by inaccuracies in the roll measurements of SLR's. Indeed, it is believed by the NRL that roll librations may never have exceeded 7° in amplitude [98]. Further simulations reveal that such a scenario is very likely, for a 7° roll amplitude is consistent with the estimated pre-deployment attitude of the system ($10^\circ<\alpha_0<50^\circ$, $-30^\circ<\gamma_0<30^\circ$). In light of these findings, Figure 4.28 shows the decay of the librations for initial amplitudes of 41° and 7° in pitch and roll, respectively. For this simulation, the tether damping constant is 403kNs.

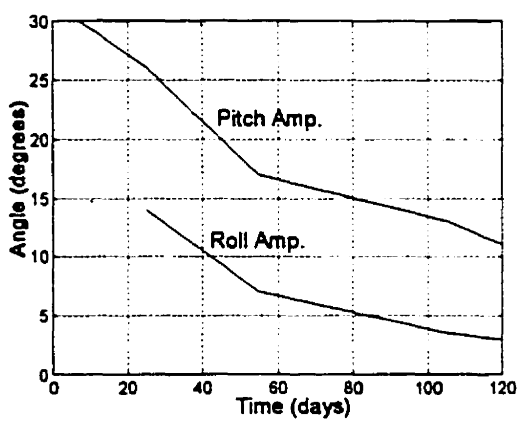

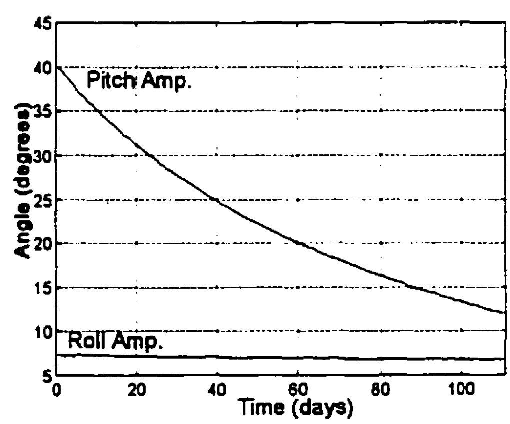

Fig. 4.27: TiPS Libration Amplitudes Observed Using SLR Techniques [88]

Fig. 4.28: Simulated Decay of TiPS Librations for Initial Pitch and Roll Amplitudes of 41° and 7° Respectively

4.3.4.3 Longitudinal Oscillations

Figures 4.15, 4.29 and 4.30 show the longitudinal oscillations of TiPS tether at three different stages of the flight. Figure 4.15 plots the tension during and immediately after deployment and hence shows the transient behaviour of the tether. Figure 4.29 shows the tether vibrations once the transient dynamics have decayed (5 orbits after deployment). Finally, Figure 4.30 displays the tether tension 90 days into the flight.

The most important conclusion to draw from these graphs is that the amplitude of the strain oscillations decays with tether librations (see also Figure 4.24). In fact, the TiPS cable reaches its maximum tension of 0.15N approximately 1.2 orbits into the flight. At this moment, the librations are very large, the transient dynamics of the tether have not yet decayed, and the peak-to-peak amplitude of the tension oscillations reaches 0.08N. By flight day number 90, the maximum tension drops to 0.114N and the peak-to-peak amplitude of tension oscillations is only 0.01N. This large reduction in the amplitude of tension oscillations explains the diminution of librational damping over time. In equation (2.15), the $d\varepsilon/dt$ term dictates the amount of damping. Lower longitudinal oscillation amplitudes imply lower values of $d\varepsilon/dt$ and hence, a lower amount of damping. Therefore, the decay rate of librations decreases with time.

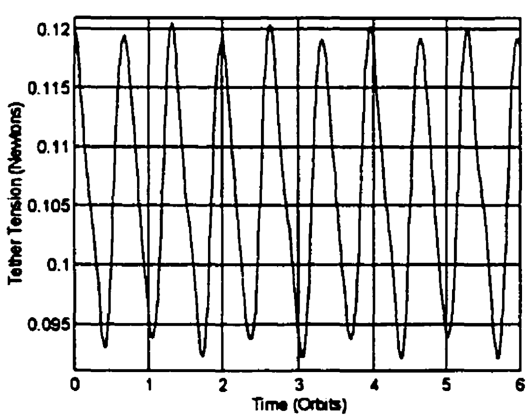

Fig. 4.29: Simulated TiPS Tether Tension for Pitch and Roll Amplitudes of 41° and 22°, Respectively

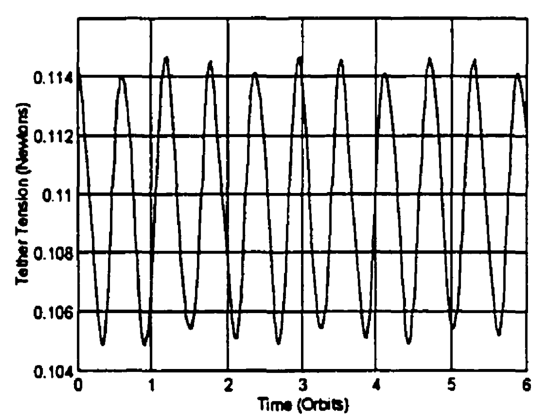

Fig. 4.30: Simulated TiPS Tether Tension for Pitch and Roll Amplitude of 15°

Given that the largest peak-to-peak tension amplitude of 0.08N corresponds to a strain variation of 0.0004, this means that the maximum length variation generated by longitudinal oscillations is approximately 1.6m.

4.3.4.4 Tether Temperature

The simulated tether temperature (Fig. 4.31) shows wild variations that do not follow the expected behaviour [6]. These unexpected variations are due to the large amplitude of the pitch and roll oscillations, which constantly alter the angle between the tether line and the Sun. The maximum and minimum tether temperatures are approximately 210K and 130K, respectively. Given the length of the TiPS tether (4023m) and its coefficient of thermal expansion (-.000028/K), this temperature differential of 80K leads to a maximum thermal elongation of 9m: almost 6 times the maximum mechanical elongation (which occurs immediately after deployment). After 90 days of flight, the ratio of thermal to mechanical elongation reaches 45! In other words, thermal strains influence external torques on the system more strongly than mechanical strains.

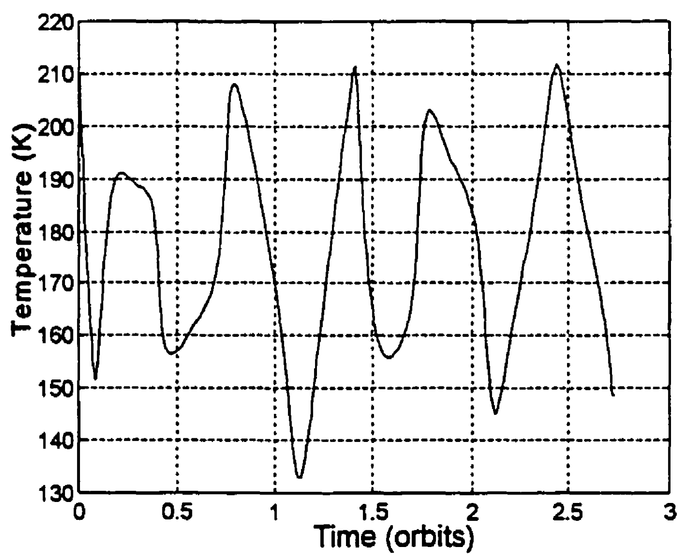

Fig. 4.31: Simulated TiPS Tether Temperature

CHAPTER 5

EFFECT OF ELECTROMAGNETIC FORCES ON TETHERED SYSTEMS

5.1 INFLUENCE OF SYSTEM AND MISSION VARIABLES ON EP

5.1.1 Preliminary Considerations

The study now focuses on the effect of electromagnetic forces and torques on the motion of conductive tethered systems. The first step in this investigation consists of determining the induced EMF, current, and the corresponding Lorentz force for different combinations of mission parameters.

As mentioned by Forward, Hoyt and Uphoff [8], the best tether material for electromagnetic propulsion is aluminum, for this metal combines low density and high conductivity. However, aluminum has such a low emissivity to absorptivity ratio (0.1) that its equilibrium temperature due to solar radiation alone reaches 716K [100]. This temperature is very close to the melting point (933K). Therefore, a bare aluminum tether would unlikely be suitable because solar heating and ohmic dissipation could cause creeping or even melting. To alleviate this difficulty, the aluminum wire should be covered with some high strength tether material or coating with a much higher emissivity to absorptivity ratio. This non-conductive component would provide strength and a "cooler" environment for the aluminum core. Nevertheless, the coating should not impede on the capability of "bare" tethers to capture ionospheric electrons.

The parameters of the subsatellites (m_1 is a parallepiped and m_2 is a sphere), of the tether, of the atmosphere, and of the baseline mission are shown in Tables 5.1 to 5.4, respectively.

Table 5.1: Parameters of the Subsatellites	
Dimensions (a_1,c_1, r_2)	.5m, .8m, .6m
Mass (m_1, m_2)	50kg, 5kg
Load resistance (Ohm)	0

Table 5.2: Parameters of the Tether Core	
Tether core material	Aluminum (2219-T851)
Core density (kg/m^3)	2850
Core resistivity (Ohm*m)	27.4X10^{-9}
Tether radius (mm)	0.2

Table 5.3: Parameters of the Atmosphere	
Ionospheric Plasma Temperature	1000 K
Electron Density Profile (10^{12} e$^-$/m^3)	0.9*sin(Θ) + 1.1

Note that the tether radius quoted above would generate a non-negligible tether resistance. This effect would complicate modelling and has been neglected in most documented investigations [24, 25, 26, 71].

Table 5.4: Mission Baseline Parameters for Simulations	
Semi-major axis (km)	6978 (600 km alt.)
Eccentricity	0
Inclination	0
Tether length (km)	5
System pitch (deg)	0
System roll (deg)	0

Note that for the above system orientation ($\alpha=\gamma=0$), the component of the Lorentz force along the x'-axis always vanishes (Fig. 2.1).

A number of simulations are carried out to determine the effect of various factors on the induced EMF and current, and on the corresponding Lorentz force. The effect of each factor is determined by varying its value, while holding the value of all other factors constant. The following sections (5.1.2 to 5.1.5) discuss the major findings of these simulations, which assume complete reversibility of current flow in conductive tethered systems.

5.1.2 Effect of Tether Length

According to Forward, Hoyt and Uphoff [8], tether lengths for EP (Electromagnetic Propulsion) applications should range between 5 km and 20 km. Such tether lengths are necessary to insure that the tether remains taut at all times. Figures 5.1 through 5.4 show the effect of tether length on EP variables. They display the average EMF, the mean current at m_1, and the average Lorentz force (in orbital coordinates), for both insulated and bare tethered systems.

As shown in equation (2.50) and in Figures 5.1 and 5.2 below, the induced EMF is the same for bare and insulated systems and increases linearly with tether length. On the other hand, the induced current at m_1 and the Lorentz forces are 1 to 2 orders of magnitude larger for bare tethers than for insulated tethers. As mentioned in Section 2.5.4, this results from Debye shielding in insulated systems and clearly demonstrates the superior capability of bare tethers to capture ionospheric electrons.

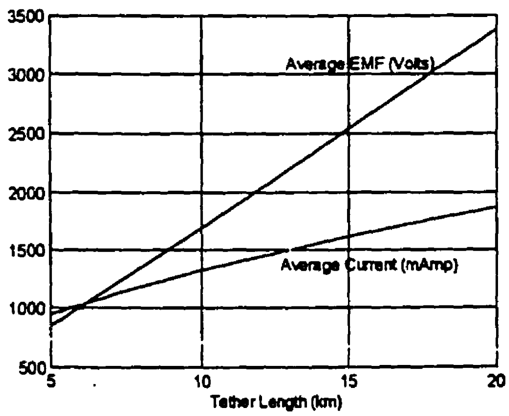

Fig. 5.1: Average EMF and Current Induced in an Insulated Tethered System

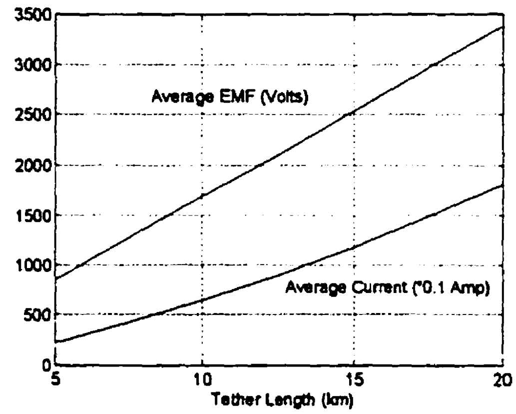

Fig. 5.2: Average EMF and Current at m_1 in a Bare Tethered System

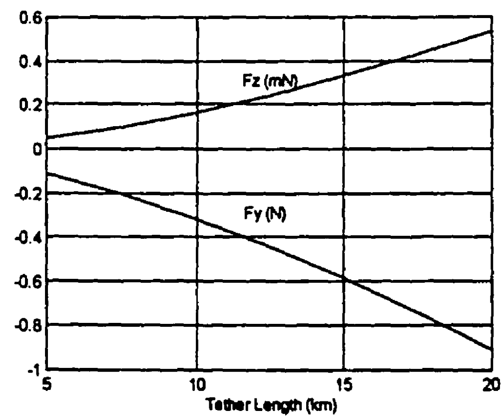

Fig. 5.3: Average Lorentz Forces Induced in an Insulated Tethered System

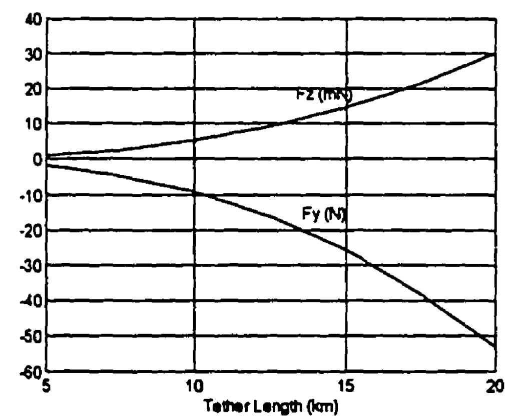

Fig. 5.4: Average Lorentz Forces Induced in a Bare Tethered System

The current in insulated systems follows the expected .528th power law behaviour (Fig. 5.1, equation (2.52)). This inference is further sustained by Figure 5.5 which plots the variation of mission variables for insulated tethers on a log-log scale. As Lorentz forces are proportional to both the current and tether length, they approximately follow a 1.528th power law behaviour (equation (2.57), Fig. 5.1, 5.5).

As for bare wire systems, the induced current at m_1 grows with the 1.5th power of tether length (equation (2.57,2.59), Fig. 5.2, 5.6). By virtue of equation (2.54), this implies that Lorentz forces should vary with the 2.5th power of tether length, which they indeed do (Fig. 5.4, 5.6). This more rapid growth of available power and Lorentz forces constitutes a major advantage of bare wire systems over insulated tethers.

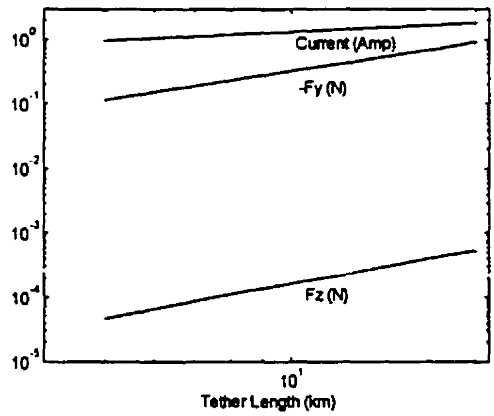

Fig. 5.5: Log-Log Plot of the Variation of Induced Current and Lorentz Forces in Insulated Tethered Systems

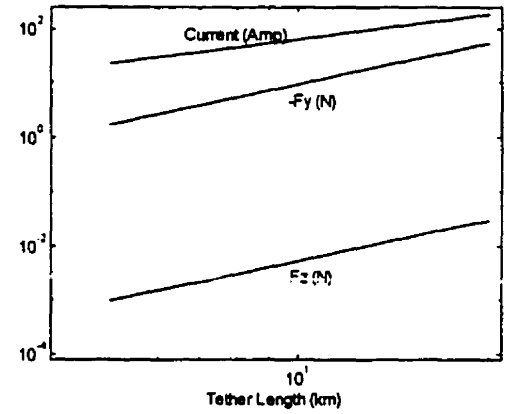

Fig. 5.6 Log-Log Plot of the Variation of Induced Current and Lorentz Forces in Bare Wire Systems

5.1.3 Effect of the Semi-Major Axis

As shown in the Figures below, the altitude of the spacecraft strongly influences the various EP variables (induced EMF and current, Lorentz forces).

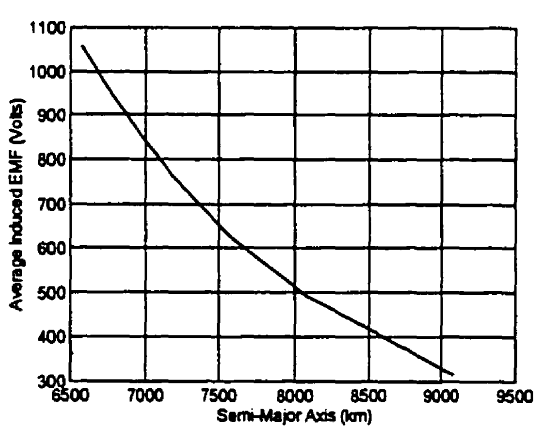

Fig. 5.7: Average EMF Induced for Both Insulated and Bare Tethered Systems

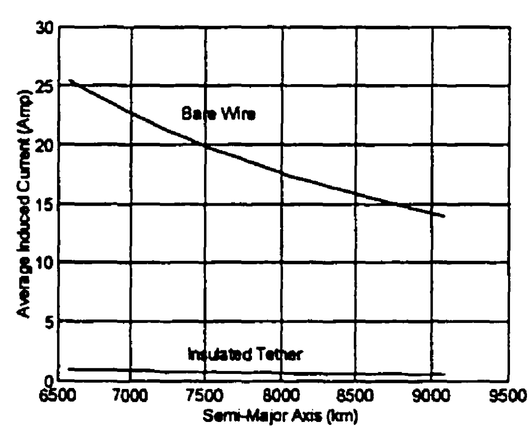

Fig. 5.8: Average Current at m_1 for Insulated and Bare Tethered Systems

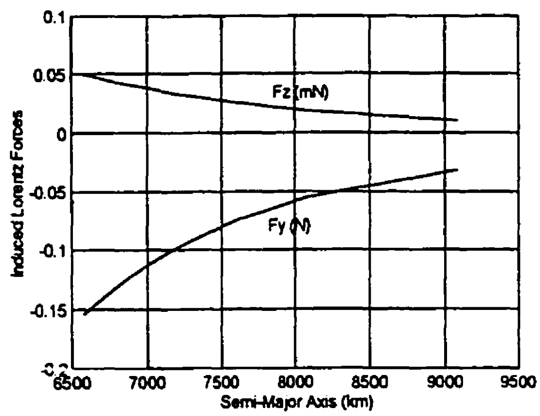

Fig. 5.9: Average Lorentz Forces for Insulated Tethered System

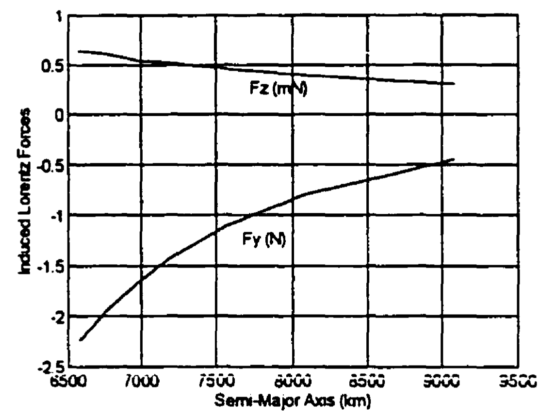

Fig. 5.10: Average Lorentz Forces for Bare Tethered Systems

Once again, the induced EMF does not depend on the nature of the tether (bare of insulated), but merely on its length and position relative to the Earth (Fig. 5.7). In fact, the voltage induced across the system decays with the 3.74th power of the geocentric altitude. By virtue of equation (2.50), this result is consistent with first order approximations [6] which predict a 3.5th power decay of the EMF caused by the 0.5th power decay of orbital speed and the 3rd power decay of the dominant term of the Earth magnetic field. The slight discrepancy between the simulations and approximate results is due to the higher order harmonics of the magnetic field. Figure 5.11 further demonstrates the exponential decay of the induced EMF.

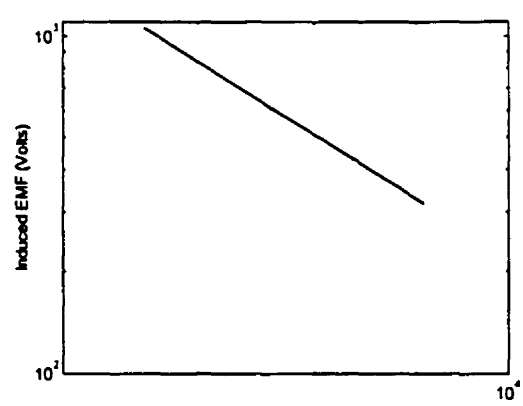

Fig. 5.11: Log-Log Plot of the EMF Variation in Conductive Systems Due to Geocentric Altitude

Since the tether current in insulated systems varies with the 0.528th power of the EMF (equation 2.52), first order approximations predict that the induced current would decay with the inverse of the 1.85th power of altitude. Nonetheless, simulations show that a more refined model of the magnetic field leads to a 1.74th power variation with the altitude. As for bare wire systems, first order approximations predict a 1.75th power variation of current with altitude. On the other hand, the present model yields a 1.87th power decay. Finally, previous studies estimate that Lorentz forces vary with the 5.54th and 5.25th power of distance for insulated and bare wires, respectively. However, simulations show that electromagnetic forces actually decay with the 4.85th and 4.98th power of the altitude, respectively.

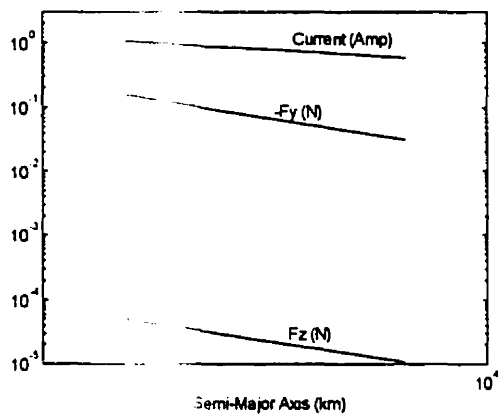

Fig. 5.12: Log-Log Plot of Average EP Variables for Insulated Tethered Systems

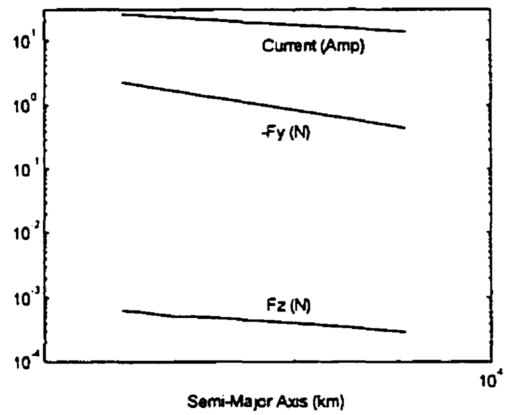

Fig. 5.13: Log-Log Plot of Average EP Variables for Bare Tethered Systems

5.1.4 Effect of the Orbital Inclination

The effect of the orbital inclination on EP variables is shown in Figures 5.14 to 5.17. The orbital inclination strongly influences the average voltage, current, andLorentz forces. As a matter of fact, the EMF and current reverse direction in retrograde orbits. Furthermore, the magnitude of the EP variables reaches a minimum along nearly polar orbits and is larger for inclinations of π-i than i. Indeed, the speed of the spacecraft with respect to a frame moving with the magnetic field of the Earth is larger for retrograde orbits than for direct orbits. By equations (2.50), (2.52), (2.54), and (2.59) this generates larger EMF's, currents, and Lorentz forces

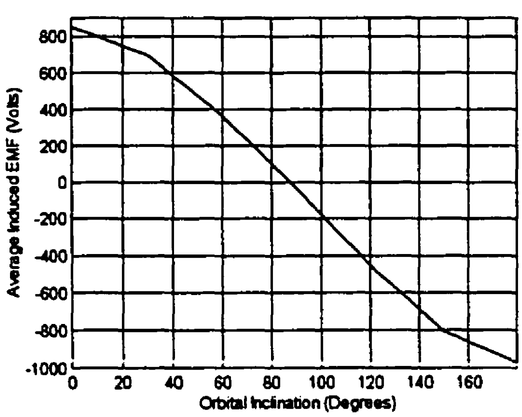

Fig. 5.14: Variation of the Average Induced EMF with the Orbital Inclination for Insulated and Bare Tethered Systems

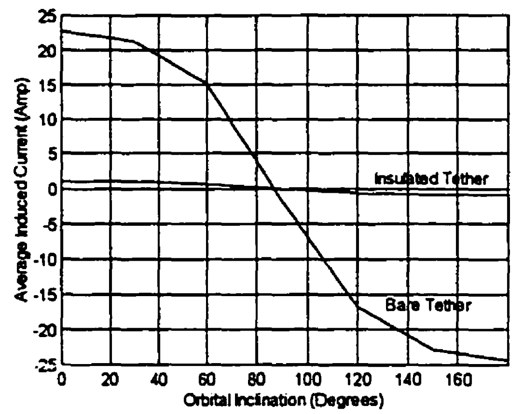

Fig. 5.15: Variation of the Average Current at m_1 with the Orbital Inclination for Conductive Tethered Systems

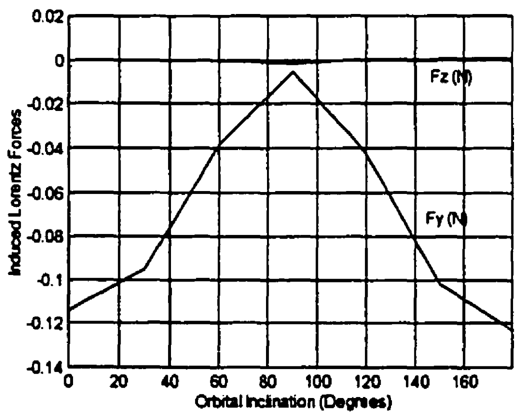

Fig. 5.16: Variation of Average Lorentz Forces with the Orbital Inclination for an Insulated Tethered System

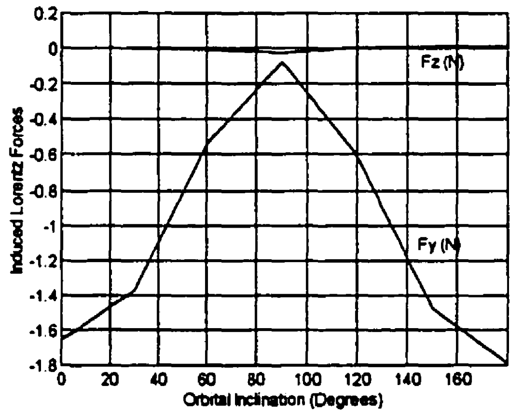

Fig. 5.17: Variation of Average Lorentz Forces with the Orbital Inclination for a Bare Tethered System

In light of the results presented so far in this chapter, the average value of F_y has been shown to always remain negative. The explanation for this is quite simple: the electromagnetic force has the tendency of bringing any conductive object to "rest" with respect to a coordinate system centered at the Earth and rotating with the magnetic field. Whether its trajectory is direct or retrograde, any spacecraft moving at orbital speeds in LEO is bound to travel much faster than the magnetic field (400-500 m/s at the equator). Most importantly, this means that regardless of the inclination, it is impossible to raise the orbit of a spacecraft in a circular orbit by continually applying maximum electromagnetic thrust. In fact, a circular orbit can be raised only if the tangential (y') component of the perturbative force is positive. For altitudes beyond the geostationary orbit, the speed of the magnetic field becomes greater than the orbital speed. A spacecraft travelling along one such trajectory could potentially use the magnetic field of the Earth to obtain both thrust and "free" electrical power. However, the low intensity of the magnetic field at these altitudes may very well undermine the potential of this application. On the other hand, this concept could reveal very attractive for propelling a spacecraft in orbit around Jupiter: a planet with a very strong magnetic field and most of its moons above the "jupitostationnary" orbit.

This leaves only two possible ways of using electromagnetic forces to raise the orbit of a LEO spacecraft: current phasing and EMF reversal. Phasing refers to a procedure in which the tether current is judiciously controlled as a function of the position of the spacecraft along its orbit. By applying the right current at the right moment (with the help of a variable load resistor), one could potentially raise the spacecraft orbit. The second option consists of using a series of batteries to reverse the direction of the induced EMF and provide a positive F_y. However, this possibility is highly impractical, since one would have to work against an EMF of the order of hundreds or even thousands of Volts. The PMG experiment [6] constitutes the only example of such EMF reversal. Indeed, the planners of this mission connected several batteries in series to generate an EMF of approximately 80V, which was higher than the voltage induced by the motion of the 500m tether through the magnetic field. On the other hand, all applications considered in this Chapter require much longer tethers (>5km) to ensure longitudinal stability. Such long cables make EMF reversal very difficult because motional EMF's reach very large values.

5.1.5 Effect of Orbital Motion

The motion of the spacecraft along its orbit causes large periodic variations in the various parameters studied. For example, Figures 5.18 and 5.19 show the variation of the induced voltage for an 18 km long tether in a typical ISS orbit as simulated by the author and by other researchers [26].

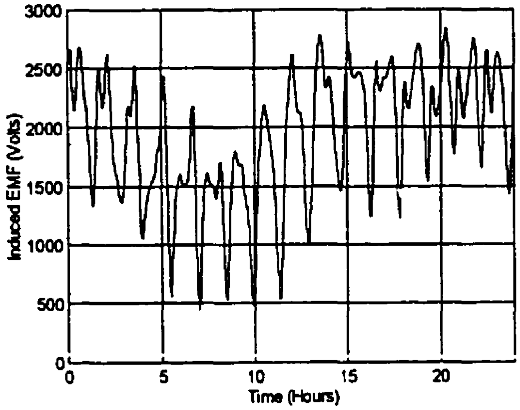

Fig. 5.18: Variation of the Induced EMF for an 18 km Long System Orbiting along an ISS Orbit (Simulated by the Author)

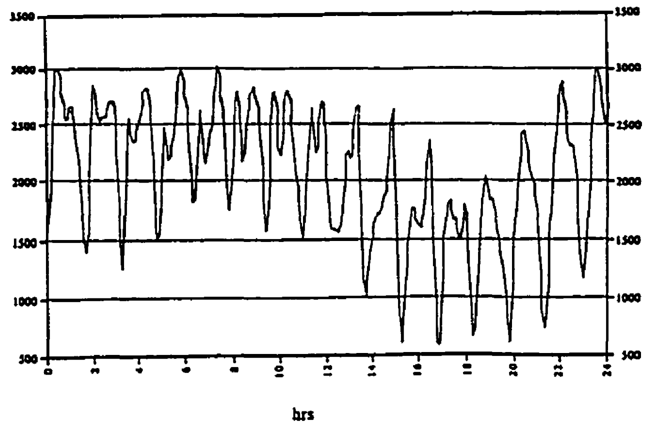

Fig. 5.19: Variation of the Induced EMF for an 18 km Long System Orbiting along an ISS Orbit [26]

Two types of oscillations can be detected from the above graphs: a 24 hour variation due to the rotation of the non-uniform magnetic field, and a higher frequency oscillation due to the motion of the spacecraft along its orbit. Low altitudes, long tethers, highly inclined, and eccentric orbits all contribute to large variations in EP variables.

5.2 ORBIT DECAY USING ELECTROMAGNETIC PROPULSION

5.2.1 Preliminary Considerations

As mentioned in the Introduction, the tethered de-orbit concept proposes to capitalize on the Faraday effect to decay the orbit of dysfunctional satellites and spent rocket stages. The range of tether lengths required to keep the tether taut (>5 km) allows the flow of very high currents (0.5 to 5 Amp) through the tether with EMF's in the kilovolt range. If uncontrolled, these high currents generate large Lorentz torques that destabilize the librations of the system. To exemplify this phenomenon, Figure 5.20 shows the librations of a 5 km long conductive tethered system without a load resistance (R_{load}=0) flying along a circular and equatorial orbit at an altitude of 600 km. The other parameters of the spacecraft of interest are as in Section 5.1.1.

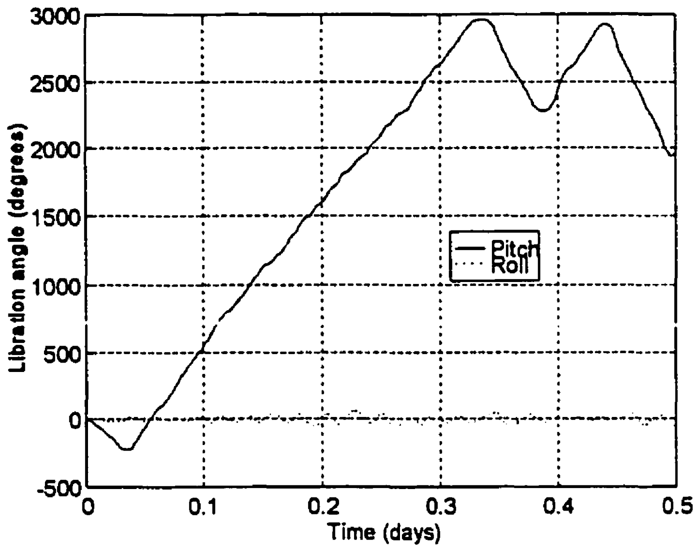

Fig. 5.20: Uncontrolled Librations of a Tethered De-orbit System Flying along a Circular and Equatorial Orbit at an Altitude of 600 km

Stabilizing tether librations while decaying the spacecraft orbit as rapidly as possible requires a sophisticated control system. Although far from optimal, the control scheme chosen for the following simulations is relatively simple. It consists of an ammeter and a varistor working in concert to keep the maximum current at $I = (0.2 + 0.1 * \sin(3\theta))$ *Amp*. The 3θ dependency helps stabilize roll oscillations [6]. To further suppress libration amplitudes, the tether current is cut whenever pitch or roll reaches an amplitude larger than 20°.

5.2.2 Results and Analysis

To demonstrate the effectiveness of the proposed current/libration control scheme, Figures 5.21 and 5.22 show the "controlled" librations of an "electromagnetic tether" flying at an altitude of 1500 km along a circular orbit for two different inclinations: 0° (Fig. 5.21) and 85° (Fig. 5.22). As expected, the libration amplitudes barely exceed 20° in both pitch and roll. Hence, the above control scheme effectively stabilizes tether librations.

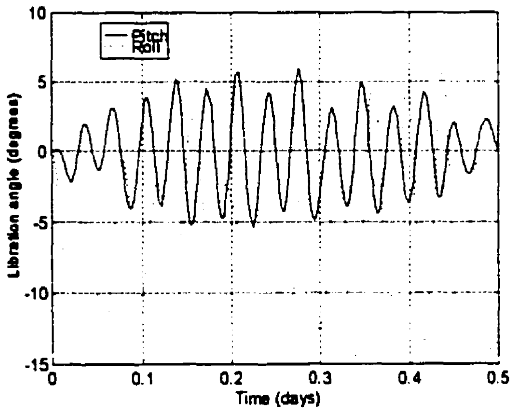

Fig. 5.21: Tether Librations for a "Terminator Tether" Flying along an Equatorial and Circular Orbit at an Altitude of 1500 km

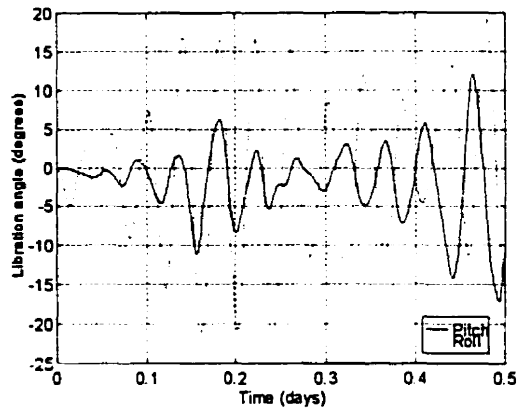

Fig. 5.22: Tether Librations for a "Terminator Tether" Flying along a Circular Orbit Inclined at 85° at an Altitude of 1500 km

Let us now examine how rapidly EP can decay the orbit of a given object. Figure 5.23 displays the evolution of the semi-major axis and perigee for the specimen spacecraft presented in Section 5.1.1 and control system introduced in Section 5.2.1. The satellite initially orbits along an equatorial and circular orbit at an altitude of 1500 km. For this system, the deorbit time is 21 days.

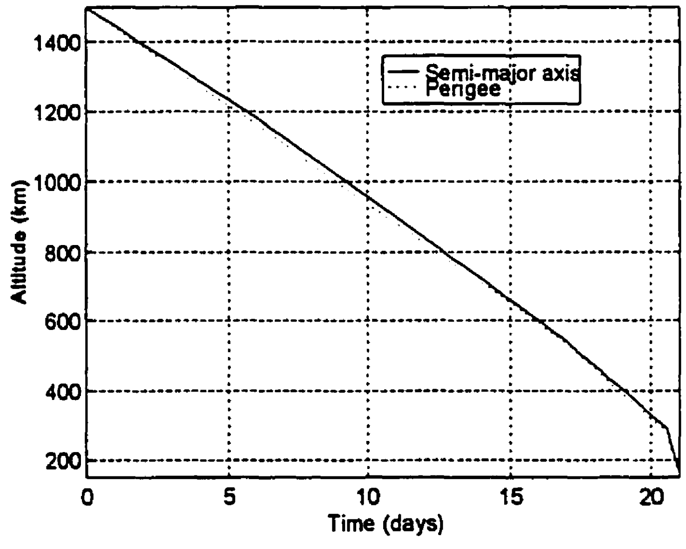

Fig. 5.23: EP Orbital Decay for a Spacecraft Initially Flying along an Equatorial and Circular Orbit at 1500 km of Altitude

As pointed out by Forward and Hoyt [77], deorbit rates decrease drastically for nearly polar orbits because the magnetic field orientation is unfavourable to orbit decay near polar latitudes. This phenomenon is exemplified in Figure 5.24, which shows how the semi-major axis and perigee take much longer to decay for a similar spacecraft initially flying along a circular orbit at an altitude of 1500 km and inclination of 85°.

In Figures 5.23 and 5.24, one notices that the semi-major axis and perigee decay smoothly over most of the manoeuvre (when Lorentz forces dominate), but suddenly drop at the end of the flight (when air drag becomes dominant). Deorbit times of 21 days (for an equatorial orbit) and 101 days (for a nearly polar orbit) compare extremely well with the dozens to thousands of years required for air drag to decay the spacecraft orbit alone. On the other hand, the ballast and conductive tether total 20 kg of the total spacecraft mass. This exceeds the 5.6 kg of Hydrazine-N_2O_4 fuel required to deorbit the 50 kg spacecraft. Therefore, electromagnetic propulsion is not as effective as rocket propulsion to deorbit very small satellites in LEO. This result is totally independent of the control scheme used to stabilize tether oscillations. Indeed, the control system only influences the deorbit time, not the "Terminator Tether" system mass. However, the same EP system (a 5 kg tether measuring 5 km with a 15 kg ballast) can deorbit a 1000 kg satellite initially flying along a 1500 km circular and equatorial orbit within 380 days. In fact, for a given control system, the deorbit time is inversely proportional to the spacecraft mass.

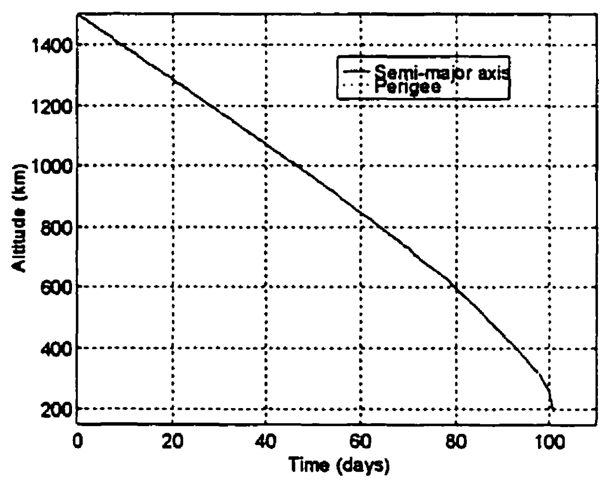

Fig. 5.24: EP Orbital Decay for a Spacecraft Initially Flying a Circular Orbit at an Altitude of 1500 km and an Inclination of 85°

On the other hand, a rocket system designed to accomplish a comparable task would require more than 110 kg of fuel. Further analysis reveals that for the system and rocket fuel described above, EP is more weight efficient than rocket propulsion when the spacecraft mass is larger than 90 kg.

But still, one must bear in mind that the reentry time for rocket propulsion is half of the orbital period (approximately 1 hour), while the reentry time of EP system can vary from weeks to months or even years.

In conclusion, for the control system described in Section 5.1.1, EP is more weight efficient for orbital decay than rocket propulsion when the spacecraft mass is larger than approximately 100 kg. However, the reentry time for "Terminator Tethers" (weeks to months) largely depends on the libration control scheme and is much longer than that of rocket systems (1 hour).

CHAPTER 6

THE DYNAMICS OF SPINNING SPACE TETHERED SYSTEMS

6.1 PRELIMINARY CONSIDERATIONS

While librating systems have been abundantly investigated over the last 30 years, very few studies have focused on the dynamics of spinning tethered systems. Schultz and Vigneron [51,52] have determined that the combined effect of longitudinal tether damping, gravity gradient, and aerodynamic drag causes a net decay of the rotational rate of spinning tethered systems. On the other hand, Carroll [81] maintains that thermally induced tether length variations are likely to cause random variations in the rotational rate of spinning systems. This Chapter partly aims at resolving the debate through simulation of the BOLAS system.

6.2 BOLAS MISSION SCENARIO AND PARAMETERS

The BOLAS proposal is outlined in section 1.4.2 and aims at investigating ionospheric plasma, and the long term dynamics of spinning tethered systems. Table o.1 presents the parameters of the BOLAS subsatellites. The tether proposed for BOLAS is identical to the TiPS tether (Table 4.12), but measures 100m and is assumed to have a damping coefficient of 45.8 kNs. Table 6.2 presents the initial conditions for the flight simulations.

Table 6.1: Parameters of the BOLAS Subsatellites (BOLAS1/BOLAS2)

Parameter	Value	Source
Mass (m_1, m_2)	74.8 kg, 76.3 kg	[101]
Width (a_1, a_2)	0.36 m, 0.36 m	[101]
Height (c_1, c_2)	0.74 m, 0.74 m	[101]
Solar absorptivity (α_{s1})	0.2	Estimated
Normal accommodation coeff. (σ_{n1}, σ_{n2})	0.85	[35]
Tangential accommodation coeff. (σ_{t1}, σ_{t2})	0.85	[35]

Table 6.2: Initial Conditions for BOLAS Flight Simulations

Variable	Value	Source
Beginning of the simulation	Dec. 1st, 2001 GMT 00:00	[101]
Semi-major axis (a)	6943 km	[101]
Eccentricity (e)	0.030966	[101]
True anomaly (θ)	180°	
Inclination (i)	103°	[101]
Argument of perigee (ω)	335°	[101]
Long. of the ascending node (Ω)	90°	[101]
Pitch (α)	45°	
Pitch rate ($d\alpha/dt$)	0.62527°/sec ($10\omega_{orb}$)	[101]

Table 6.2: Initial Conditions for BOLAS Flight Simulations		
Roll (γ)	10°	
Roll Rate ($d\gamma/dt$)	0	
Strain (ϵ)	0.0027428	Equilibrium strain
Strain Rate ($d\epsilon/dt$)	0/s	Equilibrium strain
Tether temperature (T)	180 K	Minimum temperature

In the simulations, the tolerance for Gear's algorithm was chosen to be 0.000002. The duration of the simulation is 180 days and the solar activity index is 150.

6.3 ANALYSIS OF THE BOLAS MISSION

6.3.1 Perturbation Forces

Throughout the range of altitudes flown by BOLAS, Earth oblateness (1N) and solar pressure (10^{-6}N) forces remain fairly constant. On the other hand, eccentricity effects cause aerodynamic lift and drag to vary by a factor of 1000 from 10^{-6}N at apogee to 10^{-3}N at perigee. Lunisolar attraction and electromagnetic forces are neglected. The orbital, attitude, thermal, and longitudinal dynamics of BOLAS are simulated over 180 days.

6.3.2 Orbital Motion

Aerodynamic forces have a very strong effect on the orbital trajectory of BOLAS. Indeed, atmospheric drag causes a decay of 23.7 km in the semi-major axis [Fig. 6.1].

As is the case for TiPS, the semi-major axis of BOLAS also undergoes periodic variations [Fig. 6.1]. The period and amplitude of these oscillations are $2\omega_{orb}$ and 18 km, respectively.

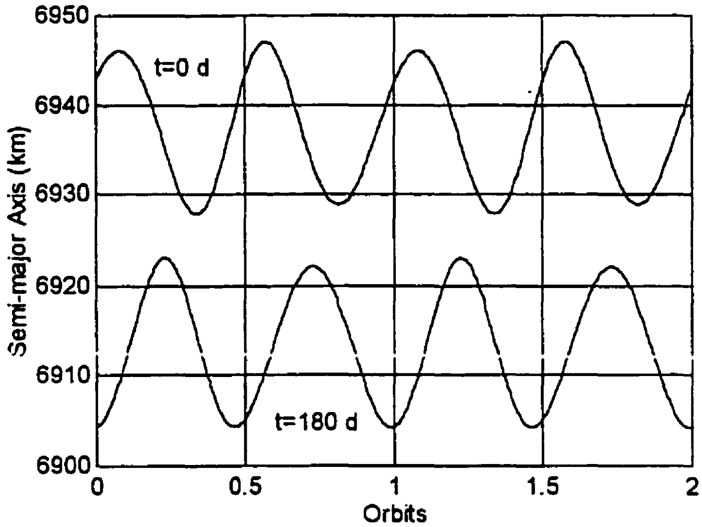

Fig. 6.1: Periodic and Secular Variations of the Semi-Major Axis of BOLAS

Furthermore, the eccentricity decreases from 0.031 to 0.0266 as a result of the combined effect of air drag and solar pressure [33]. Consequently, the apogee of the BOLAS orbit drops from 780 km to 720 km. Finally, the orbital inclination decreases by 1° over six months due to atmospheric rotation.

Earth oblateness causes a drift of the line of apses and of the nodal line. Variations reach -2.87°/day for ω and 1.60°/day for Ω. These results agree with approximate theoretical results (equation 2.47).

6.3.3 Attitude Motion

As shown in Figure 6.2, the pitch rate of the system undergoes two distinct periodic variations: a short period oscillation induced by the spin of the system, and a long period oscillation caused by the spacecraft orbital motion.

The frequency of the short wavelength variation is $20\omega_{orb}$ (twice the spin rate). Its oscillations peak when the system is aligned with the local vertical, and reach a minimum when the satellite crosses the local horizontal. In their analysis of the BOLAS proposal, Schultz and Vigneron [52] also noticed this phenomenon.

In contrast, the long period oscillation is caused by the orbital motion of the spacecraft. Indeed, orbital eccentricity and thermal expansion combine to cause tether stretching which, by conservation of angular momentum, causes variations in the spin rate of the system. In their investigation of the BOLAS proposal, Schultz and Vigneron did not notice this long period oscillation because they did not consider the orbital eccentricity and the thermal dynamics of spinning tethered systems [52]. Their analysis predicts a net decrease in the pitch rate. They attribute this energy loss to the interaction between tether damping and gravity gradient forces [52], and to air drag [51].

The present model predicts random variations of the average spin rate, but an overall increase of 0.0017°/s (0.27%) over 180 days. In other words, the positive torque induced by external perturbations dominates over the negative torque generated by tether damping, gravity gradient forces, and aerodynamic drag [81].

Roll oscillations remain marginally stable near 10° throughout the flight [Fig. 6.3]. The period of the roll oscillations is approximately $11\omega_{orb}$, not $2\omega_{orb}$ as is the case for gravity-gradient stabilized systems. This comes as no surprise, since linearizing the roll equation of motion (2.13) reveals that the frequency of roll oscillations should be about $[(\omega_{spin} + \omega_{orb})^2 + 3\omega_{orb}^2]^{1/2}$; which is approximately $11.1\omega_{orb}$, since $\omega_{spin} = 10\omega_{orb}$ in the present case.

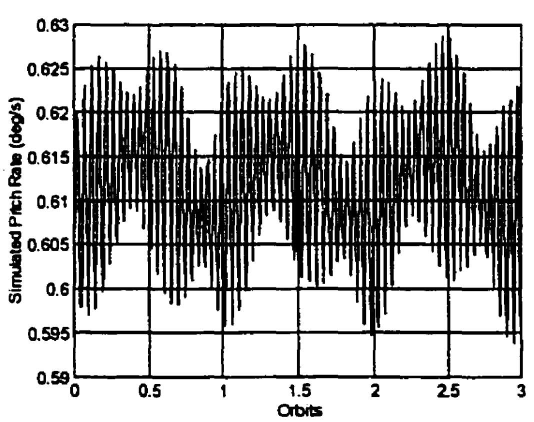

Fig. 6.2: Simulated Pitch Rate of BOLAS

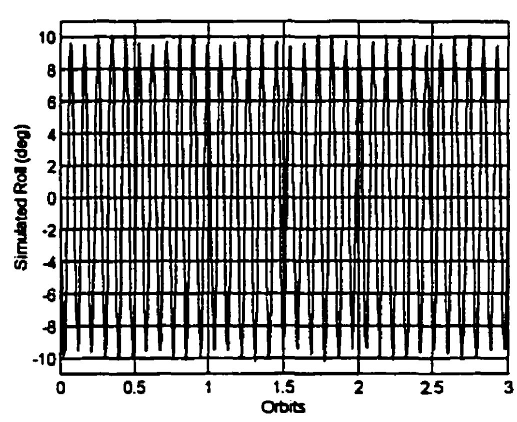

Fig. 6.3: Simulated Roll Oscillations of BOLAS

6.3.4 . .ther Longitudinal Oscillations

Like . . . itch rate, the longitudinal strain of the tether (Fig. 6.4) shows periodic variations d... .. ..her spin (high frequency) and due to orbital motion (low frequency). The average s... . .0264) is consistent with the results of Schultz and Vigneron [52] and generates . . .age tension of approximately 0.5N.

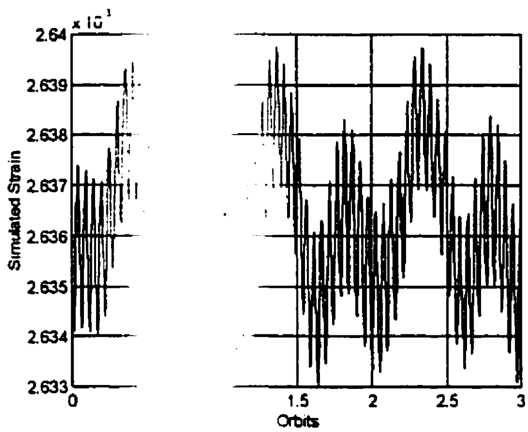

Fig. 6... . ..lated BOLAS Tether
.sc..lations

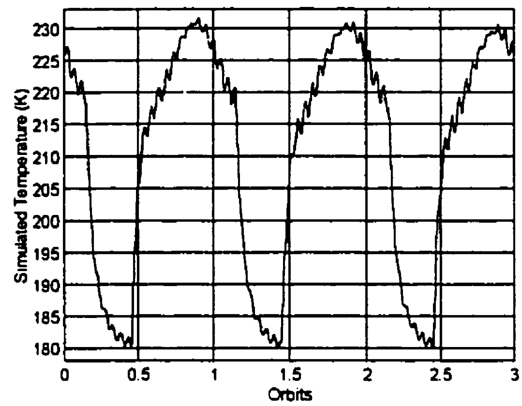

Fig. 6.5: Simulated BOLAS Tether Temperature

6.3.5 . . ...er Temperature

BC . .er temperature variations (Fig. 6.5) are much more regular than that of TiPS (Fig. . .ndeed, the rapid spin rate of BOLAS removes any dependence of tether temperatur . . ..taneous tether orientation. The variation in temperature from 180K to 230K over . . . .uses a variation of 14cm in tether length, which is much greater than the 0.7mm . . n caused by the change in longitudinal strain over an orbit. Once again, this estab... . . mportance of thermal strain on the attitude dynamics of BOLAS.

CHAPTER 7

CONCLUSIONS

A detailed mathematical model and a software have been developed to analyse the long-term effects of the low Earth orbit environment on tethered systems. The software predicts the trajectory and the attitude of the system, as well as the temperature and the longitudinal vibrations of the tether. The program accounts for the effects of atmospheric lift and drag, asphericity of the Earth (zonal and sectorial harmonics), solar and Earth radiation, electromagnetic forces, lunisolar attraction, and material damping.

The thesis extends previous research work in the field using more detailed models of external perturbations, and a refined integration scheme (Gear's method). Particular attention was given to the three major external forces influencing the dynamics of tethered systems: atmospheric forces, Earth oblateness effects, and electromagnetic (Lorentz) forces. Furthermore, analytical solutions were provided for the problem of atmospheric drag induced shift of the equilibrium angle.

Experiments were also carried out to gain further insight on the material properties of SPECTRA, a commonly used space tether material. It was found that this material has a highly non-linear stress-strain relationship and that its properties are highly dependent on the tether loading history.

It was noted that the present formulation can predict the long-term motion of non-conductive librating tethered systems (such as TiPS) with greater accuracy than previous models. The simulation software is also used to study the behaviour of spinning tethered satellites. For example, it was found that unlike what was previously thought, the overall spinning rate of the proposed BOLAS system does not undergo any net reduction.

Finally, the results show that electromagnetic propulsion applied on bare conductive tethers can deorbit spent rocket stages and dysfunctional satellites over 100 kg at a lower "weight cost" than traditional rocket systems and much faster than atmospheric drag.

Looking onward to the future, the author recommends to conduct further research in the area of electromagnetic propulsion. For example, a bare tether could presumably be used to simultaneously control the orbital elements and the librations of tethered systems. This would virtually eliminate the need to consume chemical fuel to control and later deorbit spacecraft.

CHAPTER 8

REFERENCES

[1] Tsiolkovsky, K.E., *Грезйи О Земле И Небе И На Весте*, (Speculations between Earth and Sky, and on Vesta), Izd-vo AN SSR, Moscow, USSR, 1959 reprint, p.35.

[2] Keshmiri, M., *Dynamics and Control of Multi-Body Tethered Satellite Systems*, Ph.D. Thesis, Department of Mechanical Engineering, McGill University, Montreal, Qc, Canada, Jan. 1995.

[3] Hacker, B.C., and Alexander, C.C., *On the Shoulders of Titans: A History of Project Gemini,* http://www.hq.nasa.gov/office/pao/History/SP-4203, NASA Special Publication-4203 in the NASA History Series, 1977, pp.361, 366-368, 378-379.

[4] NASA Image Exchange Website, http://nix.nasa.gov/nix.cgs, Photo ID S66-62794.

[5] Jablonski, A.M., Vigneron, F.R., Tyc, G., Han, R.P.S., Misra, A.K., Modi, V.J., and Chandrashaker, R., *OEDIPUS-C Tether Dynamics Experiment*, 9th CASI Conference on Astronautics, Ottawa, ON, Nov. 13-15, 1996.

[6] Cosmo, M.L., and Lorenzini, E.C., *Tethers in Space Handbook*, 3rd Ed., Smithsonian Astrophysical Observatory, Cambridge, MA, 1997, pp.2-24, 28-35, 37-40, 49-50, 59, 71-72, 75-78, 81-82, 107-108, 137-151, 158-162, 167-168, 181-186.

[7] *OEDIPUS Program Website*, http://www.conveyor.com/space/oedipus/oedipus.html.

[8] Forward, R.L, Hoyt, R.P, and Uphoff, C., *The Terminator Tether™: A Low-Mass System for End-of-Life Deorbit of LEO Spacecraft*, Tether Technical Interchange Meeting, Huntsville, AL, Sept 10 1997.

[9] NASA Image Exchange Website, http://nix.nasa.gov/nix.cgs, Photo ID STS75711024.

[10] Purdy, W., Coffey, S., Barnds, W.J., Kelm, B., and Davis, M., *TiPS: Results of a Tethered Satellite Experiment*, Presented at the AAS/AIAA Astrodynamics Specialist Conference, Sun Valley ID, Aug. 4-7 1997, Paper No. AAS-97-600.

[11] *TiPS Website*, http://hyperspace.nrl.navy.mil/TiPS/sepdraw.html.

[12] *ATEx Website*, http://hyperspace.nrl.navy.mil/ATEX/ATEx.html.

[13] *ATEx Website*, http://hyperspace.nrl.navy.mil/ATEX/STEX_ATEx1.gif.

[14] *ATEx Website*, http://hyperspace.nrl.navy.mil/ATEX/Tether.gif.

[15] Licata, R., Gavira, J.M., Bracciaferri, F., and Vysokanov, *SESDE: A First European Tether Experiment*, Presented at the 49th IAF Astronautical Congress, Melbourne, Australia, Sept. 28 - Oct. 2, Paper No. IAF-98-A.7.09.

[16] Eichler, P., Reynolds, R., Bade, A., and Johnson N., *Historical Evolution and Current Status of the Number and Mass of Objects in Earth Orbit*, Presented at the 49th IAF Astronautical Congress, Melbourne, Australia, Sept. 28 - Oct. 2, Paper No. IAF-98-IAA.6.3.06.

[17] *Tethers Unlimted Website*, http://www.tethers.com/Newsletter2.pdf.

[18] *Tethers Unlimted Website*, http://www.tethers.com/Webimages/TT.GIF.

[19] *AIRSEDS-S Explorer Guide*, http://www.airseds.com/introduction.html.

[20] *AIRSEDS-S Explorer Guide*, http://www.airseds.com/probeandinstru.gif.

[21] Jablonski, A.M., James, H.G., Tyc, G., Vigneron, F.R., Carrington, C.K., Rupp, C.C., and Harrison, J.K., *The BOLAS Tether Ionospheric Mission,* Presented at the 49th IAF Astronautical Congress, Melbourne, Australia, Sept. 28 - Oct. 2, Paper No. IAA-98-IAA-.11.4.02.

[22] *BOLAS Website*, http://gauss.gge.unb.ca/BOLAS.html

[23] *BOLAS Website*, http://gauss.gge.unb.ca/BOLAS/images/bolas_ab.gif.

[24] Johnson, L., and Herrmann, M., *International Space Station Electrodynamic Tether Reboost Study,* NASA TM–1998-208538, Marshall Space Flight Center, Hunstville, AL, Jul. 1998.

[25] Estes, R.D., Sanmartin, J.R., and Martinez-Sanchez, M., *Technology of Bare Tether Current Collection,* Tether Technology Interchange Meeting, NASA Marshall Space Flight Center, Hunstville, AL, Sept. 9-10, 1997.

[26] Lorenzini, E.C., Estes, R.D., and Cosmo, M.L., "Electrodynamic Tethers for the International Space Station", *In-Space Transportation with Tethers*, Annual Report for NASA Grant NAG9-1303, Smithsonian Astrophysical Observatory, Cambridge, MA, Oct. 1997, pp.4-23.

[27] Von Tiesenhausen, G., *The Roles of Tethers on Space Station*, NASA TM-86519, Marshall Space Flight Center, Huntsville, AL, Oct. 1985.

[28] Quadrelli, B.M., and Lorenzini, E.C, "Dynamics and Stability of a Tethered Centrifuge in Low Earth Orbit", *The Journal of the Astronautical Sciences*, Vol. 40, No. 1, 1992, pp.3-25.

[29] Puig-Suari, J., *Aerobraking Tethers for the Exploration of the Solar System*, Ph.D. Thesis, School of Aeronautics and Astronautics, Purdue University, West Lafayette, IN, Aug. 1993.

[30] Penzo, P.A., *Tether Assisted Penetrators for Comet/Asteroid Sample Return*, AIAA/AAS Astrodynamics Conference, 1986.

[31] Penzo, P.A., and Mayer, H.L., "Tethers and Asteroids for Artificial Gravity Assist in the Solar System", *Journal of Spacecraft and Rockets*, Vol. 23, No. 1, Jan.-Feb. 1986, pp. 79-82.

[32] Lanoix, E.L.M., and Misra, A.K., *Tether Sling Shot Assist*, AAS 97-604, AAS/AIAA Astrodynamics Specialist Conference, Sun Valley, ID, Aug. 4-7, 1997, Paper No. AAS-97-604.

[33] Chobotov, V.A., *Orbital Mechanics*, AIAA Education Series, Washington, DC, 1991, pp.188, 209-216.

[34] Boden. D.G., "Introduction to Astrodynamics", *Space Mission Analysis and Design*, Ed. Larson, W.J., and Wertz, J.R, Microcosm and Kluwer Academic Publishers, Torrance, CA, 1992, pp.129-156.

[35] Hughes, P.C., *Spacecraft Attitude Dynamics*, Wiley, New York, NY, 1986, pp.248-266.

[36] Jacchia, L.G., *Thermospheric Temperature, Density, and Composition: New Models*, Special Report 375, Smithsonian Astrophysical Observatory, Cambridge, MA, Mar. 1977.

[37] Warnock, T.W., and Cochran, J.E., "Orbital Lifetime of Tethered Satellites", *The Journal of the Astronautical Sciences*, Vol. 41, No. 2, Apr.-Jun. 1993, pp.165-188.

[38] Kaplan, M.H., *Modern Spacecraft Dynamics and Control*, Wiley, New York, 1976, pp.349-353, 355-357.

[39] Baker, R.M.L., *Astrodynamics, Applications and Advanced Topics*, Academic Press, New York NY, 1967, pp.188, 192-194.

[40] Kulla, P., *Dynamics of Dumbell Satellites*, ESA Rep. TMM/77-134/pk/cb, 1977.

[41] Bainum, P.M., and Kumar, V.K., "Optimal Control of the Shutle-Tethered-Subsatellite System", *Acta Astronautica*, Vol. 7, 1980, pp.1333-1348.

[42] Misra, A.K., and Modi, V.J., :"A Survey on the Dynamics and Control of Tethered Satellite, Tethers in Space", *Advances in the Astronautical Sciences*, Vol. 62, 1987, pp.667-720.

[43] Lorenzini, E.C., Grossi, M.D., and Cosmo, M., "A Low Altitude Tethered Mars Probe", *Acta Astronautica*, Vol. 21, No. 1, 1990, pp.1-12.

[44] Keshmiri, M., and Misra, A.K., *Effects of Aerodynamic Lift on the Stability of Tethered Subsatellite System*, AAS 93-184, AAS/AIAA Spaceflight Mechanics Meeting, Pasadena, CA, 1993.

[45] Onada, J., and Watanabe, N., "Tethered Subsatellite Swinging from Atmospheric Gradients", *Jounal of Guidance*, Control, and Dynamics, Vol. 11, Sept.-Oct. 1988, pp.477-479.

[46] Beletskii, V.V., and Levin, E.M., "Dynamics of the Orbital Cable System", *Acta Astronautica*, Vol. 12, No. 5, May 1985, pp.285-291.

[47] No, T.S., and Cochran, J.E., "Dynamics and Stability Analysis of an Orbiter-Tether-

Maneuvrable Subsatellite System", Spaceflight Mechanics 1991, *Advances in the Astronautical Sciences*, Vol. 75, Part 2, 1991, pp.987-1006.

[48] Kalaghan, P.M., Arnold, D.A., Colombo, G., Grossi, M.D., Kirschner, L.R., and Orringer, O., *Study of the Dynamics of a Tethered Satellite System (Skyhook)*, Final Report NAS8-32199, Mar. 1978.

[49] Lang, D.D., GTOSS Generalized Tethered Object Simulation System Reference Manual, 1983.

[50] Beletskii, V.V., and Levin, E.M., "Dynamics of Space Tether Systems", *Advances in the Astronautical Sciences*, Vol. 83, 1992.

[51] Schultz, F., and Vigneron, F.R., *Loss of Rotation of the BOLAS Tethered Spacecraft Due to Aerodynamic Drag*, Dept. of Mech. and Aerospace Eng., Carleton University, Feb. 28, 1998.

[52] Schultz, F., and Vigneron, F.R., *Loss of Rotation of the BOLAS Tethered Spacecraft Due to Gravity Gradient Forces*, Dept. of Mech. and Aerospace Eng., Carleton University, Feb. 16, 1998.

[53] Angrilli, F., Bianchini, G., Da Lio, M., and Fanti, G., "Modelling the Mechanical Properties and Dynamics of the Tethers for the TSS-1 and TSS-2 Missions", *ESA Journal*, Vol. 12, No. 3, 1988, pp.353-368.

[54] Fanti, G., Angrilli, F., Bagliono, P., and Bianchini, G., "Mechanical testing on a Composite Flexible Structure", *Spacecraft Structures and Mechanical Testing*, Vol. 1, 1991, pp. 375-381.

[55] *TiPS Website*, http://hyperspace.nrl.navy.mil/TiPS/plots/stiffness.gif

[56] Angrilli, F., Bianchini, G., Da Lio, M., and Fanti, G., *Mechanical and Thermic Properties for Evaluation of TSS-1 Tether Dynamic Behaviour*, Third International

Conference on Tethers in Space Toward Flight, San Francisco CA, May 17-19, 1989, Paper No. 89-1595-CP.

[57] He, X., and Powell, J.D., "Tether Damping in Space", *Journal of Control, Dynamics and Guidance*, Vol. 13, No. 1, Jan.-Feb. 1990, pp.104-112.

[58] Battin, R.H., *An Introduction to the Mathematics and Methods of Astrodynamics*, AIAA Education Series, Washington DC, 1987, pp.490-493.

[59] Modi, V.J., Chang-Fu, G., Misra, A.K., Ming Xu, D., "On the Control of the Space Shuttle Based Tethered Systems", *Acta Astronautica*, Vol. 9, No. 6-7, 1982, pp.437-443.

[61] Biswell, B., and Puig-Suari, J., *Lifting Body Effects on the Equilibrium Orientation of Tethers in the Atmosphere*, AIAA 96-3597, AIAA/AAS Astrodynamics Conference, San Diego, CA, 1996.

[62] *World Data Center Website*, gopher://solar.sec.noaa.gov:70/19/weekly/sunspot

[63] Wells, D.A., *Theory and Problems of Lagrangian Dynamics, with a Treatment of Euler's Equations of Motion, Hamilton's Equations and Hamilton's Principle*, Schaum, New York, NY, 1967.

[64] Zarrouati, G., *Trajectoires Spatiales*, CNES, CEPADUES-Editions, Toulouse, France, 1987, pp.87-89.

[65] Larson, W.J., and Wertz, J.R, *Space Mission Analysis and Design*, Microcosm and Kluwer Academic Publishers, Torrance CA, 1992.

[66] U.S. Nautical Almanac Office, *The Astronomical Almanac*, Washington, DC, 1996, pp.C24, D46.

[67] Moyer, T.D., *Mathematical Formulation of the Double-Precision Orbit Determination*

Program (DPODP), JPL Technical Report #32-1527, May 1971, p.33.

[68] The Defense Mapping Agency, *Department of defense World Geodetic System 1984: Its Definition and Relationships with Local Geodetic Systems*, 2nd Ed., Sept. 1991.

[69] Langel, R.A., *Main Field*, Geomagnetism, edited by J.A. Jacobs, Academic Press, London, 1987, pp.249-512.

[70] IAGA Division V, Working Group 8, "International Geomagnetic Reference Field, 1995 Revision", *Journal of Geomagnetism and Geoelectricity*, Vol. 47, 1995, pp.1257-1261.

[71] Sanmartin, J.R., Martinez-Sanchez, M., and Ahedo, E., "Bare Wire Anodes for Electrodynamic Tethers", *Journal of Propulsion and Power*, Vol. 9, 1993, pp.353-360.

[72] Parker, L.W., and Murphy, B.L., "Potential Buildup on an Electron-Emitting Satellite", *Journal of Geophysical Research*, 72, 1976.

[73] Thompson, D.C., Bonifazi, C., Gilchrist, B.E., Williams, S.D., Raitt, W.J., Lebreton, J.-P., Burke, *The Current-Voltage Characteristics of a Large Probe in Low Earth Orbit: TSS-1R Results*, http://setswww.sprl.umich.edu/sets/public/papers/publications/grl97/IV- characteristics/IV-char.html, 1997.

[74] Carroll, J.A., *Private Communication*, Oct., 1998.

[75] Moore, R.D., *The Geomagnetic Thruster -- A High Performance "Alfven Wave" Propulsion System Utilizing Plasma Contacts*, AIAA Paper No. 66-257.

[76] Bate, R.R, Mueller, D.D., and White, J.E., *Fundammentals of Astrodynamics*, Dover, New York NY, 1971, p.399-404.

[77] *Tethers Unlimted Website*, http://www.tethers.com

[78] *Tethers Unlimted Website*, http://www.tethers.com/WebImages/DeorbitRate.gif

[79] *Tethers Unlimted Website*, http://www.tethers.com/WebImages/DeorbitTime.gif

[80] Moulton, F.R., *An Introduction to Celestial Mechanics*, Dover, New York NY, 1970, pp.337-338.

[81] Carroll, J.A., *Private Communication*, Aug., 1998.

[82] Modi, V.J., and Misra, A.K., "On the Deployment Dynamics of Tether Connected Two-Body Systems", *Acta Astronautica*, Vol. 6, No. 9, 1979, pp.1183-1197.

[83] Serway, R.A., *Physics for Scientists and Engineers*, 3rd Ed., Saunders College Publishing, Philadelphia PA, p.492-494.

[84] Colombo, G., Grossi, M., Dobrowolny, M., and Arnold. D., *Investigation of Electrodynamic Stabilization and Control of Long Orbiting Tethers*, Interim Report on Contract NAS8-33691, Smithsonian Astrophysical Observatory, March 1981.

[85] Carroll, J.A., and Alexander, C.M., *SEDS: The Small Expandable-tether Deployment System*, Final Report on NASA SBIR Phase II Contract NAS8-35256, Dec. 1987.

[86] Inman, D.J., *Engineering Vibrations*, Prentice-Hall, 1996, p.44-45.

[87] Modi, V.J., and Pradhan, S., *Damping Test for the OEDIPUS Tether*, Department of Mechanical Engineering, University of British Columbia, Jul. 1996.

[88] Glaese, J.R., *TiPS Tether Dynamics Analysis Final Briefing*, Control Dynamics Division, BD Systems, June 30 - July 1, 1997.

[89] Wilson, W.K., *Practical Solution of Torsional Vibration Problems*, Vol. 1, 2nd Ed., Wiley and sons, New York, NY, 1948, pp.1-18.

[90] AIAA (American Institute of Aeronautics and Astronautics), *AIAA Aerospace Design Engineers Guide*, 3rd Ed., Washington, DC, 1993, pp.2-8, 2-19.

[91] Carroll, J.A., *Private Communication,* Oct., 1997.

[92] The Mathworks, *SIMULINK: Dynamic System Simulation for MATLAB,* Jan. 1997, p.4-1 to 4-28.

[93] Gear, C.W., *Numerical Initial Value Problems in Ordinary Differential Equations,* Prentice-Hall Inc., Englewood Cliffs, N.J., 1971.

[94] *TiPS Website*, http://hyperspace.nrl.navy.mil/TiPS/techspecs.html

[95] *TiPS Website*, http://hyperspace.nrl.navy.mil/TiPS/tips.els

[96] Barnds, W.J., Private communication, Nov. 1997, Jul. 1998.

[97] *TiPS Website*, http://hyperspace.nrl.navy.mil/TiPS/optical.html

[98] Barnds, W.J., Private communication, Aug. 1998.

[99] *TiPS Website*, http://hyperspace.nrl.navy.mil/TiPS/elements.html

[100] McMordie, R.K., "Thermal", *Space Mission Analysis and Design*, Ed. Larson, W.J., and Wertz, J.R, Microcosm and Kluwer Academic Publishers, Torrance CA, 1992, pp.409-430.

[101] James, G., et al., BOLAS Phase A Report to the Space Sciences Directorate of the Canadian Space Agency, Jan. 1997.